Computational Modelling of Mechanically Induced Electrophysiological Alterations of Axons and Nerve

Man Ting Kwong

St Hugh's College
University of Oxford

A thesis submitted for the degree of Doctor of Philosophy

Hilary 2018

Abstract

In the last decade, traumatic brain injuries (TBIs) and spinal cord injuries (SCIs) has become one of the most scrutinised medical challenges of our time. However, the lower quality of life experienced by the sufferer and the associated socio-economic cost of both TBI and SCI remain a huge burden for society. There is currently no reliable way to evaluate the level of functional damage caused by TBI and SCI related mechanical forces without invasive examination. The types of axonopathy involved in such injuries are the combinations of coupled mechanical-electrophysiological phenomena at multiple length and time scales, extremely challenging to approach by experimental means alone. It is therefore highly desirable to complement experimental studies with computational work to further the understanding of such multiscale problems.

This thesis firstly proposes a novel 3D finite element framework coupling mechanics and electrophysiology to model cellular and subcellular phenomena, such as nerve dislocation and membrane damage by micropipette. The former study shows that 1D simulations focussing solely on the stretch component of the axonal damage are unable to capture the same electrophysiological damage that a 3D framework predicts. The latter study shows that local membrane deformation can lead to electrophysiological alterations at the axonal level solely through geometrical effects and without the need to account for ion channel activity alterations. This was demonstrated for micropipette suction in a patch clamp where the consideration of the 3D flow of current was sufficient to alter its electrophysiology, offering an alternative explanation to the damage mechanism hypothesised by published experimental work.

At the axonal and tissue scale, previous models have often simplified the modelling of damage by using a single axon model [1–3]. It is however unclear whether an altered axonal electrophysiology can truly be representative of the compound electrophysiology of multiple axons or fibre. Three different models: axonal, fibre and tissue level models, were evaluated and compared for their ability to model macroscale electrophysiology deficits. The results of the three models suggest that the recovery of compound action potential amplitude post-mechanical stretch can not be straightforwardly scaled from axonal level to fibre level. Furthermore, the electrophysiological recovery may not be solely dependent on mechanical recovery of the tissue.

This thesis identified the need for scale specific models in the context of TBI and SCI. In particular, lipid bilayer membrane geometrical distortion following mechanical insult at the subcellular scale and functional tissue alteration at the tissue scale both require a different approach. The models proposed herein successfully identify mechanisms overlooked in previous experimental literature. In order to fully capture experimental behaviour, future models will need to account for other mechanisms such as mechanoporation, reorganisation of paranodal junctions and injury related Ca^{2+} imbalance.

Computational Modelling of Mechanically Induced Electrophysiological Alterations of Axons and Nerve

Man Ting Kwong

St Hugh's College

University of Oxford

A thesis submitted for the degree of

Doctor of Philosophy

Hilary 2018

Acknowledgements

I would like to use this opportunity to express my gratitude to everyone who supported me throughout the course of my DPhil. study. In particular my parents, who have only ever wanted the best for me. My father who was there to help me through difficult times, even though he had the biggest battle to fight himself. He taught me the perseverance that I needed to complete this thesis, and he always believed in me. My mother who has been the most understanding and supportive with my decision to study and throughout my doctorate degree. I would also like to thank my brother, my aunts, uncle and cousin who have all humblely supported me through this degree. Without them this could not be possible.

I would like to thank Prof. Antoine Jerusalem for giving me the opportunity to study for a doctorate and all the weekly meetings with him. My sincere thanks to Prof. Jose Pena, Prof. Ludovic Noels, Dr. Julian Garcia, Dr. Lina Homsi, Dr. Antonio Lattore and Dr. Daniel Garcia for all the time and effort they put in for the research presented in this thesis, it has been a pleasure to work with and learn from these outstanding researchers. I would like to express my gratitude to Prof. Amy Zavasky and Dr. Marrie-Anne, who have both supported me throughout my DPhil outside my research. I would also like to thank Prof. Allan Ramsay for proof reading this thesis.

I would also like to thank my dear friends who has supported me, particularly Munirah and Ross who have shared their own PhD. experiences with me and always just a phone call away. I would also like to thank Dr. Dongli Li, Dr. Lili Zhang and Dr. Julian Garcia, whom are all distinctive researchers who have become very dear friends to me, it has been an honour to work with them.

Finally, I would like to thank Steve, who has always been there for me through the highs and lows over the four years. This thesis would not be possible without him.

Abstract

In the last decade, traumatic brain injuries (TBIs) and spinal cord injuries (SCIs) has become one of the most scrutinised medical challenges of our time. However, the lower quality of life experienced by the sufferer and the associated socio-economic cost of both TBI and SCI remain a huge burden for society. There is currently no reliable way to evaluate the level of functional damage caused by TBI and SCI related mechanical forces without invasive examination. The types of axonopathy involved in such injuries are the combinations of coupled mechanical-electrophysiological phenomena at multiple length and time scales, extremely challenging to approach by experimental means alone. It is therefore highly desirable to complement experimental studies with computational work to further the understanding of such multiscale problems.

This thesis firstly proposes a novel 3D finite element framework coupling mechanics and electrophysiology to model cellular and subcellular phenomena, such as nerve dislocation and membrane damage by micropipette. The former study shows that 1D simulations focussing solely on the stretch component of the axonal damage are unable to capture the same electrophysiological damage that a 3D framework predicts. The latter study shows that local membrane deformation can lead to electrophysiological alterations at the axonal level solely through geometrical effects and without the need to account for ion channel activity alterations. This was demonstrated for micropipette suction in a patch clamp where the consideration of the 3D flow of current was sufficient to alter its electrophysiology, offering an alternative explanation to the damage mechanism hypothesised by published experimental work.

At the axonal and tissue scale, previous models have often simplified the modelling of damage by using a single axon model [1–3]. It is however unclear whether an altered axonal electrophysiology can truly be representative of the compound electrophysiology of multiple axons or fibre. Three different models: axonal, fibre and tissue level models, were evaluated and compared for their ability to model macroscale electrophysiology deficits. The results of the three models suggest that the recovery of compound action potential amplitude post-mechanical stretch can not be straightforwardly scaled from axonal level to fibre level. Furthermore, the electrophysiological recovery may not be solely dependent on mechanical recovery of the tissue.

This thesis identified the need for scale specific models in the context of TBI and SCI. In particular, lipid bilayer membrane geometrical distortion following mechanical insult at the subcellular scale and functional tissue alteration at the tissue scale both require a different approach. The models proposed herein successfully identify mechanisms overlooked in previous experimental literature. In order to fully capture experimental behaviour, future models will need to account for other mechanisms such as mechanoporation, reorganisation of paranodal junctions and injury related Ca^{2+} imbalance.

Contents

List of Figures **ix**

List of Abbreviations **xi**

1 Introduction **1**

1.1 Traumatic brain injury and spinal cord injury 1

1.2 Axons in the nervous system 3

1.3 The multiscale nature of traumatic brain injury and spinal cord injury 5

1.4 Scope of thesis 7

2 Literature Review **9**

2.1 Experimental work 10

2.2 Computational models of damaged electrophysiology 15

2.3 Computational modelling of mechanical damage of axon 16

2.4 Computational model coupling mechanical and electrophysiology models 18

3 3D axon model **27**

3.1 Finite element framework 29

3.1.1 Mechanics 29

3.1.2 Electrophysiology 30

3.1.3 Coupled problem 35

3.2 Boundary conditions implementation and verification 37

3.2.1 Implementation 37

3.2.2 Verification 39

3.3 Axonal indentation 41

3.3.1 Simulation setup 43

3.3.2 Results and discussion 45

3.3.3 Comparison of coupled “left-shift” theory between 1D and 3D models 48

4 Subcellular Modelling of Axons **51**
4.1 Geometry 54
4.2 Boundary conditions 55
4.3 Results 56
4.4 Discussion 57

5 Axon to nerve scaling **63**
5.1 Experimental study 64
5.2 Axonal bundle model 65
5.3 Calibration of axonal fibre model 71
5.4 Calibration of representative axon model 74
5.5 Discussion 76

6 Modelling tissue scale mechanically induced electrophysiological alteration **81**
6.1 Constitutive model framework 82
6.1.1 Mechanics 82
6.1.2 Electrophysiology 86
6.1.3 Coupling of mechanics and electrophysiology 87
6.2 Calibration 87
6.2.1 Mechanical model calibration 87
6.2.2 Energies evaluation 89
6.3 Results 90
6.4 Discussion 93

7 Conclusion **97**
7.1 Summary 97
7.2 Conclusion 99
7.3 Future work 100

Appendices

A Appendix **105**
A.1 $\frac{\partial f_{CT}}{\partial V}$ 106
A.2 $\frac{\partial f_{HH}}{\partial V}$ 106
A.3 $\frac{\partial f_{CT}}{\partial u_{kb}}$ 108
A.4 $\frac{\partial f_{HH}}{\partial u_{kb}}$ 108
A.5 $\frac{\partial n_i}{\partial u_{kb}}$ 109
A.6 ε_s 110
A.7 1D FE script 111

References **117**

List of Figures

1.1 A typical axon in the white matter. 4
1.2 A typical action potential profile 5

2.1 A time-line summarising different mechanical and electrophysiological experimental observations. 14
2.2 Experimental results showing reduction and the recovery of CAP over 30min post-compressive injury of guinea pig spinal cord, and computational model calibration results. 19
2.3 Electrophysiological-mechanical framework 20

3.1 Axonal membrane current models 31
3.2 3D FE internode simulation and comparison plot of propagation profiles along the axon between *Neurite*, 1D FE and 3D FE with CT boundary conditions. 39
3.3 3D FE node of Ravier simulation and comparison plot of propagation profiles along the axon between *Neurite*, 1D FE and 3D FE with HH boundary conditions. 40
3.4 Difference comparison plots of propagation profiles along the axon between *Neurite*, 1D FE and 3D FE with CT boundary conditions. 40
3.5 Difference comparison plots of propagation profiles along the axon between *Neurite*, 1D FE and 3D FE with HH boundary conditions. 41
3.6 Axon geometry and boundary conditions. 44
3.7 Resultant deformation of 500 Pa applied on 10 µm of axon. 46
3.8 Action potential propagation comparison between axon without indentation, indentation of internodal segment and nodal segment . 47
3.9 Action potential propagation comparison between 3D FE and *Neurite* simulations. 48

4.1 Schematic of membrane patch under voltage clamp in cell-attached configuration. 52
4.2 Left-shifted electrophysiological dynamics observed experimentally. 53
4.3 Geometry of cell under patch clamp. 54
4.4 Boundary conditions of cell under patch clamp. 55

4.5 Equivalent circuit for voltage clamp stimulation. 56
4.6 Displacement of bleb at maximal suction. 57
4.7 Comparison of current flowing normal to membrane with and without suction. 58
4.8 Profile of current flowing normal to membrane. 59
4.9 Comparison of voltage gradient pre and post suction. 60

5.1 Double sucrose gap set up. 65
5.2 CAP amplitudes of six loading cases during mechanical stress free relaxation 66
5.3 Geometrical relationships extracted from morphmetric studies of guinea pig axons. 67
5.4 Distribution of diameters in the nerve fibre obtained from guinea pig spinal cord axons. 68
5.5 Nerve and representative axon. 69
5.6 A case with three identical axons. 70
5.7 Compound action potential recovery simulations using 27-axon fibre model. 75
5.8 Compound action potential recovery simulations using single axon model. 76

6.1 Schematic of the constitutive hyperviscoelasticity model. 83
6.2 Model calibration with compression data. 89
6.3 Loading according to the experimental strains and strain rates. . . . 90
6.4 Experimental conduction deficit and calibrated conduction deficit. . 91
6.5 Comparison between experimental, tissue, fibre and axon model at t=0 min post loading. 92
6.6 Comparison between experimental, tissue, fibre and axon model at t=30 min post loading. 92

List of Abbreviations

TBI . . . . . Traumatic brain injury.

SCI . . . . . Spinal cord injury.

CNS . . . . . Central nervous system.

CTE . . . . . Chronic traumatic encephalopahty.

PNS . . . . . Peripheral nervous system.

K^+ . . . . . Potassium ions.

Na^+ . . . . . Sodium ions.

AP . . . . . Action potential.

Na_V **channel** . Voltage fated sodium ion channel.

K_V **channel** . . Voltage fated potassium ion channel.

CAP . . . . . Compound action potential.

TAI . . . . . Traumatic axonal injury.

DAI . . . . . Diffuse axonal injury.

mTBI . . . . . Mild traumatic brain injury.

FE . . . . . Finite element.

EEG . . . . . Electroencephalography.

Ca^{2+} . . . . . Calcium ions.

HEK . . . . . Human embryonic kidney.

4AP . . . . . 4-Aminopyridine.

HRP . . . . . Horseradish peroxidase.

TTX . . . . . Tetrodotoxin.

HH . . . . . Hodgkin-Huxley.

CT . . . . . Cable Theory.

DTI . . . . . Diffusion tensor imaging.

1 Introduction

Contents

1.1 Traumatic brain injury and spinal cord injury 1
1.2 Axons in the nervous system 3
1.3 The multiscale nature of traumatic brain injury and spinal cord injury 5
1.4 Scope of thesis 7

1.1 Traumatic brain injury and spinal cord injury

Traumatic brain injury (TBI) and spinal cord injury (SCI) are injuries in which the central nervous system (CNS) is damaged under external mechanical forces. These forces can be broadly categorised as contact and non-contact mechanical loads [4]. TBI-inducing contact forces are typically caused by direct impact, common in car accidents, contact sports and military combat settings. SCIs are usually caused by compressive force from blunt object impact or impinging bone fragments [5, 6]. Non-contact loading is more often observed in TBI and can be found in the form of rapid acceleration, deceleration, rotation of the head, or in a military blast environment [7, 8]. Immediate severe symptoms of TBIs may include loss

of consciousness, loss of reflex functions (such as corneal, pupillary and spinal reflexes), loss of control of musculature causing collapse or spasm and respiratory arrest or apnea [7]. Milder symptoms may include headache, nausea, dizziness, vomiting, restlessness, irritability and confusion [7]. Long term symptoms for TBI such as cognitive impairments of memory and attention or Chronic Traumatic Encephalopahty (CTE, a progressive neurodegenerative disease caused by repeated head injuries) are also commonly observed [9, 10]. Severe SCIs can cause loss of motor and sensory functions and impair control of limbs [11].

The aforementioned symptoms often result in neurodegeneration which can significantly reduce the quality of life of an individual and pose a huge economic burden on society and healthcare [12]. TBI is a major cause of mortality and morbidity worldwide [12, 13]. In the US, there are 1.7 million annual incidences of TBI [12], with a prevalence of 5 million individuals living with long term TBI related disabilities [14], costing over $70 billion every year [15]. Locally in England and Wales, there are approximately 1.4 million hospital visits following head injury each year [16]. While early motivations to study TBI and SCI have mainly been driven by military blast related injuries [17, 18], there has recently been increasing media attention and calls for research on sports (such as American football and boxing) related neurodegenerative diseases. A recent study showed that of those who donated their brains to this research program, 99% of professional level (National Football League) players were diagnosed with CTE [10]. There is therefore an urgency to develop methods to diagnose TBI and CTE in the living rather than post-mortem, and understand the link between the mechanically induced injury and the functional neurological outcomes. Alongside physiological [19] and molecular research and diagnostics development [20, 21], computational simulation appears as one of the promising avenues for identifying damage criteria, modelling neurological output and improving designs for protective equipment [22–24]. This thesis aims to exploit the existing pool of experimental studies on TBIs and SCIs, along with a range of computational methods to explore and develop tools for modelling mechanical-electrophysiological coupling under TBI and SCI conditions. These

tools will aim to model mechanically induced functional deficits on length scales that are relevant to different damage mechanisms in TBI and SCI. The rest of the chapter is organised as follows: Section 1.2 provides relevant background on the nervous system. Section 1.3 discusses the multiscale nature of TBI and SCI. Finally, Section 1.4 will discuss and define the scope of this thesis.

1.2 Axons in the nervous system

The nervous system is divided into CNS and peripheral nervous system (PNS) [25–27]. The CNS consists of the brain, the major information processing unit, and the spinal cord, a pathway for relaying neurological information between the brain and the PNS [28]. The fundamental cellular unit of the nervous system is a neuron [29]. Neuron morphologies can vary largely from one type to another, but they all share common components such as a cell body and neurites (axon and dendrites), see Figure 1.1. The cell body, also called soma, contains the nucleus of the neuron, which holds the DNA of the neuron and is immersed in a rheological fluid called cytoplasm [29, 30]. Neurons interact with each other via electro-chemical signals, and their neurites act as the receptors and emitters via their synapses [29]. The axon is typically elongated and transmits electrical signals over a long distance from the soma to the axon terminals [29].

Within the mammalian CNS, white and grey matter can be distinguished. The white matter is mainly composed of glial cells and axons, as opposed to the grey matter which contains mainly somas and interneurons [26]. Axons are typically periodically insulated by myelin that are provided by oligodendrocytes (a type of glial cell) [25, 26]; the regions that are myelinated are referred to as internodes ($\sim 600\,\mu m$), while the shorter exposed regions are known as nodes of Ranvier ($\sim 2\,\mu m$) [29, 31, 32].

Axonal membrane is naturally polarised, predominantly by a high concentration of intracellular potassium ions (K^+), and a high concentration of extracellular sodium ions (Na^+) [29, 31, 33]. Voltage gated ion channels distributed across the axonal membrane control the entrance and exit of various ions through the

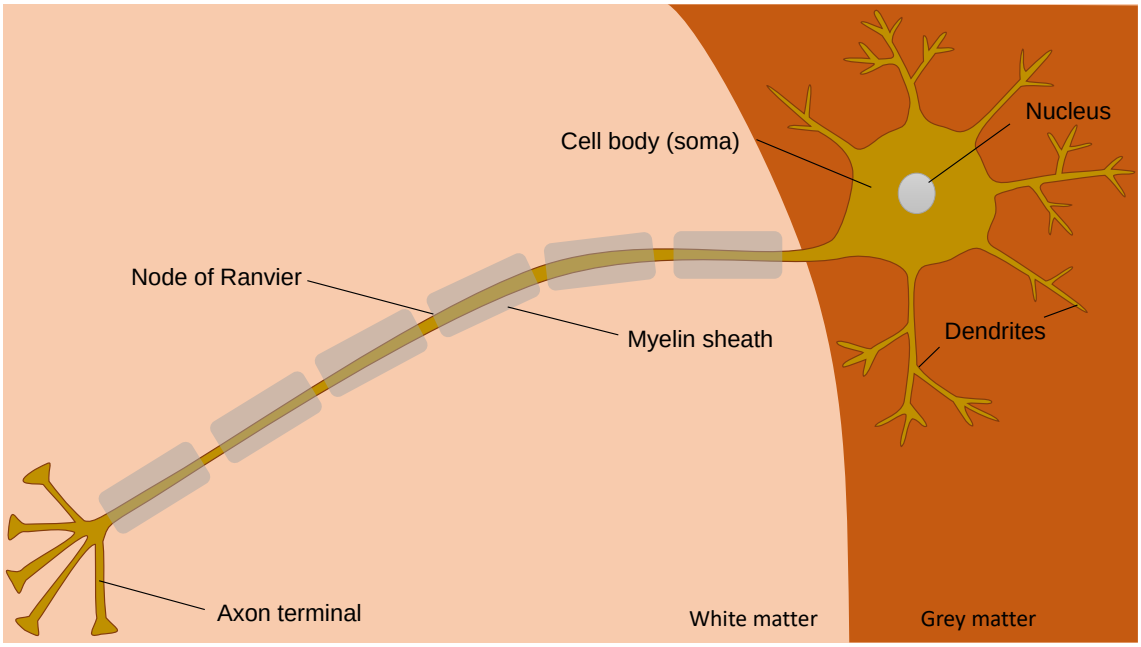

Figure 1.1: A typical axon in the white matter.

membrane. Axonal communications are based on the opening and closing of these ion channels, giving rise to an electrical impulse, known as an action potential (AP).

As a myelinated axon is stimulated, if this stimulus is larger than a certain threshold, neighbouring voltage gated sodium ion (Na_V) channels distributed in the nodes of Ranvier open to allow an influx of Na^+ through the membrane [33]. This influx of Na^+ then leads to a local depolarisation, causing further neighbouring Na_V channels to open. This eventually leads to a cascade of Na_V channels opening along the axon, thus propagating the signal [34]. If this stimulus is below the threshold, the voltage gated ion channels remain inactivated [33]. When the intracellular Na^+ level rises, and depolarises the plasma membrane, voltage gated potassium (K_V) channels open to allow a flux of K^+ to exit the axon (within 1 ms by the fast K_V channels type [35]), preventing immediate re-excitation after an AP propagation [29, 36]. In myelinated nerve fibres, the repolarisation of the axons occurs as Na_V channels inactivate and axonal current leaks to the extracellular matrix [37]. When the K_V channels finally close, the axon is temporarily more polarised than its original resting state. This phenomenon is known as hyperpolarisation [34]. The resting potential is then restored by Na^+/K^+ exchangers and fast K_V channels, returning

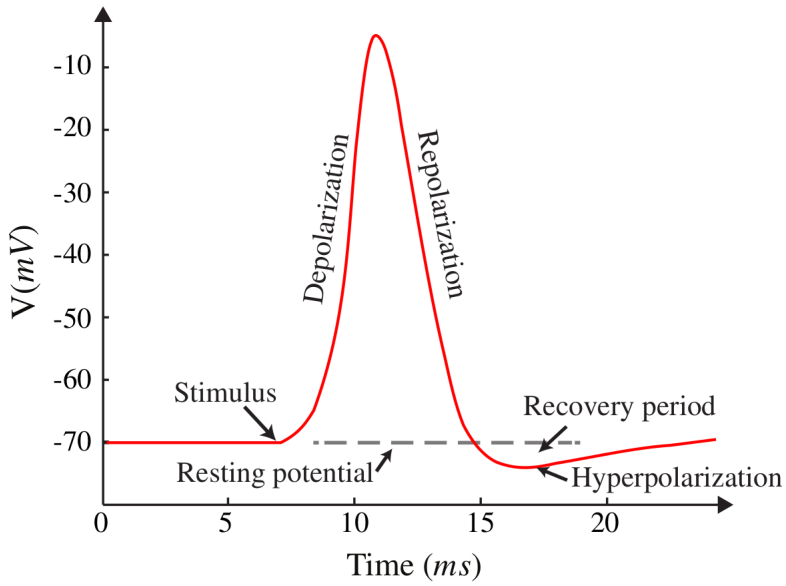

Figure 1.2: A typical AP profile. [1]

the ion concentrations to the resting level [35, 37, 38]. The time duration during which all ion channels are occupied or saturated, thus inhibiting further stimulation, is known as the refractory period. To summarise the above, an AP consists of four phases: depolarisation, repolarisation, hyperpolarisation and resting, see Figure 1.2. Bundles of axons form nerve and axonal tracts in the white matter and the collective AP measured at the tissue level is known as the compound AP (CAP) [39].

1.3 The multiscale nature of traumatic brain injury and spinal cord injury

The complex mechanisms leading to the array of clinical symptoms in TBI and SCI span across various length scales, and are currently a subject undergoing intense research. This section gives an overview on the phenomena observed at each length scale.

The brain is suspended in cerebral spinal fluid and bounded by the dura mater and pia mater (with an elastic modulus of ∼31.5 MPa and ∼11.5 MPa, respectively [40]), which protect the brain from low levels of inertia [41]. Inertia from sudden

[1] Image courtesy of Julian García-Grajales.

acceleration, deceleration and rotation at a larger scale are then translated to pressure and shearing forces at the tissue level [42]. The brain tissue and spinal cord tissue are highly inhomogenous, and white and grey matter were reported to have significantly different material properties [43–45]. Shear stiffness measured from magnetic resonance elastography of white and gray matter are reported to be 13.6kPa and 5.22kPa, respectively [43]. From brain tissue slice indentation, white matter was reported to be on average 39% stiffer than gray matter, with an average sample moduli of 1.895kPa and 1.389kPa respectively [44]. Furthermore, local vasculature also contributes to material heterogeneity, with arteries and veins reported to have stiffness of ∼20MPa and ∼3MPa, respectively [45].

Two of the main pathologies of TBI and SCI are traumatic axonal injury (TAI) or diffuse axonal injury (DAI). In TAI, the axonal tracts in the white matter are disrupted or have cellular and subcellular changes upon the application of macroscopic mechanical loads [8]. In DAI the locality of this type of axonal injury, is emphasised and is characterised by scattered white matter tracts deformation and disruption of axonal transport, which result in accumulation of axonal transport leading to swelling [4, 42].

At the cellular level, under mild TBI (mTBI) where no tissue laceration occurs, DAI is observed to be scattered rather than localised, suggesting that some structures, such as the nodes of Ranvier, maybe more vulnerable than others [41, 46]. Experimental observations have supported this theory by reporting that the CAP of myelinated axons had a better ability to recover compared to unmyelinated axons post mechanical trauma [46, 47].

Pressure and shear applied at the cellular scale further translate into forces on subcellular components. Subcellular material properties are highly inhomogeneous and widely unexplained. They depend on factors such as extracellular matrix composition, cell adhesion molecules and mechanosensitive intracellular structures [41]. Membrane tears, microtubules, neurofilaments disruptions [48] and organelles accumulations have also been observed to occur. These have been linked to

neurodegenerative cascades [49, 50], causing influx of abnormal levels of calcium ions [49] and other ion imbalances [5, 51–53].

Within the membrane, ion channels distribution have been observed to be compartmentalised in healthy axons [37, 39, 54]. Na_V channels are typically clustered at the membrane of the nodes of Ranvier [39, 54]. The paranodal junction which is positioned next to the node has a crucial role as anchorage for the myelin layers and as a septum for ion channels between nodes and internodes [29, 55]. The juxtaparanode is a region in the internode, situated directly next to the paranodal junction under the myelin layers. This is where fast K_V channels are located in highest concentrations [37, 54]. Myelin layers are adhered to the axon by cell adhesion molecules and form a tight seal with the membrane [56]. Demyelination has commonly been observed to occur after TBI [5, 57], and has been associated with K_v channels migration and exposure, which can alter the axonal electrophysiology [55].

Electrophysiology alterations from the bottom-up are believed to originate from cellular ion imbalances. These ion imbalances may lead to various phenomena observed such as axonal hyper-excitability [58], calcium ion associated degenerative cascade [49] and reduction in CAP amplitude [51], ultimately leading to larger scale network dysfunction [59] and clinical presentation such as seizure and loss of neurological functions [7].

1.4 Scope of thesis

As mentioned in the previous section, a plethora of phenomena have been observed at different scales in TBI and SCI. Chapter 2 provides a detailed review of the state-of-the-art experimental and computational research studies on mechanical-electrophysiological coupling in TAI at different length scales.

Experimental investigations are often restricted in terms of the exploration of different mechanisms and theories. Therefore, where certain investigations may be impractical to set up, it is desirable to create *in silico* models to complement experimental investigations.

It has been proposed that shear stress is a main factor contributing to axonal damage in TBI, however experiments and *in silico* models mainly focus on uniaxial loading. It is therefore crucial to explore how complex membrane strain could affect the resultant electrophysiology.

Chapter 3 therefore presents a computational tool for 3D finite element (FE) modelling of axons, which was used to demonstrate the need of modelling mechanically induced electrophysiological alteration in 3D over 1D.

At a subcellular level, there are many factors that could contribute to electrophysiology change. Some research has posited channel mechanosensitivity or irreversible damage of channels as factors contributing to this change [24]. It is often assumed that the mechanosensitivity of ion channels in patch clamp studies are the only source of electrophysiology alteration. It has however not been investigated whether the current flow under a deformed bleb would cause any change in electrophysiology propagation due to the geometry change alone. Such mechanisms are difficult to observe experimentally, and it would be insightful to explore the cause of altered electrophysiology by use of a computational model.

In Chapter 4 the mechanical-electrophysiological coupling of neuron patch clamping at a subcellular scale is studied using the aforementioned 3D FE tool. The results suggest that 3D membrane deformation may offer an alternative explanation to the "left-shift" phenomenon observed by Wang et al. [24].

At a clinically relevant level, it is useful to have models to inform about conduction blockage and alteration. For example, such models could be used to infer the level of nerve damage in upper extremity nerve injury, or to study the conduction recovery in carpel tunnel syndrome after surgical relief of pressure.

Chapter 5 therefore proposes a framework for modelling mechanical electrophysiological coupling at the fibre scale in TBI. Chapter 6 finally proposes a more general framework at the tissue level using energetic terms of the mechanical system to approach the mechanical-electrophysiological coupling. Finally Chapter 7 concludes this work and discusses future work that can stem from this research.

2

Literature Review

Contents

2.1 Experimental work 10
2.2 Computational models of damaged electrophysiology . 15
2.3 Computational modelling of mechanical damage of axon 16
2.4 Computational model coupling mechanical and electrophysiology models 18

There is a large body of both experimental and computational research on mechanically induced electrophysiological alterations of axons and neuronal tissue to address this issue. The aim of this chapter is to review the state-of-the-art experimental and computational research on this topic. Section 2.1 reviews the experimental research on cellular network and tissue scales focussing on observing the neurological changes post-TBI/SCI-equivalent mechanical loads. Section 2.2 reviews the existing computational models of TBI/SCI electrophysiology. Section 2.3 reviews the computational models of neuronal tissues and axonal mechanics. Finally, Section 2.4 gives a detailed review of models that couple the mechanics and electrophysiological alteration observed in TBI/SCI.

2.1 Experimental work

Researchers use various tools to measure electrophysiological signals and evaluate their dysfunction. Certain aspects of neuronal signalling are usually studied in order to meaningfully characterise their dysfunction, for example, the CAP amplitude, signal latency or relative excitability. These characteristics of neuronal signalling are summarised in Table 2.1. Although they are all methods and parameters for evaluating neuronal dysfunction, it is important to note that these measurements are performed on various spatial scales, or even time scales.

The physical consequences of severe cases of TBI at the organ scale can manifest themselves as contusion, ruptured blood vessels and haemorrhages [7]. For mild TBI (mTBI), visual examination of the intact brain, as well as dissected tissue slice do not explicitly reveal damage [66]. Gross pathological degeneration can only be visible microscopically by use of staining and histological methods [66]. Modalities such as diffusion tensor imaging [48], resting-state magnetoencephalography [67], scalp electroencephalography (EEG) recordings [7] have been used to demonstrate the correlation between loss of functional connectivity in different brain regions to a reduction in cognitive function in TBI patients [9, 64].

At the network scale, electrophysiological alterations are generally observed to have a reduction in overall activity. TBI-inducing stretch has been observed to disrupt and reduce the pharmacologically (bicuculline – a neurotransmitter and channel blocker used in *in vitro* studies for mimicking epilepsy.) induced synchronisations between different regions of a rat brain slice [59, 63]. Furthermore, immediately after mild injury, reduced excitation and a less connected network topology were observed *in vitro* in rat cortical neuron networks [64]. Electrophysiological dysfunctions from spinal cord white matter segments were observed to occur through reduction in CAP amplitude [17, 52], conduction velocity [36, 68] and complete conduction blocks [68]. After blast injury, CAP amplitudes of guinea pig spinal cord white matter segment were observed to reduce in a double sucrose gap [17]. After chronic clip compression, rat thoracic spinal cords were observed to have a reduced CAP amplitude, excitability and a longer refractory period [36].

Measurement	Reasoning	Measurement setup
CAP	CAP is the collective response from a bundle of axons or tissue. A reduction of CAP indicates that collectively the bundles of axons are less excitable.	CAP of a white matter segment is often measured using a double sucrose gap [36, 51, 52] or two glass pipettes with a stimulating electrode [36, 60].
Individual axon AP	The direct measurement of AP can evaluate the excitability of each axon by comparing the amplitudes of AP.	Whole cell patch clamp recordings were used to measure electrophysiology in axotomised and nonaxotomised axons [58, 61].
Conduction velocity latency	Latency between evoked potentials can reveal the slowing of conduction and an increase in refractory period of AP and CAP.	Conduction velocity of CAP was measured to significantly reduce in chronically injured dorsal columns [36]. Longer latency for AP propagation was found in rats *in vivo* AP measurement post-SCI [62].
Network excitability	Excitation response from different regions of a tissue slice is studied to evaluate dysfunction on a network's connectivity and synchronisation, this is used as a proxy for memory and information storage [59].	Tissue slice electrophysiology can be measured using microelectrode arrays, a network's synchronisation has been studied using paired electrode stimulation and excitation technique [59, 63].
Fluorescence change	An increased permeability to calcium ions (Ca^{2+}) is used as a marker of membrane damage and/or channels dysfunction. Calcium imaging is used to track and evaluate the level intracellular Ca^{2+} post-trauma.	Calcium imaging was used to study the permeability change due to traumatic stretch of human embryonic kidney (HEK) cells transfected with $Na_v1.6$ (a channel type present in axons) [24]. Calcium dynamics of single cells and network activity patterns were also studied using this technique [64, 65].

Table 2.1: Summary of published experimental measures of electrophysiological alteration.

Several studies have also observed that such electrophysiological changes are strain and strain rate dependent [52, 68, 69], where a more rapid strain rate leads to a more significant conduction deficit and membrane disruption [52, 69].

Although a generalised reduction can be observed for the overall neuronal activity, the damage response of a single cell within a network has been observed to be heterogeneous. For example, better connected neurons have been observed to be more resistant to Ca^{2+} associated injury mechanisms, which was proposed to be related to their mechanosensing GluN2B-containing NMDA receptors [64]. Furthermore, damaged axons in neuronal network subjected to equivalent TBI-inducing stretch on an elastic substrate were observed (using whole cell recording) to be less excitable, while neighbouring axons within the network exhibited three-fold increase of excitability and firing rate 30-60 min post-injury [70]. The above observations reveal the network dynamics to be complex, and therefore call for further understanding of pathophysiology and electrophysiology on a subcellular scale.

The microscopic level damage is also observed to be heterogeneous and diffused. Physical cellular abnormalities such as demyelination [69], varicosities (the enlargement of axon lumen by accumulation of organelles)[53, 71], blebbing (the detachment of membrane from the cytoskeleton cortex) [72], neurofilament change [8] are often found to concurrently accompany the aforementioned tissue level electrophysiological alterations. Conformational changes such as axonal blebbing and a decrease in number and density of structural filamentous proteins such as neurofilament and microtubule have been observed to occur less than 1min post-mechanical load [8]. Cellular change such as paranodal demyelination can also immediately be observed post-SCI, which is observed to be linked to a CAP amplitude reduction that is partially restorable by 4AP (4-Aminopyridine, a potassium channel blocker), suggesting possible K_V channels exposure after stretch injury [57].

Calcium imaging is often used to investigate membrane permeability change post-TAI [53, 73, 74], in which intra-axonal Ca^{2+} was observed immediately (within 30 s) after injury [53]. Ca^{2+} influx has been established to be associated with secondary degenerative mechanisms which is typically observed 2 h post-traumatic injury [57],

during which deleterious cascade causes physical breakage of membrane to allow entrance to large complex molecules such as dextran [73]. Calcium-mediated calpain activation has also been observed to cause proteolysis of structural proteins such as spectrin 3-6 h after injury [74, 75]. Despite the fact that intracellular Ca^{2+} influx is a well established phenomena, it is still highly debated how the aforementioned Ca^{2+} associated degenerative cascade is initiated.

Earlier studies suggested that transient intra-axonal entrance of larger molecules post-TAI can be used as evidence for membrane poration and resealing [51, 52, 76]. In an *in vitro* model of neuronal stretch, plasma membrane permeability to various large molecules was observed to increase immediately and then transiently recovers over 5-10 min after stretch [76]. Similarly permeability of large particles such as horseradish peroxidase (HRP) across the membrane was observed to be temperature dependent, with lower temperatures giving a slower resealing, and where gap potential and CAP of spinal cord axons were observed to be a function of membrane resealing [51, 52].

Some research has observed that the influx of Ca^{2+} is linked to Na_V channels [24, 53, 77]. Through transfecting HEK cells with the desired Na_V channels (HEK cells have reliable growth and are suitable for transfection, and are hence often used for studying the dynamics of specific channels), Na_V channels were observed to be subjected to a "left-shift" channel dynamics [24], effectively causing a larger influx of Na^+ post-stretch [77]. This influx of Na^+ has been observed to be tetrodotoxin (TTX, a Na_V channel blocker) sensitive [24, 53], and has been suggested to trigger the initial increase in Ca^{2+} and the subsequent proteolytic cascade [77].

Through studying the Wallerian degeneration of axons, it has been argued that the highest level of axonal Ca^{2+} levels was observed away from injury site, and therefore unlikely to be caused by mechanoporation [49, 78]. Moreover, it has also been argued that the addition of TTX does not stop axon degeneration, and therefore Na^+ influx may not be the primary cause of the neurodegenerative cascade [49, 53]. Some suggested that mitochondria [49, 79] and integrin may all have a part to play in the rise of intra-axonal Ca^{2+} [80].

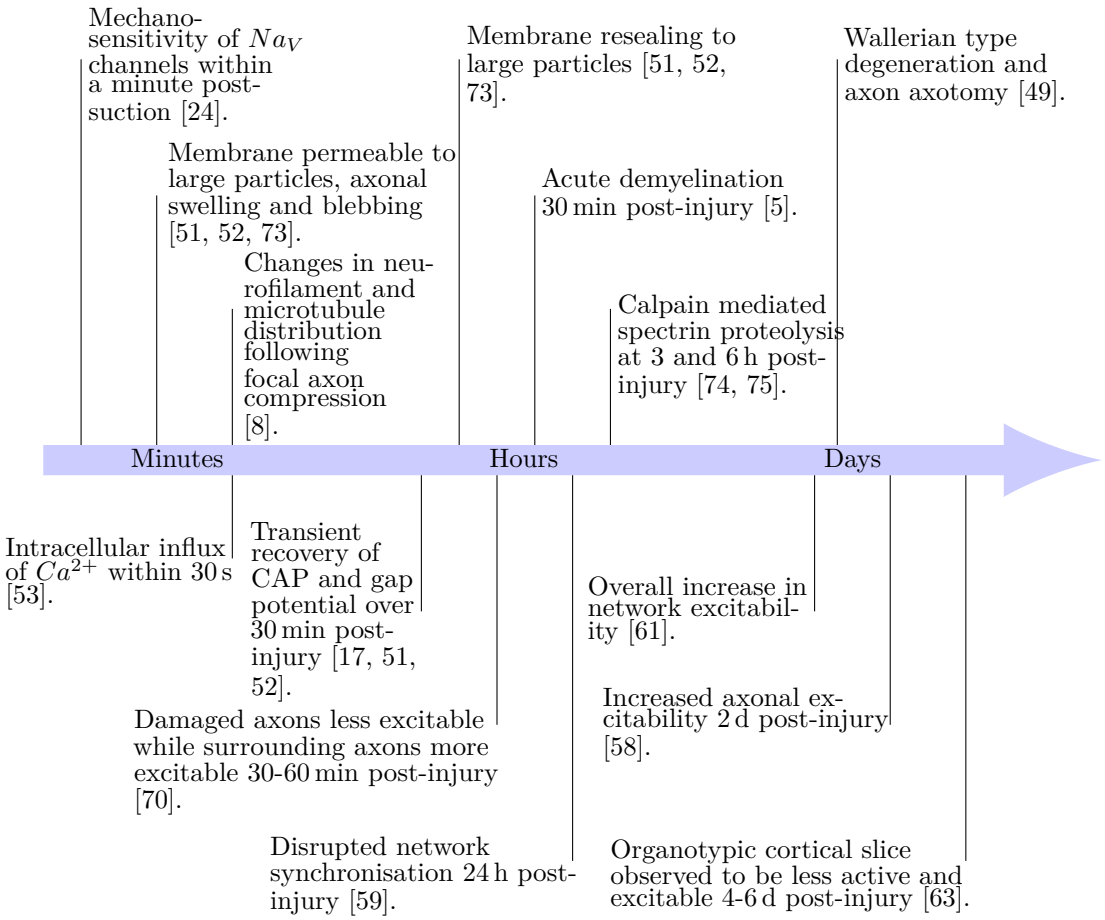

Figure 2.1: A time-line summarising different mechanical (top) and electrophysiological (bottom) experimental observations.

A time-line representation is shown in Figure 2.1 to tentatively summarise the plethora of pathological and electrophysiological observations post-TBI and SCI. The broad range of spatial scales and loading boundary conditions involved means that it is very difficult to translate observation from one scale to another, and form a quantitative outcome. To bridge this gap, there is an increasing body of computational research, creating models to capture phenomena on each scale with the aim to inform the neurological consequences at a higher scale.

Computational work has been used to model the electrophysiology and the post-TBI alterations, this is reviewed in Section 2.2. Computational efforts focussed on the mechanics of TBI are reviewed in Section 2.3. Finally computational efforts linking mechanical damage to electrophysiological dysfunction is reviewed in Section 2.4.

2.2 Computational models of damaged electrophysiology

Neuronal AP initiation and propagation have been extensively modelled computationally by software systems such as NEURON [81] and GENESIS[82], making use of the Hodgkin-Huxley (HH) and Cable Theory (CT) models in a computational framework. The research of 2D and 3D modelling of electrophysiology is driven by the fields of neurostimulation (e.g. the application of deep brain stimulation [83]) and neuroprosthesis (e.g. application to restore neuromotor function post-SCI [84]). Such applications require the understanding of propagation of electrophysiology through neural tissue. FE methods in particular have been used in several previous research studies on 3D axonal electrophysiology [85–90]. Elia et al. have studied the electrophysiology using the Maxwell equation on a 2D domain with the HH equations along a 1D membrane domain, and solved the system using the commercial multiphysics software COMSOL [85]. A similar 2D FE study of an extracellular electrical field on a compartmentalised axon model was presented by Bauer et al. by using HH equations to study how axon geometry and heterogeneous extracellular electrical fields affect the strength of the neural fields on a larger scale [86]. The above studies showed that it is possible to model the electrophysiology with the HH equations as a boundary condition with the 2D FE method, however in order to include the study of more complex scenarios, it is necessary to extend the modelling of electrophysiology to 3D. A larger four-part study accounting for extracellular electrical stimulation explored the modelling of axons with the Laplace's and CT equations solved by the Fourier spectral method, which is computationally more efficient than the FE method [87–90]. They also developed a cellular composite electrophysiology model for axon fibre bundles to study the passive electrophysiology of axons under external electrical fields. It is worth noting that only the CT equations were presented in this work. In order to study cellular ionic electrophysiological alterations, the HH equations must also be considered. While the studies mentioned above were mainly focussed on modelling the extracellular electrical stimulation,

the numerical techniques used can also be applied to the study of mechanically induced electrophysiological alterations.

In the past decade computational models of electrophysiological signal alterations due to mechanical damage have been proposed [3, 5, 24, 91–94], and they focus on capturing certain electrophysiological features observed experimentally. Some models focus on the modulation of signal transmission of axonal demyelination on electrophysiology [3, 91]. Babbs and Shi [91] used increasing node width to computationally simulate mild retraction of myelin caused by nerve stretch and crush injury, while more severe retraction and detachment of paranodal myelin were generalised by decreasing paranodal resistance in their simulation. Volman and Ng [3] proposed a compartmentalised axon model to consider the paranode and juxtaparanode, and focussed their investigation on the electrophysiological alteration caused by nodal junction demyelination as observed experimentally [5]. Boucher et al. [2] modelled trauma induced coupled "left-shift" dynamics of $Na_V1.6$ channels as observed in experiments published by Wang et al. [24] by displacing the membrane potential towards a more hyperpolarised state. The same model was used to further study the stimulation induced ectopicity [92], spontaneous excitation pattern [93] and ectopic arrhythmia [94].

The computational models mentioned above contain important features of post-electrophysiology dysfunction, however, they lack a direct link between the mechanical damage and the resulting electrophysiological deficit. Parameters quantifying the degree of damage were proposed but without relating those parameters to mechanical quantities such as stresses or strains. Also the electrophysiology model above targetted phenomena that are characteristic of each scale.

2.3 Computational modelling of mechanical damage of axon

FE methods have long been used for modelling mechanical damage in TBI, to aid understanding and approximation of the level of stresses and strains required to affect electrophysiological functions.

Whole head models are often used to approximate damage criteria for the brain, incorporating complex constitutive models and experimentally measured material properties [23, 95–99]. One difficulty with head level simulations is that it is difficult to define practical damage criteria that can be widely used. Sahoo et al. investigated different stress and strain measures as criteria for axonal damage such as brain axonal strain rate, axonal strain, first principal stress/strain and von Mises stress/strain, and concluded that axonal strain was the most appropriate predictor for DAI [23]. El Sayed et al. used shear stress as a measure for permanent shear damage for postulating the occurrence of DAI [96]. Cloots et al. and Giordano et al. both concluded that it is not possible to link axonal strains to the tissue level without the consideration of axonal orientations, and therefore proposed the use of anisotropic equivalent strain measure [97, 98].

While several examples are highlighted in the following, more constitutive models of brain tissues have been summarised in the review by de Rooij and Kuhl [100]. Variational constitutive models were used to capture elastoplastic and viscoelastic components of the brain to illustrate the diffused distribution of high stress concentrations in DAI [96]. A microscopic critical volume element approach was used to capture axonal mechanical heterogeneities in conjunction with a macroscopic head model [97]. White matter tract orientation can be observed using diffusion tensor imaging (DTI), where a hyperviscoelastic fibre-reinforced anisotropic law was used to correlate with the fractional anistropy from DTI to develop a biofidelic head model [98]. A similar approach was adopted for a model used for the reconstruction of a real-life ice hockey concussion [99], and in several studies to develop brain injury criteria [23, 99]. Other soft tissue constitutive models not only take into account strain rate dependencies, but also temperature dependencies [95].

FE modelling has also been used to model SCI, e.g., to look at the resultant stresses and strains in a spinal cord model under different impact speeds [101], or to simulate acute spinal cord compression for qualitative correlation of electrophysiological function recovery [5, 69] and cellular damage [102] post-compressive strain.

At the axonal level, simulation of nerve bundles was used to illustrate that high stress/strain concentrations may be a contributor in paranodal demyelination [5].

All of the research mentioned above works towards building a fuller picture of the multiscale biomechanics of neurons and neuronal tissue from a purely mechanical perspective. However, in order to truly understand how mechanical damage is translated into neuronal deficits, it is equally important to account for the electrophysiological deficits and its coupling with mechanical injury.

2.4 Computational model coupling mechanical and electrophysiology models

Computational models that couple the mechanics and electrophysiology directly link mechanical strain to a measure of electrophysiological damage. Jérusalem et al. [1] proposed a 1D finite difference model to capture the strain and strain rate dependence of electrophysiological alteration by proposing that the Na_V and K_V channels "leakiness" and dynamics are related to the plastic strain in the membrane. This model focussed on capturing the recovery of CAP amplitude from 0-30min post-white matter stretch in experiments conducted in a double sucrose gap by Shi and Whitebone [52]. Under mild (ε=25%), moderate (ε=50%) and severe (ε=100%) strain and strain rates (slow, $\dot{\varepsilon}$=0.006-0.008s^{-1} and fast, $\dot{\varepsilon}$=355-519s^{-1}), various levels of CAP reduction and near complete conduction block were observed. The model calibration and the experimental results are summarised in Figure 2.2.

The mechanical model in the coupled framework by Jérusalem et al. is governed by η_1, η_2 and E, which are respectively the viscoelasticity at the microscopic level (the active reorganisation of the molecules of the membrane from growth and tissue reorganisation), the viscoelasticity at the macroscopic level (which incorporates linkage to extracellular scaffold or structure), and the Young's modulus. The microscopic axial axonal strain is denoted by $\varepsilon_{m,a}$ and the overall macroscopic axial strain by ε_a. The microscopic damage strain $\varepsilon_{D,a}$ occurs as axonal stress σ_1 exceeds a threshold σ_0 at which the axon becomes permanently deformed following a plasticity-type law. The mechanical model is described by the following system

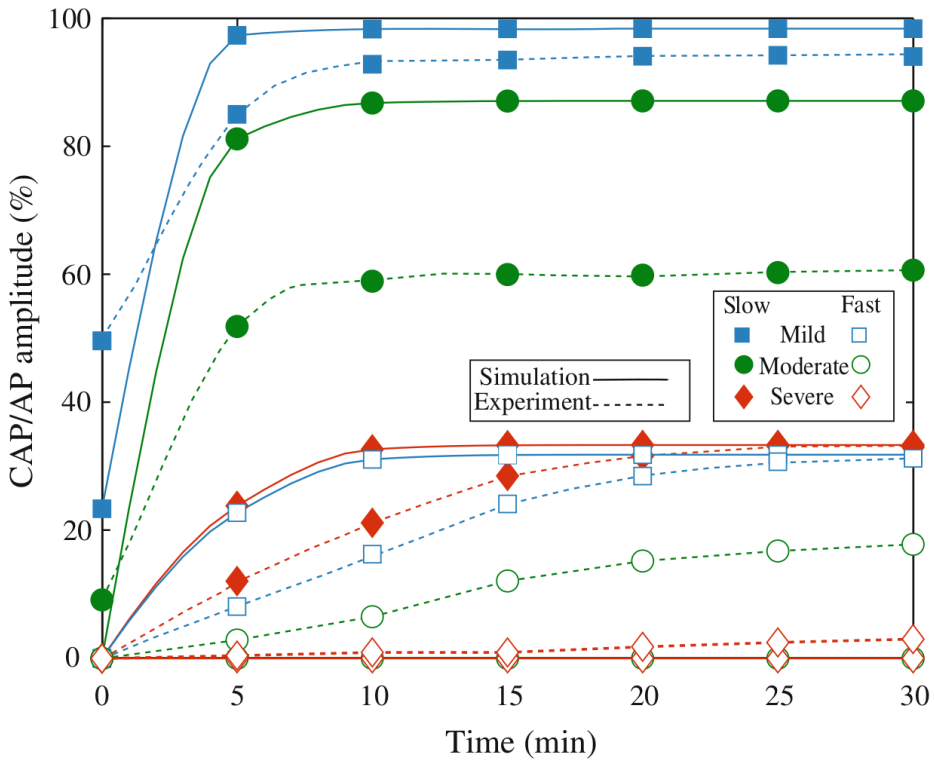

Figure 2.2: Experimental results of Shi et al. showing reduction and the recovery of CAP over 30min post-compressive injury of guinea pig spinal cord, and computational model calibration results by Jerusalem et al. [1].

of equations and the equivalent spring damper diagram is labelled as ① in Fig. 2.3 and mathematically expressed in Equation 2.1:

$$\begin{aligned}
&\sigma_1 = E(\varepsilon_{m,a} - \varepsilon_{D,a}) \\
&\sigma_1 = \eta_1(\dot{\varepsilon}_a - \dot{\varepsilon}_{m,a}) \\
&\sigma_2 = \eta_2 \dot{\varepsilon}_a \\
&\sigma = \sigma_1 + \sigma_2 \\
&\begin{cases} \dot{\varepsilon}_{D,a} = 0 & \text{if } \sigma_1 < \sigma_0 + k\varepsilon_{D,a} \\ \sigma_1 = \sigma_0 + k\varepsilon_{D,a} & \text{otherwise} \end{cases}
\end{aligned} \tag{2.1}$$

The mechanical and electrophysiological models are coupled by the axonal geometry. As the axon deforms, the conductances change according to geometrical parameters such as diameter, internodal length, node size and myelin thickness, see ② in Fig. 2.3. In this study it was assumed that the axons are bound tightly together and that the extracellular cross-linking links all the axons together perfectly as if they were homogenous mechanically. Therefore the strains experienced by

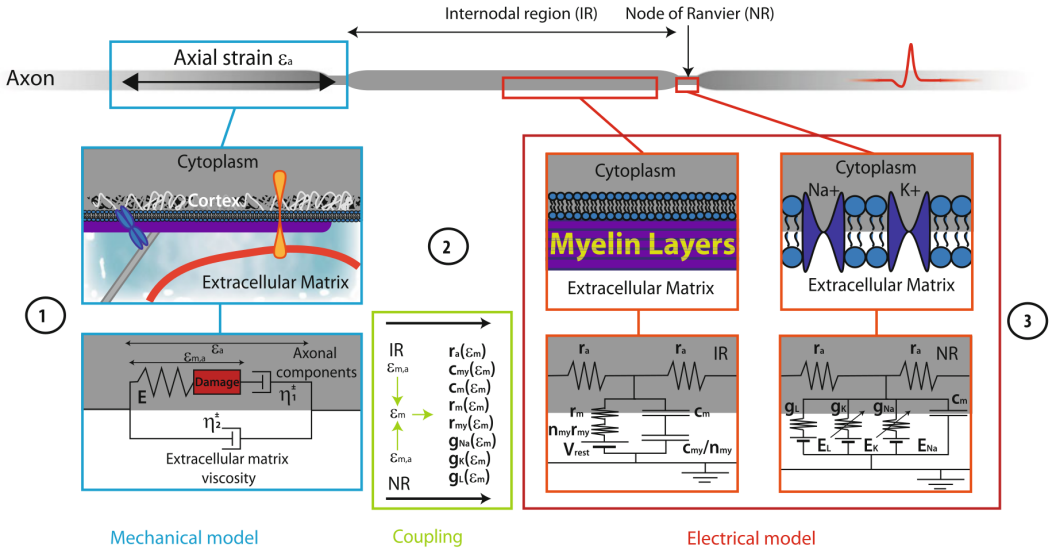

Figure 2.3: Electrophysiological-mechanical framework by Jerusalem et al. [1]: ① mechanical model, ② coupling model (relating strain parameters to geometrical and electrophysiological alterations), ③ electrophysiological model.

the internodal regions are assumed to be the same as the strains experienced by the nodes of Ranvier:

$$\varepsilon_{m,a}^{node} = \varepsilon_{m,a}^{internode} = \varepsilon_{m,a} \tag{2.2}$$

Note that this approximation may not be a realistic assumption, as the material properties of nodes and internodes are known to be different (internodes are protected by mechanically stronger myelin). Note that it is possible to differentiate the relative strain of nodes and internodes within this framework, however this was not done by the authors. Equivalent stress was not used in this case as axonal strain can more readily be evaluated compared to axonal damage.

As the axons are assumed to be incompressible, the microscopic membrane strain is linked to the microscopic axial strain and the relationships for original axon diameter d_0 and deformed axon diameter d are given by:

$$1 + \varepsilon_m = \sqrt{1 + \varepsilon_{m,a}} \tag{2.3}$$

Note that ε_m is the surface strain, which was approximated by the authors assuming $\varepsilon_m = \frac{a-a_0}{a_0}$, where a_0 and a are the original and the deformed surface

area of the membrane respectively.

$$d = \frac{d_0}{\sqrt{1+\varepsilon_{m,a}}} \tag{2.4}$$

Using the CT and HH models, axons are simulated as passive cable and short patches of excitable membrane to represent the internodal regions and the nodes of Ranvier, respectively, see ③ in Fig. 2.3. Both models can be represented by the following partial differential equation.

$$A\frac{\partial^2 V}{\partial x^2} = B\frac{\partial V}{\partial t} + CV + D \tag{2.5}$$

where V is the membrane potential, and A, B, C and D are listed in Table 1. The CT parameters are dependent on the resting potential V_{rest}, the axial resistivity of axon cytoplasm ρ_a, the membrane resistivity ρ_m, the myelin sheaths resistivities ρ_{my} and the equivalent electric constants of cell membrane and myelin sheaths C_m and C_{my}.

The HH model parameters involve the axial resistivity of axon cytoplasm ρ_a, the equivalent electric constants of the cell membrane C_m, the variable conductances G_{Na} and G_K for Na channels and K_V channels and their corresponding potentials E_{Na} and E_K, along with a leak potential and conductance E_L and G_L.

Table 2.2: PDE model parameters [1].

Parameter	Cable theory	Hodgkin-Huxley
A	$\frac{\pi d_0^2}{4\rho_a}$	$\frac{\pi d_0^2}{4\rho_a}$
B	$\left(\frac{h_0}{C_m \pi d_0} + \sum_{i=1}^{n_{my}} \frac{h_{my,o}}{C_{my}\pi d^i_{my,0}}\right)^{-1}$	$\frac{C_m \pi d_0}{h_0}$
C	$\frac{\pi}{\frac{\rho_m h_0}{d_0} + \sum_{i=1}^{n_{my}} \frac{\rho_{my} h_{my,0}}{d^i_{my,0}}}$	$\frac{\pi d_0}{h_0}(G_L + G_{Na} + G_K)$
D	$\frac{-\pi V_{rest}}{\frac{\rho_m h_0}{d_0} + \sum_{i=1}^{n_{my}} \frac{\rho_{my} h_{my,0}}{d^i_{my,0}}}$	$\frac{-\pi d_0}{h_0}(G_L E_L + G_{Na} E_{Na} + G_K E_K)$

The leakage potential is defined as the following:

$$E_L = \left(1 + \frac{G_{Na}}{G_L} + \frac{G_K}{G_L}\right) V_{rest} - \frac{(G_{Na}E_{Na} + G_K E_K)}{G_L} \tag{2.6}$$

The variable conductances are dependent on the states of their corresponding ion channels. The state (open or closed) of the channels is controlled by gating particles n, m and h. The probabilities of the gating particles being open or closed are time and voltage dependent, and the expressions are summarised in Table 2.

Table 2.3: Na_V and K_V channels conductance voltage, time dependent equations [1].

Na_V	K_V
$G_{Na}(V) = \overline{G}_{Na} m^3 h$	$G_K(V) = \overline{G}_K n^4$
$\frac{dm}{dt} = \alpha_m(V)(1-m) - \beta_m(V)m$ $\frac{dh}{dt} = \alpha_h(V)(1-h) - \beta_h(V)h$	$\frac{dn}{dt} = \alpha_n(V)(1-n) - \beta_n(V)n$
$\alpha_m(V) = \frac{25-(V-V_{rest}}{10(e^{(25-(V-V_{rest}))/10}-1)}$ $\alpha_h(V) = 0.07e^{-(V-V_{rest})/20}$	$\alpha_n(V) = \frac{10-(V-V_{rest}}{100(e^{(10-(V-V_{rest}))/10}-1)}$
$\beta_m(V) = 4e^{-(V-V_{rest})/18}$ $\beta_h(V) = \frac{1}{e^{(30-(V-V_{rest}))/10}+1}$	$\beta_n(V) = 0.125e^{-(V-V_{rest})/80}$

The electrophysiological damage model postulates in Ref. [1] that the functionalities of both Na_V and K_V channels are affected by the microscopic membrane strain. As $\varepsilon_{D,a}$ increases, the ion channels becomes increasingly damaged and "leaky", thus affecting the E_{Na} and E_K. The system of equations describing the electrophysiology after damage is given by the following:

$$\begin{cases} E_{Na}(\varepsilon_m) = \begin{cases} E_{Na,0}(1 - (\frac{\varepsilon_m}{\tilde{\varepsilon}})^\gamma), & \text{if } \varepsilon_m < \tilde{\varepsilon} \\ 0, & \text{else} \end{cases} \\ E_K(\varepsilon_m) = \begin{cases} E_{K,0}(1 - (\frac{\varepsilon_m}{\tilde{\varepsilon}})^\gamma), & \text{if } \varepsilon_m < \tilde{\varepsilon} \\ 0, & \text{else} \end{cases} \end{cases} \tag{2.7}$$

$$
\begin{aligned}
\alpha_m(V,\varepsilon_m) &= \begin{cases} \alpha_m(V+\frac{\varepsilon_m}{\tilde{\varepsilon}}{}^{\gamma}E_{Na,0}), & \text{if } \varepsilon_m < \tilde{\varepsilon} \\ \alpha_m(V+E_{Na},0), & \text{else} \end{cases} \\
\alpha_h(V,\varepsilon_m) &= \begin{cases} \alpha_h(V+\frac{\varepsilon_m}{\tilde{\varepsilon}}{}^{\gamma}E_{Na,0}), & \text{if } \varepsilon_m < \tilde{\varepsilon} \\ \alpha_h(V+E_{Na},0), & \text{else} \end{cases} \\
\beta_m(V,\varepsilon_m) &= \begin{cases} \beta_m(V+\frac{\varepsilon_m}{\tilde{\varepsilon}}{}^{\gamma}E_{Na,0}), & \text{if } \varepsilon_m < \tilde{\varepsilon} \\ \beta_m(V+E_{Na},0), & \text{else} \end{cases} \\
\beta_h(V,\varepsilon_m) &= \begin{cases} \beta_h(V+\frac{\varepsilon_m}{\tilde{\varepsilon}}{}^{\gamma}E_{Na,0}), & \text{if } \varepsilon_m < \tilde{\varepsilon} \\ \beta_h(V+E_{Na},0), & \text{else} \end{cases} \\
\alpha_n(V,\varepsilon_m) &= \begin{cases} \alpha_n(V+\frac{\varepsilon_m}{\tilde{\varepsilon}}{}^{\gamma}E_{K,0}), & \text{if } \varepsilon_m < \tilde{\varepsilon} \\ \alpha_n(V+E_{K},0), & \text{else} \end{cases} \\
\beta_n(V,\varepsilon_m) &= \begin{cases} \beta_n(V+\frac{\varepsilon_m}{\tilde{\varepsilon}}{}^{\gamma}E_{K,0}), & \text{if } \varepsilon_m < \tilde{\varepsilon} \\ \beta_n(V+E_{K},0), & \text{else} \end{cases}
\end{aligned}
\tag{2.8}
$$

where $\tilde{\varepsilon}$ is the microscopic strain threshold at which the ion channels are fully damaged.

The model detailed above was the first of its kind to link the electrophysiological alteration to membrane strain, and also takes into account that electrophysiological changes are rate dependent. This model however shares the same limitation with other 1D model formulations that couple electrostriction to electrophysiology [103, 104]. An axisymmetry assumption means that these models can only capture simple uniaxial loading and deformation and therefore have limited applications.

In order to study axonal electrophysiological alteration induced by non-axisymmetric mechanical deformations, the 3D FE method has been considered. Recent work by Cinelli et al. [105–108] proposed the use of electro-thermal equivalences and piezoelectric effect to couple mechanics and electrophysiology in nerves. Their model was implemented in the commercial software ABAQUS and considers the extracellular matrix, membrane and intracellular matrix as separate domains. The strain based electrophysiology damage model proposed by Jérusalem et al. [1] was adopted in this model, and the resultant electrophysiological signals of a nerve bundle under various degrees of uniaxial stretch were presented. The three element type model may be advantageous for studying the near-field scaling of electrophysiology from axon to nerve tissue level. The drawback of this approach however is that

discretising the membrane (being a relative thin structure compare to other axonal components) in such a model is computationally costly.

A generalised multiscale framework published recently by Ng et al. [22] was the first work to link mechanically altered electrophysiological dysfunction models from cellular, network and head scales. In this framework whole head FE models were used to obtain stresses and strains in the corpus callosum, along with a rate-dependent composite model to capture the micromechanics of the axonal tract structures within the corpus callosum. Furthermore, a biophysical signalling model based on the coupled "left-shift" model is coupled with the micromechanics model to capture the altered membrane dynamics. Finally, a neuronal network model was used to illustrate a slower neuronal network which was reported to be consistent with observations with quantitative EEG. Although this is a pioneering framework attempting to link the damage phenomena at various scales that has been observed to be crucial in TBI, it is only validated with a very limited set of boundary conditions. Furthermore this validation is limited to tension, while shearing is known to be the more damaging form of loading in axonopathy.

To date the most common ways to clinically evaluate the neurological consequences after an episode of TBI or SCI are based on neuroimaging, neurocognitive and vestibular tests. There is no quantitative and non-invasive way to evaluate the tissue damage due to an episode of TBI or SCI. There is currently a lack of i) 3D models investigating mechanically induced electrophysiological alterations and ii) models investigating how electrophysiological dysfunction link from one scale to another. To this end, this thesis set out to address both of those issues. Firstly Chapter 3 will be dedicated to developing a framework for 3D modelling of mechanically induced axonal electrophysiology that allows for capturing complex boundary conditions that arise from experimental investigations. Chapter 4 is dedicated to the application of this framework in modelling the coupled "left-shift" effect which occurs in electrophysiology patch clamping. The physical organisation of the neuronal network is intricate: a traumatising mechanical impact will not only cause structural disruption, but also functional disruption throughout the

tissue, network, axon and subcellular scales. Furthermore, it is not well established how electrophysiology disruption at a lower scale may translate in a measurement obtained on a higher scale. To address the issue of multiscale, Chapter 5 present a scaling model based on the software system *Neurite* by Jerusalem et al. [1]. Chapter 6 presents a generalised model formulated based on energies for coupling mechanics and electrophysiology on a tissue level. Finally Chapter 7 concludes the findings of this thesis and discuss the future work of this research.

3
3D axon model

Contents

3.1 Finite element framework 29
3.1.1 Mechanics 29
3.1.2 Electrophysiology 30
3.1.3 Coupled problem 35
3.2 Boundary conditions implementation and verification 37
3.2.1 Implementation 37
3.2.2 Verification 39
3.3 Axonal indentation 41
3.3.1 Simulation setup 43
3.3.2 Results and discussion 45
3.3.3 Comparison of coupled "left-shift" theory between 1D and 3D models 48

The material and figures presented here are extracted from a submitted article that is currently under review [109] .

In TBIs and SCIs, the CNS is subjected to multiple mechanical loading modes, such as stretch, compression, shear or a combination of those [18, 110, 111]. These mechanical disturbances compromise the structural integrity of the tissue and underlying cells, in turn inducing electrophysiological alterations at various scales [5, 24, 52, 57, 58, 69, 70, 112, 113].

In order to study the electrophysiological alterations induced by mechanical

loading at the tissue and cellular scale, experimental setups have been proposed to control the mechanical loading of a specimen in order to relate its relationship with the altered electrophysiology. However, experimental setups that will allow the application of load and the subsequent measurement of electrophysiology on the same specimen are limited. For example in Shi et al.[52], the experimental measurement of spinal cord electrophysiology after stretching in a double sucrose gap is done such that the nerve segment is clamped at two ends while a strain rod impacts the spinal cord vertically. In fact such a form of stretching consists of more loading modes than uniaxial tension; the specimen also experiences compression and shear forces at the site of indentation. Therefore if the electrophysiological alteration is linked to the strain that the membrane is experiencing, this may not be straightforwardly simplified to a 1D system. Another example is the method for measuring electrophysiology at the subcellular scale during and after membrane suction in a pipette [24]. While the membrane experiences tension and shear under suction, the resulting strain (and geometry) of the membrane are often not considered to be a factor for electrophysiology change. It is unclear in the examples above that modelling the mechanics and (or) the electrophysiology in 1D is sufficient.

In this chapter, a FE framework with an additional degree of freedom, electrical potential, is presented. This framework uses the Poisson's equation (for describing the potential field as a result of a charge density distribution) as a governing potential equation for axoplasm. This framework also models AP propagation at the internodal and nodal membrane by introducing electro-mechanically coupled boundary conditions (modelled by the CT [114] and HH [115] models respectively) directly in the weak form of the FE model. The above aims to provide a flexible way to model axonal electrophysiological alteration directly induced by 3D non-axisymmetric mechanical deformations. The advantage of this approach is its ability to incorporate phenomenological electrophysiological equations into a 3D framework without the explicit inclusion of extra 3D membrane elements. Details of the governing equations and the FE formulation are presented in Section 3.1. The verification of CT and HH equations implementation in the open source FE

platform Gmsh [116, 117] is presented in Section 3.2. Finally, Section 3.3 illustrates the flexibility of the method with a study of axonal indentation.

3.1 Finite element framework

3.1.1 Mechanics

For a material point of coordinate $\mathbf{X}$ in the reference configuration Ω_0 and of coordinate $\mathbf{x}$ in the current configuration Ω, the balance of linear momentum reads:

$$\mathrm{Div}\,\mathbf{P}(\mathbf{X}) + \rho_0\mathbf{b} = \rho_0\ddot{\mathbf{x}}(\mathbf{X}) \tag{3.1}$$

where $\mathbf{P}$ is the first Piola-Kirchhoff stress, ρ_o is the material density, $\mathbf{b}$ is the body force in the reference configuration, and "Div" is the divergence operator formulated in the reference configuration. Note that body forces imposed by gravitational, electrical and magnetic fields are assumed to be negligible in the applications presented in this thesis, and are therefore not considered in the framework presented below. In indicial notation, Equation (3.1) reads:

$$P_{iJ,J} + \rho_0 b_i = \rho_0 \ddot{x}_i \tag{3.2}$$

The Neumann and Dirichlet boundary conditions on the corresponding boundaries $\partial\Omega_0^n$ and $\partial\Omega_0^d$ can be formulated as follows:

$$\begin{cases} \mathbf{P}\cdot\mathbf{N} = \bar{\mathbf{T}}, & \forall \mathbf{X} \in \partial\Omega_0^n \\ \mathbf{u} = \bar{\mathbf{u}}, & \forall \mathbf{X} \in \partial\Omega_0^d \end{cases} \tag{3.3}$$

where $\mathbf{u} = \mathbf{x} - \mathbf{X}$ is the material point displacement, $\mathbf{N}$ is the boundary normal, and $\bar{\mathbf{T}}$ is the imposed traction and $\bar{\mathbf{u}}$ is the displacement on their respective boundaries in the reference configuration.

For all admissible virtual displacements $\boldsymbol{\eta}$, the weak form of the mechanics is as follows:

$$a_{\mathbf{uu}}(\mathbf{u}, \boldsymbol{\eta}) = l_{\mathbf{u}}(\boldsymbol{\eta}) \tag{3.4}$$

where $a_{\mathbf{uu}}$ and $l_{\mathbf{u}}$ represent the bilinear form of the weak formulation of the mechanical problem, defined as below:

$$\begin{cases} a_{\mathbf{uu}}(\mathbf{u}, \boldsymbol{\eta}) = \iiint_{\Omega_0} P_{iJ}(\mathbf{u})\eta_{i,J} dV_0 \\ l_{\mathbf{u}}(\boldsymbol{\eta}) = \iiint_{\Omega_0} \rho_0 b_i \eta_i dV_0 + \iint_{\partial\Omega_0^n} \bar{T}_i \eta_i dS_0 \end{cases} \tag{3.5}$$

Note that, without loss of generality, the dynamic term is dropped here and subsequently.

The final FE problem for the mechanical part is defined by:

$$\mathbf{F}_{\mathbf{u}}^{ext} = \mathbf{F}_{\mathbf{u}}^{int} \tag{3.6}$$

where the mechanical external and internal force vectors $\mathbf{F}_{\mathbf{u}}^{ext}$ and $\mathbf{F}_{\mathbf{u}}^{int}$ are given by:

$$\begin{cases} F_{\mathbf{u},ia}^{ext} &= \iiint_{\Omega_0} \rho_0 b_i N_a dV_0 + \iint_{\partial\Omega_0^n} \bar{T}_i N_a dS_0 \\ F_{\mathbf{u},ia}^{int} &= \iiint_{\Omega_0} P_{iJ}(\mathbf{u_h}) N_{a,J} dV_0 \end{cases} \tag{3.7}$$

where the FE displacement vector $\mathbf{u}_h$ is estimated from the FE nodal displacement vector $\mathbf{u}_a$ by use of the shape functions N_a:

$$\mathbf{u}_h = \Sigma_a N_a(\mathbf{X}) \mathbf{u}_a \tag{3.8}$$

Note that P_{iJ} is directly dependent on $\mathbf{F}_{iJ}$, the deformation gradient. $\mathbf{F}_{iJ}$ can be written in terms of the displacements, and is estimated at the gauss points, given by (3.10):

$$\mathbf{F}_{iJ} = \mathbf{X}_{i,J} + \mathbf{u}_{i,J}(\mathbf{X}, t) \tag{3.9}$$

$$\mathbf{F}_{iJ} = I + \Sigma_a N_{a,J} \mathbf{u}_a^i \tag{3.10}$$

3.1.2 Electrophysiology

The potential $V(\mathbf{x})$ in a material of constant permittivity ϵ_0. This is described at all material points of the body B in the current configuration by Poisson's equation:

$$\Delta V = s(\mathbf{x}) = \frac{-\tilde{\rho}}{\epsilon_0} \tag{3.11}$$

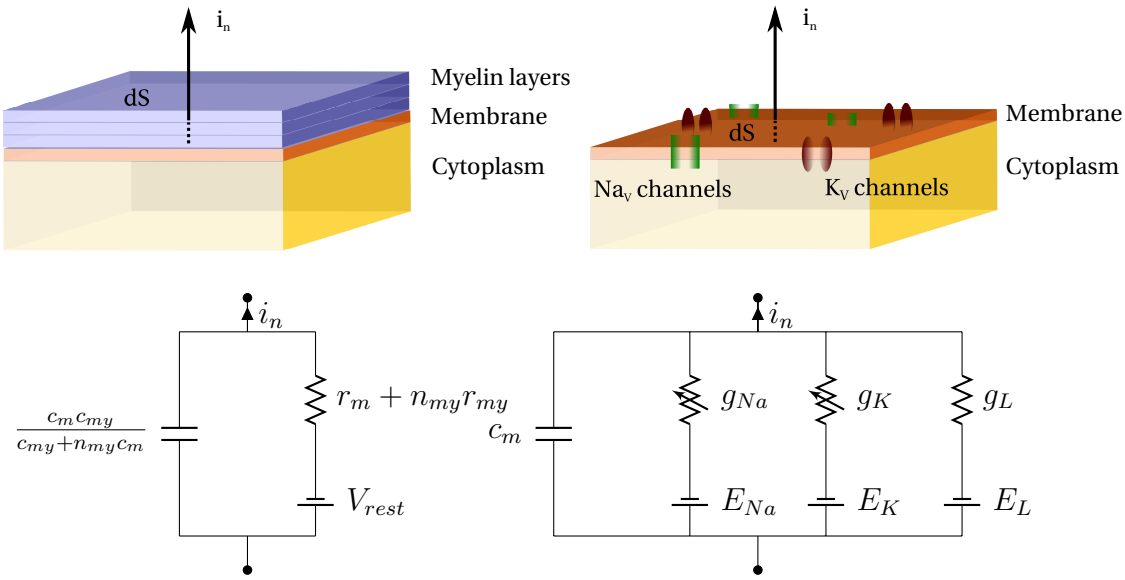

(a) Internode (b) Node

Figure 3.1: Axonal membrane outward current flux, a) either impeded by myelin layers in the internodal regions, b) or governed by the dynamics of the gating of the Na_V and K_V channels in the nodes of Ranvier, modelled by the CT and HH models, respectively.

where "Δ" is the Laplace operator, $s(\mathbf{x})$ is the "source term", here in the cytoplasm we assume a region where there are no charges or current source, $\tilde{\rho}$ is neglected as a first approximation (i.e. $\tilde{\rho} = 0$) and Equation (3.11) is reduced to Laplace's equation ($\Delta V = 0$). However, $s(\mathbf{x})$ may be desirable in some cases, e.g., when considering secondary injury mechanisms associated with mitochondrial calcium transport disruption. Enhanced Ca^{2+} buffering capacity was observed in Wallerian type degeneration [118, 119], and mitochondria may be considered both as a current sink and source within the cytoplasm.

The electrophysiological boundary conditions of the deformed body B were assumed to either be passive (CT model) or active (HH model), where the internodal region ($\partial\Omega^{CT}$) is enveloped by successive layers of myelin, and the node of Ranvier region ($\partial\Omega^{HH}$) is an active membrane with Na_V and K_V ion channels given free access to the extracellular medium, see Figure 3.1.

The current i_n flowing out of a patch of membrane surface dS with a potential V follows the relation:

$$i_n = -\frac{dS}{\rho_c}\nabla_{\mathbf{n}} V, \ \forall \mathbf{x} \in \partial\Omega^{CT} \cup \partial\Omega^{HH} \tag{3.12}$$

where $\nabla_{\mathbf{n}}$ is the differential operator in the normal direction to the membrane (pointing away from the cell) in the current configuration, i.e. $\nabla_{\mathbf{n}} = \nabla \cdot \mathbf{n}$.

The identification of i_n in both models (see CT and HH models in Figure 3.1) for a patch of membrane of area dS leads to:

$$\begin{cases} i_n = \frac{c_m c_{my}}{c_{my}+n_{my}c_m}\frac{\partial V}{\partial t} + \frac{1}{r_m+n_{my}r_{my}}(V - V_{rest}), & \forall \mathbf{x} \in \partial\Omega^{CT} \\ i_n = c_m\frac{\partial V}{\partial t} + g_{Na}(V - E_{Na}) + g_K(V - E_K) + g_L(V - E_L), & \forall \mathbf{x} \in \partial\Omega^{HH} \end{cases} \tag{3.13}$$

where r_m and c_m are the membrane resistance and capacitance, and r_{my} and c_{my} are the individual myelin layer's resistance and capacitance for n_{my} number of layers. V_{rest} is the resting potential. g_{Na}, g_K and g_L are the Na_V and K_V ion channels, and leak conductances; E_{Na} and E_K are their reversal potentials. Their relationship with the specific membrane and myelin layer resistivities, ρ_m and ρ_{my}, membrane and myelin layer equivalent electric constants, C_m and C_{my}, and dynamic conductances $G_{Na}(V, \varepsilon_s)$, $G_K(V, \varepsilon_s)$ are listed below:

$$\begin{cases} g_{Na} = \dfrac{dSG_{Na}}{h_m}, g_K = \dfrac{dSG_K}{h_m}, g_L = \dfrac{dSG_L}{h_m} \\ r_m = \dfrac{\rho_m h_m}{dS}, r_{my} = \dfrac{\rho_{my} h_{my}}{dS} \\ c_m = \dfrac{dSC_m}{h_m}, c_{my} = \dfrac{dSC_{my}}{h_{my}} \end{cases} \tag{3.14}$$

where h_m and h_{my} are the membrane and myelin layer thicknesses. Here the channel conductances are expressed with respect to the surface area in the current configuration, dS, however, g_{Na} and g_K can also be calculated with respect to dS_0, which will later be used to consider a patch of active membrane with a conserved number of ion channels.

The dynamic conductances G_{Na} and G_K are functions of the time-dependent membrane potential V, and two reference values $\overline{G}_{Na}$ and $\overline{G}_K$ [33, 120], see Table 3.1. In this table, the dimensionless activation (m and n) and inactivation (h) states describe the evolution of the corresponding conductances as a function of the rate constants α_k and β_k for $k \in \{m, h, n\}$. The states need to be simultaneously open in a given configuration (3 m's and 1 h for Na_v; 4 n's for K_v) to allow for the full opening of the gate, see Refs. [120] and [33] for further information.

Table 3.1: Na and K ion channel Hodgkin-Huxley evolution equations (potential and time units are respectively mV and ms in this table).

$\mathbf{Na_V}$	$\mathbf{K_V}$
$G_{Na}(V,\varepsilon_s) = \bar{G}_{Na} m^3 h$	$G_K(V,\varepsilon_s) = \bar{G}_K n^4$
$\frac{dm}{dt} = \alpha_m(V,\varepsilon_s)(1-m) - \beta_m(V,\varepsilon_s)m,\ m_0 = \frac{\alpha_{m,0}}{\alpha_{m,0}+\beta_{m,0}}$ $\frac{dh}{dt} = \alpha_h(V,\varepsilon_s)(1-h) - \beta_h(V,\varepsilon_s)h,\ h_0 = \frac{\alpha_{h,0}}{\alpha_{h,0}+\beta_{h,0}}$	$\frac{dn}{dt} = \alpha_n(V,\varepsilon_s)(1-n) - \beta_n(V,\varepsilon_s)n,\ n_0 = \frac{\alpha_{n,0}}{\alpha_{n,0}+\beta_{n,0}}$
$\alpha_m(V,\varepsilon_s) = \begin{cases} \alpha_{m,0}\left(V + \left(\frac{\varepsilon_s}{\tilde{\varepsilon}}\right)^\gamma E^0_{Na}\right), \text{ if } \varepsilon_s < \tilde{\varepsilon} \\ \alpha_{m,0}(E^0_{Na}), \text{ else} \end{cases}$ $\alpha_h(V,\varepsilon_s) = \begin{cases} \alpha_{h,0}\left(V + \left(\frac{\varepsilon_s}{\tilde{\varepsilon}}\right)^\gamma E^0_{Na}\right), \text{ if } \varepsilon_s < \tilde{\varepsilon} \\ \alpha_{h,0}(E^0_{Na}), \text{ else} \end{cases}$ $\beta_m(V,\varepsilon_s) = \begin{cases} \beta_{m,0}\left(V + \left(\frac{\varepsilon_s}{\tilde{\varepsilon}}\right)^\gamma E^0_{Na}\right), \text{ if } \varepsilon_s < \tilde{\varepsilon} \\ \beta_{m,0}(E^0_{Na}), \text{ else} \end{cases}$ $\beta_h(V,\varepsilon_s) = \begin{cases} \beta_{h,0}\left(V + \left(\frac{\varepsilon_s}{\tilde{\varepsilon}}\right)^\gamma E^0_{Na}\right), \text{ if } \varepsilon_s < \tilde{\varepsilon} \\ \beta_{h,0}(E^0_{Na}), \text{ else} \end{cases}$	$\alpha_n(V,\varepsilon_s) = \begin{cases} \alpha_{n,0}\left(V + \left(\frac{\varepsilon_s}{\tilde{\varepsilon}}\right)^\gamma E^0_{K}\right), \text{ if } \varepsilon_s < \tilde{\varepsilon} \\ \alpha_{n,0}(E^0_{K}), \text{ else} \end{cases}$ $\beta_n(V,\varepsilon_s) = \begin{cases} \beta_{n,0}\left(V + \left(\frac{\varepsilon_s}{\tilde{\varepsilon}}\right)^\gamma E^0_{K}\right), \text{ if } \varepsilon_s < \tilde{\varepsilon} \\ \beta_{n,0}(E^0_{K}), \text{ else} \end{cases}$
$\alpha_{m,0}(V) = \frac{25-(V-V_{rest})}{10\left(e^{(25-(V-V_{rest}))/10}-1\right)}$ $\alpha_{h,0}(V) = 0.07e^{-(V-V_{rest})/20}$ $\beta_{m,0}(V) = 4e^{-(V-V_{rest})/18}$ $\beta_{h,0}(V) = \frac{1}{e^{(30-(V-V_{rest}))/10}+1}$	$\alpha_{n,0}(V) = \frac{10-(V-V_{rest})}{100\left(e^{(10-(V-V_{rest}))/10}-1\right)}$ $\beta_{n,0}(V) = 0.125e^{-(V-V_{rest})/80}$

By combining Equations (3.12), (3.13) and (3.14), the following can be obtained:

$$\begin{cases} \nabla_{\mathbf{n}} V = -\rho_c \left(\dfrac{C_m C_{my}}{h_m C_{my} + n_{my} h_{my} C_m} \dfrac{\partial V}{\partial t} + \dfrac{1}{h_m \rho_m + n_{my} h_{my} \rho_{my}} (V - V_{rest}) \right), \\ \qquad\qquad \forall \mathbf{x} \in \partial\Omega^{CT} \\ \nabla_{\mathbf{n}} V = \dfrac{-\rho_c}{h_m} \left(C_m \dfrac{\partial V}{\partial t} + G_{Na}(V - E_{Na}) + G_K(V - E_K) + G_L(V - E_L) \right), \\ \qquad\qquad \forall \mathbf{x} \in \partial\Omega^{HH} \end{cases} \tag{3.15}$$

which are subsequently represented by two functions f_{CT} and f_{HH}:

$$\begin{cases} \nabla_{\mathbf{n}} V = f_{CT}(V, \frac{\partial V}{\partial t}, \varepsilon_s), & \forall \mathbf{x} \in \partial\Omega^{CT} \\ \nabla_{\mathbf{n}} V = f_{HH}(V, \frac{\partial V}{\partial t}, \varepsilon_s), & \forall \mathbf{x} \in \partial\Omega^{HH} \end{cases} \tag{3.16}$$

E_L is chosen such that $V = V_{rest}$ at rest [1, 121], i.e.,

$$E_L = \left(1 + \frac{G_{Na}(V_{rest}) + G_K(V_{rest})}{G_L} \right) V_{rest} - \frac{(G_{Na}(V_{rest}) E_{Na} + G_K(V_{rest}) E_K)}{G_L} \tag{3.17}$$

The weak form of the electrophysiological strong form presented in Equation (3.11) then reads: for all admissible virtual potential H,

$$a_{VV}(V, H) = l_V(H) \tag{3.18}$$

where

$$\begin{cases} a_{VV}(V, H) = \iiint_{\Omega} V_{,i} H_{,i} dV \\ l_V(H, V, \mathbf{u}) = \iiint_{\Omega} \frac{\tilde{\rho}}{\epsilon_0} H dV + \iint_{\partial\Omega^{CT}} H f_{CT}(V, \mathbf{u}) dS + \iint_{\partial\Omega^{HH}} H f_{HH}(V, \mathbf{u}) dS \end{cases} \tag{3.19}$$

According to Nanson's formula, $dS\mathbf{n} = J dS_0 \mathbf{F}^{-T} \cdot \mathbf{N}$, where $\mathbf{F} = \frac{\partial \mathbf{x}}{\partial \mathbf{X}}$ is the deformation gradient tensor, Equation (3.19) can be rewritten in the reference configuration:

$$\begin{cases} a_{VV}(V, H) = \iiint_{\Omega_0} V_{,J} F^{-1}_{Ji} H_{,K} F^{-1}_{Ki} J dV_0 \\ l_V(H, V, \mathbf{u}) = \iiint_{\Omega_0} \dfrac{\tilde{\rho}}{\epsilon_0} H J dV_0 + \iint_{\partial\Omega_0^{CT}} H f_{CT}(V, \mathbf{u}) J N_I F^{-1}_{Ii} n_i dS_0 \\ \qquad\qquad + \iint_{\partial\Omega_0^{HH}} H f_{HH}(V, \mathbf{u}) J N_I F^{-1}_{Ii} n_i dS_0 \end{cases} \tag{3.20}$$

where $J = \det(\mathbf{F})$ is the Jacobian and the subscript "0" refers to the reference configuration . Note that here a_{VV} also indirectly depends on $\mathbf{u}$ through $\mathbf{F}$.

The FE formulation for the electrical potential is defined by:

$$\mathbf{F}_V^{ext} = \mathbf{F}_V^{int} \tag{3.21}$$

where the external and internal electrical force vectors $\mathbf{F}_V^{ext}$ and $\mathbf{F}_V^{int}$ are given by:

$$\begin{cases} F_{V,a}^{ext} = l_V(N_a, V_h, \mathbf{u_h}) = \iiint_{\Omega_0} \frac{\tilde{\rho}}{\epsilon_0} N_a J dV_0 \\ \qquad\qquad + \iint_{\partial\Omega_0^{CT}} N_a f_{CT}(V_h, \mathbf{u_h}) J N_I F_{Ii}^{-1} n_i dS_0 \\ \qquad\qquad + \iint_{\partial\Omega_0^{HH}} N_a f_{HH}(V_h, \mathbf{u_h}) J N_I F_{Ii}^{-1} n_i dS_0 \\ F_{V_h,a}^{int} = a_{VV}(V_h, N_a) = \iiint_{\Omega_0} V_{h,J} F_{Ji}^{-1} N_{a,K} F_{Ki}^{-1} J dV_0 \end{cases} \tag{3.22}$$

where the FE potential vector V_h is estimated from the nodal potential vector V_a by use of the shape functions N_a:

$$V_h = \Sigma_a N_a(\mathbf{X}) V_a \tag{3.23}$$

Note that the same second order polynomial shape functions were used for both discretisations.

3.1.3 Coupled problem

The entire coupled FE problem requires solving the following:

$$\mathbf{F}^{ext} = \mathbf{F}^{int} \tag{3.24}$$

where

$$\mathbf{F}^{ext} = \begin{pmatrix} \mathbf{F}_{\mathbf{u}}^{ext} \\ \mathbf{F}_V^{ext} \end{pmatrix}, \mathbf{F}^{int} = \begin{pmatrix} \mathbf{F}_{\mathbf{u}}^{int} \\ \mathbf{F}_V^{int} \end{pmatrix} \tag{3.25}$$

In a non-linear implicit problem, the residual $\mathbf{r} = \mathbf{F}^{int} - \mathbf{F}^{ext}$ is iteratively decreased to zero (or close enough) through the Newton-Raphson method. To this end, the stiffness matrix is defined as the derivative of the residual:

$$\mathbf{K} = \begin{pmatrix} \mathbf{K^{uu}} & \mathbf{K^{uV}} \\ \mathbf{K^{Vu}} & \mathbf{K^{VV}} \end{pmatrix} = \begin{pmatrix} \frac{\partial \mathbf{r_u}}{\partial \mathbf{u}} & \frac{\partial \mathbf{r_u}}{\partial V} \\ \frac{\partial \mathbf{r}_V}{\partial \mathbf{u}} & \frac{\partial \mathbf{r}_V}{\partial V} \end{pmatrix} \tag{3.26}$$

By solving both CT and HH equations using the forward difference scheme (see Appendices A.1 and A.2, note that no intermediary times were used, i.e., α listed in the Appendix is zero), the stiffness matrix terms can be written as:

$$K^{\mathbf{uu}}_{iakb} = \iiint_{\Omega_0} \frac{\partial P_{iJ}}{\partial F_{kL}} N_{a,J} N_{b,L} dV_0 \tag{3.27}$$

$$\mathbf{K}^{\mathbf{u}V} = \mathbf{0} \tag{3.28}$$

$$\begin{aligned} K^{VV}_{ab} = & \iiint_{\Omega_0} N_{b,J} F^{-1}_{Ji} N_{a,K} F^{-1}_{Ki} J dV_0 \\ & + \iint_{\partial\Omega^{CT}_0} N_a \frac{\rho_c C_m C_{my}}{(h_m C_{my} + n_{my} h_{my} C_m)\Delta t} N_b J N_I F^{-1}_{Ii} n_i dS_0 \\ & + \iint_{\partial\Omega^{HH}_0} N_a \frac{\rho_c C_m}{h_m \Delta t} N_b J N_I F^{-1}_{Ii} n_i dS_0 \end{aligned} \tag{3.29}$$

$$\begin{aligned} K^{Vu}_{akb} = \frac{\partial r^V_a}{\partial u_{kb}} = & \iiint_{\Omega_0} V_c N_{c,J} \frac{\partial F^{-1}_{Ji}}{\partial u_{kb}} N_{a,K} F^{-1}_{Ki} J dV_0 \\ & + \iiint_{\Omega_0} V_c N_{c,J} F^{-1}_{Ji} N_{a,K} \frac{\partial F^{-1}_{Ki}}{\partial u_{kb}} J dV_0 \\ & + \iiint_{\Omega_0} V_c N_{c,J} F^{-1}_{Ji} N_{a,K} F^{-1}_{Ki} \frac{\partial J}{\partial u_{kb}} dV_0 \\ & - \iiint_{\Omega_0} \frac{\tilde{\rho}}{\epsilon_0} N_a \frac{\partial J}{\partial u_{kb}} dV_0 \\ & - \iint_{\partial\Omega^{CT}_0} N_a \frac{\partial f_{CT}}{\partial u_{kb}} J N_I F^{-1}_{Ii} n_i dS_0 \\ & - \iint_{\partial\Omega^{CT}_0} N_a f_{CT} N_I \frac{\partial (J F^{-1}_{Ii} n_i)}{\partial u_{kb}} dS_0 \\ & - \iint_{\partial\Omega^{HH}_0} N_a \frac{\partial f_{HH}}{\partial u_{kb}} J N_I F^{-1}_{Ii} n_i dS_0 \\ & - \iint_{\partial\Omega^{HH}_0} N_a f_{HH} N_I \frac{\partial (J F^{-1}_{Ii} n_i)}{\partial u_{kb}} dS_0 \end{aligned} \tag{3.30}$$

where

$$\frac{\partial (J F^{-1}_{Ii} n_i)}{\partial u_{kb}} = J F^{-1}_{Jk} N_{b,J} F^{-1}_{Ii} n_i - J F^{-1}_{Ik} N_{b,K} F^{-1}_{Ki} n_i + J F^{-1}_{Ii} \frac{\partial n_i}{\partial u_{kb}} \tag{3.31}$$

The matrix term governing the electrical to mechanical coupling is not considered in this framework, i.e., Equation (3.28). This is because the theory of a mechanical

wave accompanying an electrical wave is still highly controversial, with some research reporting that mechanical waves were observed to accompany electrical waves [122], others posited that the theory that AP is initiated mechanically rather than electrically [123, 124]. Since it is not established whether the electrical to mechanical coupling has any significance in TBI, only an asymmetric coupling is presented here.

All integrals (both in volume and on surface) are numerically calculated using Gauss quadrature. Note that the terms in $\frac{\partial f_{CT}}{\partial u_{kb}}$ and $\frac{\partial f_{HH}}{\partial u_{kb}}$ were found to be negligible and were therefore ommitted in the implementation, their derivations however are provided along with $\frac{\partial n_i}{\partial u_{kb}}$ in Appendices A.3, A.4 and A.5. The above FE framework was implemented in the open source FE code Gmsh [116, 117].

3.2 Boundary conditions implementation and verification

In order to verify the implementation of the CT and HH boundary conditions, both were simulated and verified separately and, in the absence of deformation, compared to the results of two other numerical schemes: *Neurite*, an explicit 1D finite difference framework for mechanical electrophysiological coupling [1, 121], and a Matlab 1D finite element code with CT and HH applied as boundary conditions in a similar fashion, and solved using the Newton-Raphson iterative scheme (see Appendix A.7).

3.2.1 Implementation

The CT and HH equations implementations were first verified separately using a cylinder (with a diameter of 3 µm and lengths of 100 µm and 600 µm for CT and HH respectively) to represent the axonal geometry. The cylinder was discretised with 16,638 quadratic tetrahedral elements. Dirichlet boundary conditions were applied to both ends of the axon: 0 mV on the left hand side and −65 mV (the resting potential) on the right hand side. CT and HH boundary conditions were applied to the envelope of the cylinder model the axonal membrane.

The electrophysiological parameters are the same as in Ref. [1, 121], except for the membrane resistivity whose value was arbitrarily reduced thousandfold

and the number of myelin layers which was set to zero for the verification of CT simulations. This was to artificially accentuate the non-linear effects of membrane current leak and better confirm the scheme convergence (for later simulations the number of layers was set to 45), see Table 3.2.

	Parameter	Value
V_{rest}	Resting potential	$-65\,\mathrm{mV}$ [2]
ρ_c	Cytoplasm resistivity	$1.89\,\Omega\,\mathrm{m}$ [33]
ρ_m	Membrane resistivity	$2.5 \times 10^6\,\Omega\,\mathrm{m}$ [33]
ρ_{my}	Myelin layer resistivity	$4.44 \times 10^6\,\Omega\,\mathrm{m}$ [125]
C_m	Membrane capacitance	$4 \times 10^{-11}\,\mathrm{F\,m^{-1}}$ [33, 120, 125]
C_{my}	Myelin capacitance	$1.8 \times 10^{-10}\,\mathrm{F\,m^{-1}}$ [125]
h_m	Membrane thickness	$4 \times 10^{-9}\,\mathrm{m}$ [126]
h_{my}	Myelin layer thickness	$1.08 \times 10^{-9}\,\mathrm{m}$ [125]
n_{my}	Number of myelin layers	0 and 45 [127]
$\overline{G}_{Na}$	Na_V Reference conductivity	$4.8 \times 10^{-6}\,\mathrm{S\,m^{-1}}$ [33, 120]
$\overline{G}_K$	K_V Reference conductivity	$1.44 \times 10^{-6}\,\mathrm{S\,m^{-1}}$ [33, 120]
G_L	Leak conductivity	$1.2 \times 10^{-8}\,\mathrm{S\,m^{-1}}$ [33, 120]
E^0_{Na}	Na_V Reference reversal potential	$49.5\,\mathrm{mV}$ [33, 120]
E^0_K	K_V Reference reversal potential	$-77.5\,\mathrm{mV}$ [33, 120]

Table 3.2: Electrophysiological parameter values.

Tables 3.3 and 3.4 summarise the spatial and time discretisation parameters used in all three programs. Spatial and temporal convergences were verified for all three cases.

	Neurite	1D FE	3D FE
Number of elements	2000	80	134 (along x)
Element length (m)	5×10^{-8}	125×10^{-8}	75×10^{-8}
Time step size (s)	2.5×10^{-11}	1×10^{-6}	5×10^{-6}
Relative NR tolerance	N/A	1×10^{-8}	1×10^{-8}

Table 3.3: CT simulation parameters.

	Neurite	1D FE	3D FE
Number of elements	500	80	800 (along x)
Element length(m)	120×10^{-8}	125×10^{-8}	75×10^{-8}
Time step size(s)	1.8×10^{-8}	1×10^{-8}	1×10^{-5}
Relative NR tolerance	N/A	1×10^{-8}	1×10^{-8}

Table 3.4: HH simulation parameters.

3.2.2 Verification

The resulting steady-state voltage field in the absence of mechanical deformation (taken here at 50 µs) as predicted by the 3D FE model with CT boundary conditions is presented in Figure 3.2a. A plot showing the voltage profiles along the axon computed by all three schemes is presented in Figure 3.2b, where the 3D FE profile plot was generated by extracting the values of the centre-line FE nodes of the 3D cylinder geometry. The effect of leakage in the CT equation was associated with the system's state-space constant: the ratio of transverse to axial resistivities [33].

A longer geometry and simulation time was necessary for HH simulations in order to observe the dynamics of the gating channels in the HH equations. The transient voltage field in the absence of mechanical deformation at 1 ms predicted by the 3D FE model with HH boundary conditions is shown in Figure 3.3a. The comparison plot of the voltage profiles along the axon for is presented for all three schemes in Figure 3.3b.

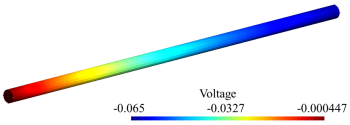

(a) Voltage profiles along the axon from 3D FE simulations

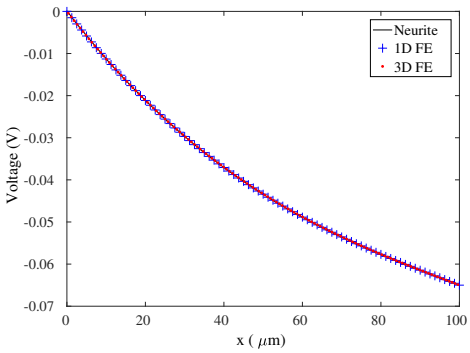

(b) A comparison plot of simulations from all three methods

Figure 3.2: 3D FE internode simulation and comparison plot of propagation profiles along the axon between *Neurite*, 1D FE and 3D FE with CT boundary conditions.

A conservative element size was used here for the *Neurite* simulation, as an explicit scheme was used to generate the results. The time step of *Neurite* was also orders of magnitude smaller, however this was automatically determined by *Neurite* according to the element size and the scheme stability [121]. The 1D FE simulation required the smallest number of elements for spatial convergence,

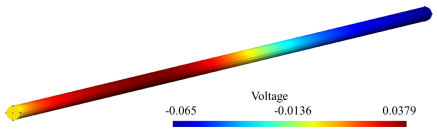

(a) Voltage profiles along the axon from 3D FE simulations

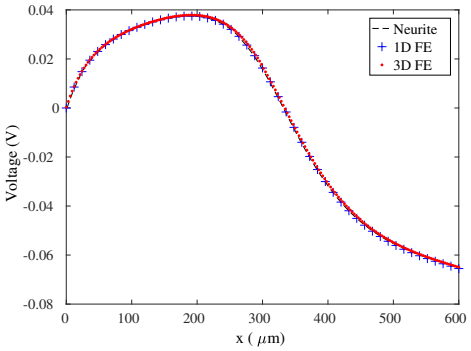

(b) A comparison plot of simulations from all three methods

Figure 3.3: 3D FE node of Ravier simulation and comparison plot of propagation profiles along the axon between *Neurite*, 1D FE and 3D FE with HH boundary conditions at 1 ms.

and a relatively large time step for temporal convergence. All simulations were temporally and spatially converged. For the *Neurite* simulations, a critical time step was determined by a spectral analysis method within the platform, please refer to Jerusalem et al. [1] for more details. A manual convergence study was performed on the 1D FE simulations. As no explicit convergence study was performed on the 3D FE simulations, the time steps and element sizes were chosen based on the 1D FE study and the results were compared across the three platforms to ensure that the results converged.

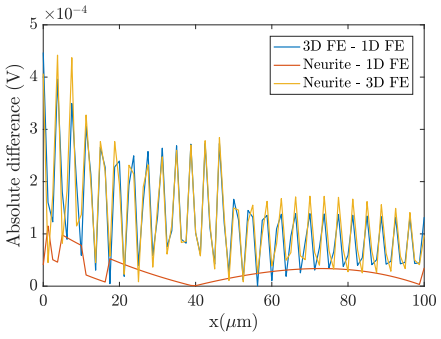

(a) Absolute difference between the three platforms for CT simulations

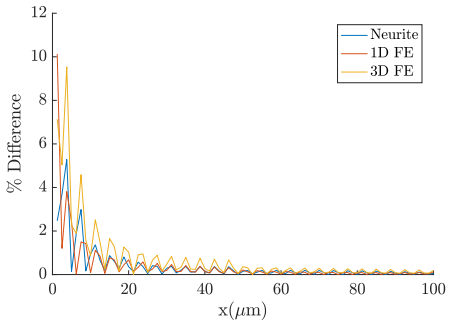

(b) Percentage difference of each platform compare to the mean of the other two platforms for CT simulations

Figure 3.4: Difference comparison plot of propagation profiles along the axon between *Neurite*, 1D FE and 3D FE with CT boundary conditions.

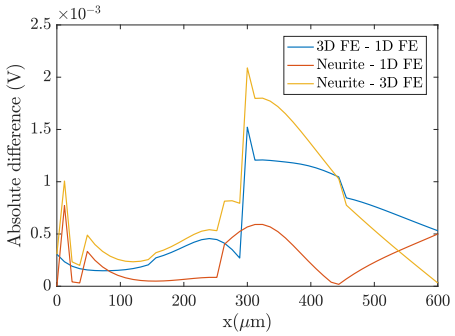

(a) Absolute difference between the three platforms for HH simulations

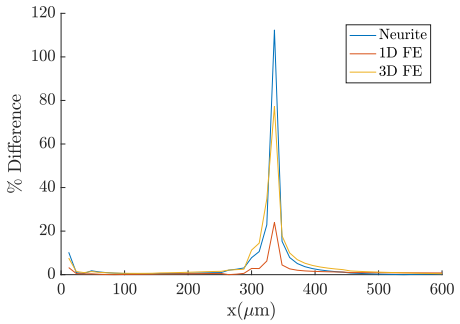

(b) Percentage difference of each platform compare to the mean of the other two platforms for HH simulations

Figure 3.5: Difference comparison plot of propagation profiles along the axon between *Neurite*, 1D FE and 3D FE with HH boundary conditions at 1 ms.

Figures 3.4a and 3.5a plot the absolute difference between the two platforms for CT and HH simulations respectively. Figures 3.4b and 3.5b plot the percentage difference of each platform compared to the mean of the other two platforms for CT and HH respectively. As seen in Figure 3.4a and 3.5a, the absolute differences between *Neurite* and 1D FE (red line) are generally lower compared to the differences between *Neurite* and 3D FE (blue line), and 3D FE and 1D FE (yellow line) for both CT and HH simulations. The absolute error stayed below 5×10^{-4} for CT simulations and 2.5×10^{-3} for HH simulations. The percentage difference compared to the other platforms are low except for when the simulation values are near zero, as expected. The error between the three platforms are significantly small for the purpose of verifying the implementation of the proposed scheme on a 3D FE platform. Further comparisons across platforms will take into account the differences that this study has shown.

3.3 Axonal indentation

This section demonstrates the capability of the framework by modelling the AP propagation alteration in a theoretical simulation of an axon within a dislocated spinal cord. Dislocation is when the spinal cord is indented or laterally displaced, e.g., by the shearing movement of one vertebra, or fragmentation of bones. Such

dislocation leads to a state of loading mixing simultaneously tension and compression. This type of loading was chosen because it contains mixed loading modes and also because several cell and tissue scale experiments have used indentation-like setups to approximate axon stretch and mild TBI [52, 71, 112]. To explore different possible conduction phenomenon, three different scenarios are considered and simulated:

1. **No change.** The model described above is used as such with $E_{Na} = E_{Na}^0$ and $E_K = E_K^0$, i.e., no damage is considered. In this case, as the area of the membrane is changing during deformation, the electrophysiological properties vary accordingly, i.e., the integrals in Equation (3.19) are done with respect to the deformed configuration. This model is in agreement with the idea that growing axons retain their electrophysiological properties per unit membrane area [128].

2. **Number of ion channels is conserved**. No irreversible damage is considered ($E_{Na} = E_{Na}^0$ and $E_K = E_K^0$) but the ion channel activity reflects the fact that even stretched, the number of ion channels remains the same. The half-life of an ion channel would be in the magnitude of hours to days. Therefore when modelling the immediate effects post mechanical loading the conservation of ion channels can be posited [129], i.e., the integrals related to the ion channels activity in Equations (3.19) need to be done with respect to the original configuration, see Equation (3.32).

3. **Number of ion channels is conserved and they can be damaged**. This model follows the approach proposed by Jérusalem et al. [1] to model the ion channel "left-shift" related damage. In this model, Equation (3.32) is also used but the reversal potentials of the ion channels are modified to reflect such damage, see Equation (3.33).

$$\begin{cases} a_{VV}(V,H) = \iiint\limits_{\Omega} V_{,i} H_{,i} dV \\ l_V(H,V,\mathbf{u}) = \iiint\limits_{\Omega} \frac{\tilde{\rho}}{\epsilon_0} H dV + \iint\limits_{\partial\Omega^{CT}} H f_{CT}(V,\mathbf{u}) dS \\ \qquad\qquad + \iint\limits_{\partial\Omega^{HH}} \frac{-\rho_c}{h_m} \left(C_m \frac{\partial V}{\partial t} + G_L(V - E_L) \right) dS \\ \qquad\qquad + \iint\limits_{\partial\Omega_0^{HH}} \frac{-\rho_c}{h_m} \left(G_{Na}(V - E_{Na}) + G_K(V - E_K) \right) dS_0 \end{cases} \tag{3.32}$$

$$\begin{cases} E_{Na} & = \alpha E_{Na}^0 \\ E_K & = \alpha E_K^0 \end{cases} \text{ where } \alpha = \begin{cases} 1 - \left(\frac{\varepsilon_s}{\tilde{\varepsilon}}\right)^{\gamma}, & \text{if } \varepsilon_s < \tilde{\varepsilon} \\ 0, & \text{else.} \end{cases} \tag{3.33}$$

where $\tilde{\varepsilon} = 0.1$ is are the corresponding threshold at which the membrane is considered fully damaged and $\gamma = 2$ is an exponent representing the sensitivity of the damage model to small *vs.* large deformation [1].

3.3.1 Simulation setup

Two cylinders with a diameter of 3 µm were used to approximate axons with two nodes of Ranvier and internodes. The first node of Ranvier is 2 µm long, the second node of Ranvier is 10 µm long, and both internodes are 600 µm long. A downward pressure of 500 Pa was applied to the upper parts of the nodal and internodal regions over 0.05 µs, see Figure 3.6. The ends of the axons were mechanically fixed in the horizontal direction, and the longitudinal lines running at the base of the axons were fixed vertically except for the segment being indented. In terms of electrical boundary conditions, the right face was clamped at −65 mV while a ramp from −65 mV to 0 mV was applied to the left face over 0.1 ms after the mechanical loading step (from 0.05 to 0.15 ms) and sustained for an additional 9.85 ms. The total simulation time is 10 ms. The measure point for AP propagation in both cases was at 725 µm.

An explicit scheme was used for solving the electrophysiological ion channel dynamics variables m, n and h of the HH boundary condition equations. The simulation time step was chosen based on the convergence of the electrophysiological equations, since the electrophysiology was evaluated on the final deformed geometry. A linear elastic material law was taken for the axon mechanical behaviour as a

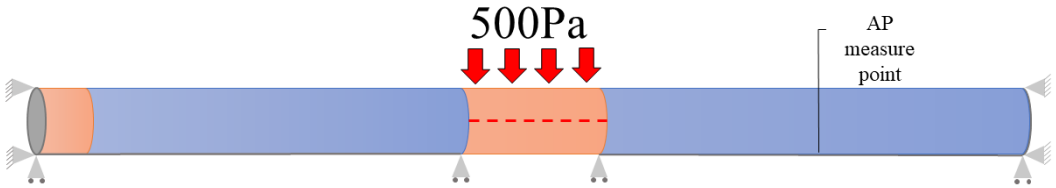

(a)

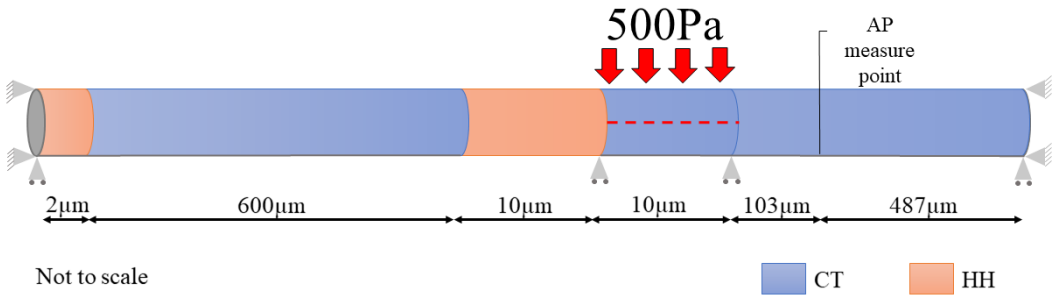

(b)

Figure 3.6: Axon geometry and boundary condition schematic with mechanical loading at a) the node of Ranvier, b) the internode.

first approximation and a linear static implicit scheme was used for the mechanics solver. As the aim of this chapter is to provide the overall framework of the coupled approach and as the electrophysiological model only depends on the geometrical deformation in its current form, the material law is only used here as a means for mechanical deformation. Note that future implementations where material irreversible deformation (e.g., plasticity) can directly be fed into the electrophysiological models are straightforward. The mechanical material properties are listed in Table 3.5. The electrophysiological parameter values used here were the same as the ones listed previously in Table 3.2, except for the number of myelin layers which was increased to 45 [1].

This study focusses on the electrophysiological change due to membrane deformation. The mechanical boundary conditions were simplified to treat the region peripheral to the membrane as a homogenous entity. This is adequate for demonstrating the electrophysiological alteration due to the fact that the AP is governed by the HH model. It is however important to note that the mechanical

stiffness of myelin are much higher than that of the membrane and would in reality influence the deformation under mechanical load.

	Parameter	Value
E	Young's modulus	165.920 kPa
ρ	Material density	993 kg m^{-3}
ν	Poisson's ratio	0.3

Table 3.5: Mechanical material properties for axon cytoplasm.

3.3.2 Results and discussion

Figure 3.7 shows the indentation of the nodal region with a close-up of the site of indentation. Both nodal and internodal indentations result in a maximal displacement of 2.84 µm at the centre of the segment as the same mechanical properties were chosen for both regions. The post-deformation electrical potential *vs.* time profiles of the centre-line node of the 3D geometry at the measure point are shown in Figure 3.8: the AP propagation of an axon without mechanical deformation (green line), with internodal indentation (dashed blue line), with nodal indentation (dashed red line) with nodal indentation and conserved number of ion channels (dotted red line), with nodal indentation and conserved number of damageable ion channels (solid red line).

The indentations applied in this study may not be experimentally realistic, however the above simulations can sufficiently demonstrate that this is a flexible framework for modelling 3D mechanical-electrophysiological coupled problems. Note that the initial rise in potential (up to −40 mV) seen in all cases is an artifact of the imposed constant voltage loading used to trigger the AP. The resting potentials of the cases without the damage model are also not fully recovered for the same reason. For the case where the channels' damage model is implemented, the resting potential is affected by the modification of the reversal potentials through the membrane surface strain, see Equation (3.33).

The AP from the internodal indentation case and the nodal indentation case with conserved number of ion channels (proportional to the original area) are very similar to the reference case (no deformation), the default case of nodal indentation

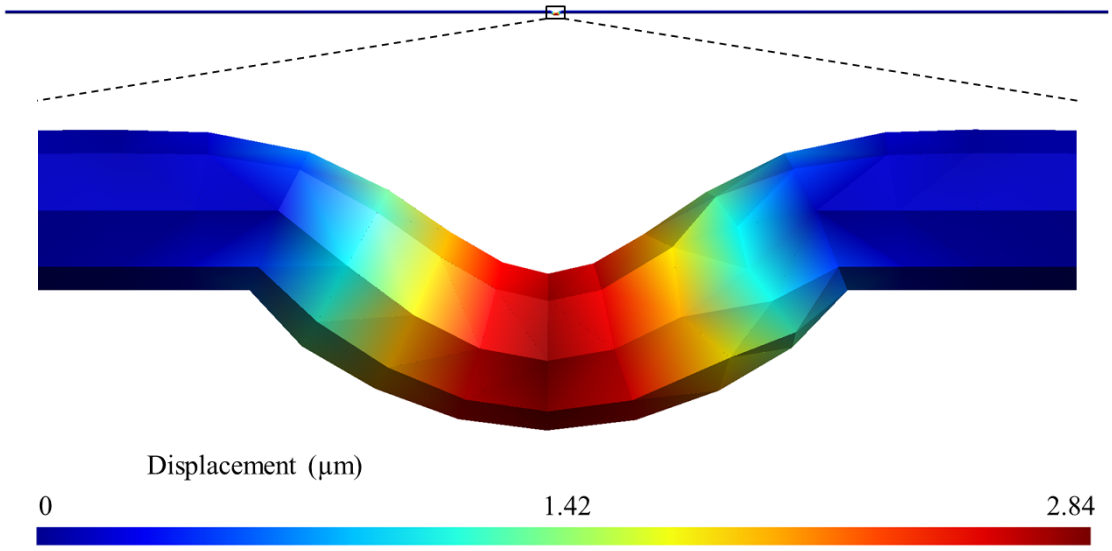

Figure 3.7: Resultant deformation of 500 Pa applied on 10 µm of axon.

(the ion channel number is proportional to the deformed area) sees a noticeable increase in peak amplitude. This is due to an increase in active surface area of the deformed node of Ranvier where HH boundary conditions are applied. For the case of internodal indentation, since the enlarged region is a passive membrane, no remarkable activity change was expected.

In the experimental work by Greer et al. [58], an increase of AP amplitude and a shorter after-hyperpolarisation duration was reported in intact and axotomised (characterised by axonal swelling) pyramidal axons, one and two days after mild TBI induced by a brief fluid pressure pulse. The authors suggested that these observations may be the result of an increase in the number of Na^+ channels combined with several different underlying K^+ channels changes, deeming damaged axons more excitable. These results are in agreement with our model predictions, where long term membrane re-organisation could ensure a recovery of the density of ion channels, and thus increase the membrane activity accordingly to its increase of surface area. Contrary to previous modelling efforts [1, 2, 107], no damage consideration was needed here to alter the electrical signal. The above simulations compare more similarly to the finite difference model of Tekieh et al. [104], where

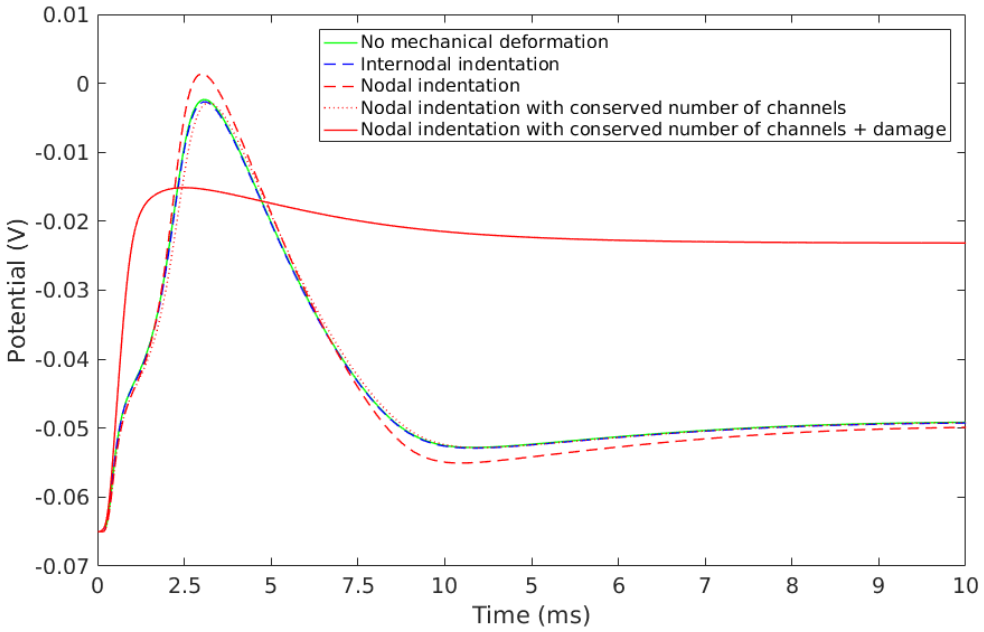

Figure 3.8: AP propagation comparison between axon without indentation, indentation of internodal segment and nodal segment are presented as a green blue and lines, respectively, with the three model modifications for the nodal indentation.

the altered electrophysiology is a direct result of the deformation itself. However, in the study by Tekieh et al. [104], a decreased AP amplitude was reported as the nodal geometry becomes depressed. This differs from the results presented here because in an axisymmetric finite difference model, a depressed nodal region corresponds to a smaller circumferential membrane area, and therefore resulting in a lower conductance (hence a decreased AP amplitude). Such discrepancy highlights the need for 3D models when modelling axonal damage.

Based on the theory of coupled "left-shift" in Na_V channels (channel type 1.6) reported by Wang et al. [24], Jérusalem et al. [1] proposed a damage model for Na_V and K_V channels. This model was implemented and presented as the red solid line in Figure 3.8. The AP amplitude is significantly decreased by the damage model compared to the other cases. Note that the critical strain for the damage model used here is 0.1, which is the same as the value reported by Jérusalem et al. [1]. This value was calibrated with tissue scale data, and hence may not be applicable for a model on cellular scale. The aim of this particular result however is to demonstrate

the flexibility of this framework to explore different damage mechanisms.

3.3.3 Comparison of coupled "left-shift" theory between 1D and 3D models

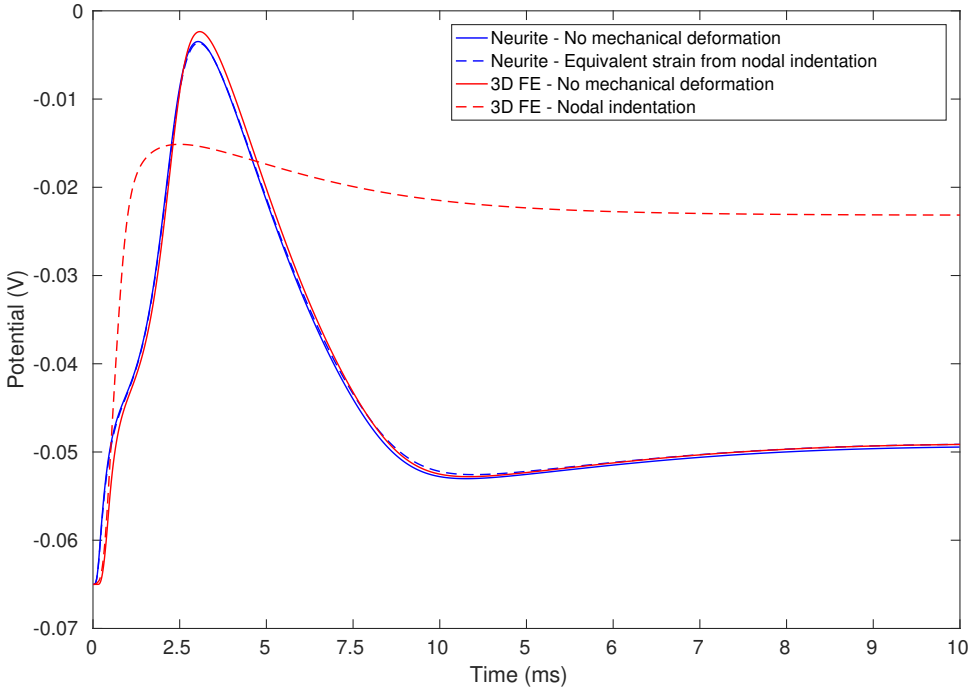

Figure 3.9: AP propagation comparison between 3D FE and *Neurite* simulations.

To further demonstrate the difference between 1D and 3D models when modelling coupling, an equivalent case of axon indentation was modelled in 1D with *Neurite*, presented in Figure 3.9 as a blue dashed line (solid line is without deformation). The axon indentation in 1D was modelled by applying an axial strain of 0.179 (approximated from the centre line of 3D deformation from the 3D FE simulations shown in Figure 3.7) to the corresponding node of a *Neurite* axon simulation. The APs for the 3D FE cases with no mechanical deformation and nodal indentation with conserved damageable ion channel number (i.e., the same underlying model as in *Neurite*) are shown as red lines in Figure 3.9.

There is an insignificant difference between the non-indented and the indented axon modelled in 1D, as the indentation equivalent axial stretch is insufficient to

cause any alteration in electrophysiology, while the amount of damage present in the 3D formulation is more significant than in the 1D case. This is due to the ability of the 3D formulation to capture the local gradient of deformation in a small region, enough to affect the overall electrophysiology. Indeed, while a mean increase in length is equally observed, the 3D model is additionally able to capture non-axisymmetric large tensile strain in the membrane. Overall this idealised axonal dislocation case demonstrates the ability of the proposed framework to capture electrophysiological alterations associated to localised damage.

Note that there are differences in conduction in APs between a *Neurite* and a 3D FE simulation when comparing the AP with no mechanical damage (Figure 3.7, solid blue and red line respectively). The AP of an undeformed axon from the 3D FE simulation produced a slightly slower but higher amplitude AP. These differences are down to differences in formulation since the 1D model is a finite difference formulation, while the 3D model is a FE formulation and hence yielding a slightly different approximation of the ion channel dynamics in the HH equation.

It is also important to note that the incompressibility assumption was used in the *Neurite* simulation, while a Poisson's ratio of 0.3 was assumed for the 3D FE. For a large enough lateral deformation this could have a significant effect on the magnitude of the AP observed, however since the deformations modelled here are relatively small and localised, it was assumed that the difference in compressibility has negligible effects.

In general, the 3D FE model is particularly useful for studying local deformation events compared to the 1D model. Furthermore it is able to take into account complex mechanical boundary conditions that are relevant for TBIs and SCIs. The next chapter will use this 3D FE tool to study local deformation in patch clamping.

4

Subcellular Modelling of Axons

Contents

4.1 Geometry **54**
4.2 Boundary conditions **55**
4.3 Results **56**
4.4 Discussion **57**

Patch clamps are often used to measure cellular electrophysiology, an experimental technique where a pipette is set up with a stimulating electrode inside it, and it is attached to the cell to probe their electrophysiology in various configurations. In this chapter, the voltage clamp in cell-attached configuration is considered. The typical set-up involves attaching the pipette to the membrane of the cell, and after suction of the membrane applied by the pipette, a "gigaseal" is formed without rupturing the membrane. The pipette then has access to the electrophysiology of a small number of ion channels within the patch (as oppose to the electrophysiology of the cell if the membrane is ruptured). A voltage clamp requires the system to maintain the voltage external to the cell (within the pipette solution) to a fixed potential. This is done by the generation of a compensating current imposed that resembles the ionic changes within the pipette solution. A schematic picture of a typical patch clamp set up is presented in Figure 4.1.

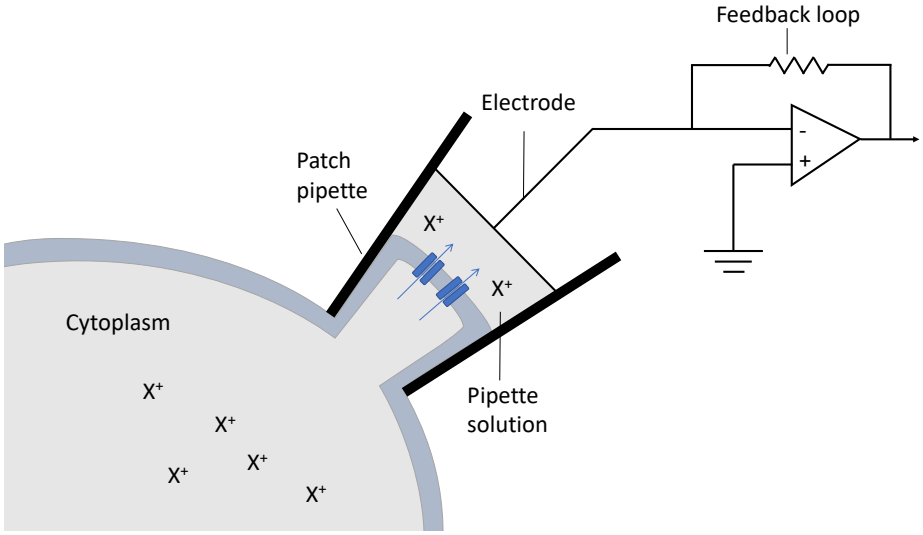

Figure 4.1: Schematic of membrane patch under voltage clamp in cell-attached configuration.

Voltage clamp was used by Hodgkin and Huxley to measure the ion channels dynamics of a giant squid axon, where the electrode inside the pipette was used to stabilise the membrane potential at a fixed voltage (via a feedback loop), while simultaneously recording the current that flows across the membrane in response to a stimulus [33].

The surface tension of the lipid bilayer of a liposome patch has been thoroughly characterised previously, through applying different aspirating pressure and using fluorimetry data to observe membrane geometry [130]. Through such experimental and computational modelling efforts, a descriptive mechanical continuum model was characterised for lipid bilayer in a patch clamp. A further study on membrane curvature was conducted to build understanding of local bending stress variation within the pipette.

Although the geometry and the mechanics of a bleb during patch clamp has not been thoroughly studied. In particular whether the alteration of the membrane geometry alone can lead to electrophysiological alteration or not is unknown [131].

Cell attached voltage clamp was the experimental set up used by Wang et al. to probe the channel dynamics of $Na_V1.6$ that were transfected in HEK cells post-membrane trauma [24]. When using the cell-attached mode for measurement,

a suction is applied to the membrane in order to form a "gigaseal" to obtain electrophysiological measurements [132]. In the aforementioned work, electrophysiological measurements were performed on "pre-stretched" patches, where gigaseals were achieved at pressures between -4 to -7 mmHg (a relatively low pressure for gigaseal formation). Then subsequent higher pressures applied to the patch were reported to cause faster rise times in the $Na_V1.6$ channel dynamics, a "left-shift" [24]. Figure 4.2 shows an example of the "left-shift" dynamics when a suction of 20 mmHg was applied to the membrane.

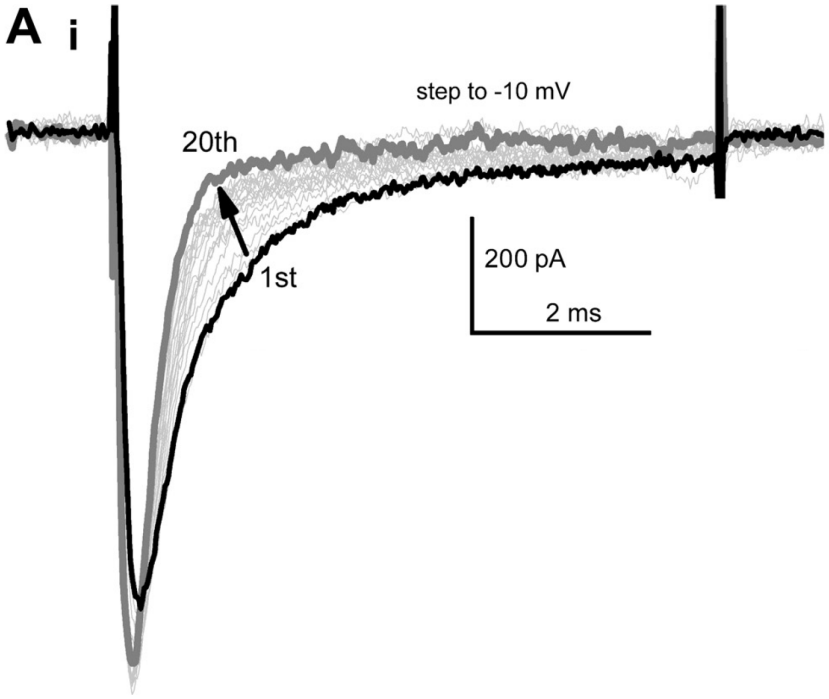

Figure 4.2: "Left-shifted" electrophysiological dynamics observed by Wang et al. [24]. Currents were monitored at 1Hz over a stretch duration of 20s. Black line represents current monitored before stretch and bold grey line represents current after 20s of stretch. Permission to reproduce this image has been granted by Prof. C. E. Morris.

Wang et al. hypothesised that direct membrane stretch through pipette suction causes $Na_V1.6$ channels to become "leaky", suggesting that the channels are susceptible to trauma. In other experimental studies, membranes were shown to behave like fluid under applied pressures and were shown to have interesting electrophysiological properties under mechanical pressure. For example an oocyte's

diameter was shown to nearly double by direct inflation with no measurable change in capacitance [133]. Suchyna et al. observed membrane creep resulting in increased dome height under patch clamping at different pressures [134]. The above shows that pressure has a large effect on bleb geometry and it is possible that the change of geometry itself may have an effect on electrophysiological propagation as opposed to ion channel dynamics alteration. To investigate the effect of pressure induced membrane bleb geometry on electrophysiology, the framework presented in Chapter 3 Section 3.1 was used to simulate the biophysics of the patch clamping.

4.1 Geometry

The geometry of the cell in the pipette is represented by a frustum of a conical cone with radii approximated from microscopy images: (the upper and lower radii are 0.75 and 0.5 µm) [134]. A cube is used to represent the cytoplasm outside the pipette. The resultant geometry can be seen in Figure 4.3. Finally the volume is discretised with 4563 quadratic tetrahedral elements.

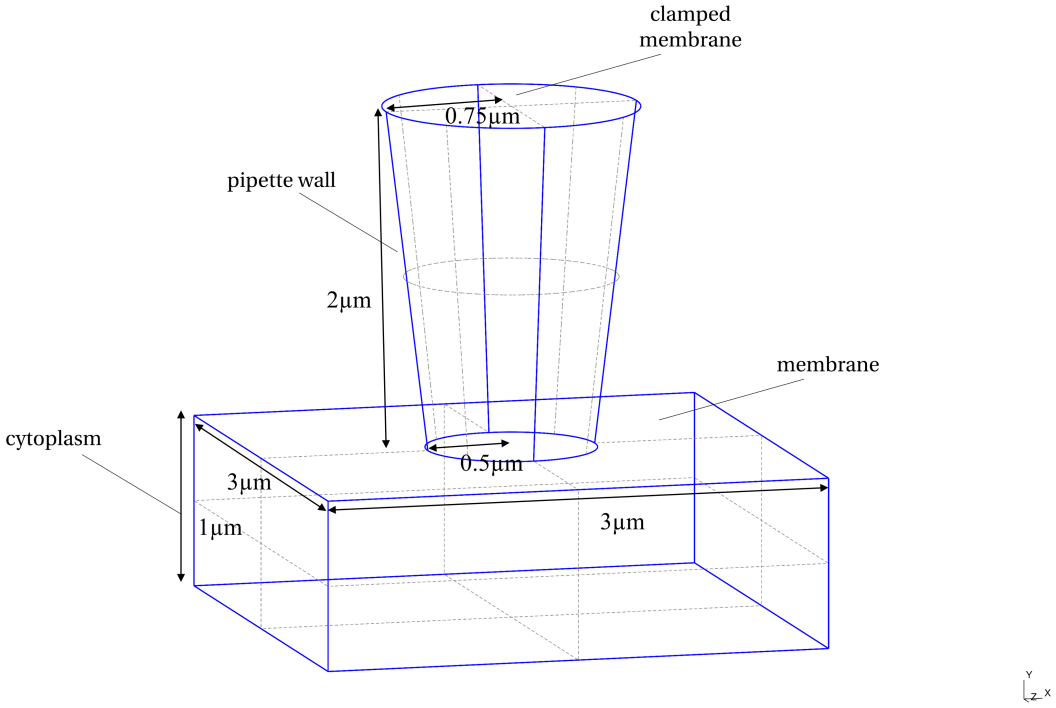

Figure 4.3: Geometry of cell under patch clamp.

4.2 Boundary conditions

A pressure boundary condition is applied to the top face of the bleb FE model to mimic the suction applied by the pipette, while the rest of the geometry was fixed in displacement, including the region representing membrane in contact with the pipette wall (see Figure 4.4). As a reminder, the membrane is "pre-stretched" by light suction to create the gigaseal as in Wang et al. [24], i.e., Figure 4.4 represents the reference configuration. The electrophysiological stimulus is modelled by modifying the reversal potential and the leak potential with a step change in potential (δV=20 mV) to reflect the stimulus applied via the pipette to the top face. This is represented in the circuit diagram in Figure 4.5.

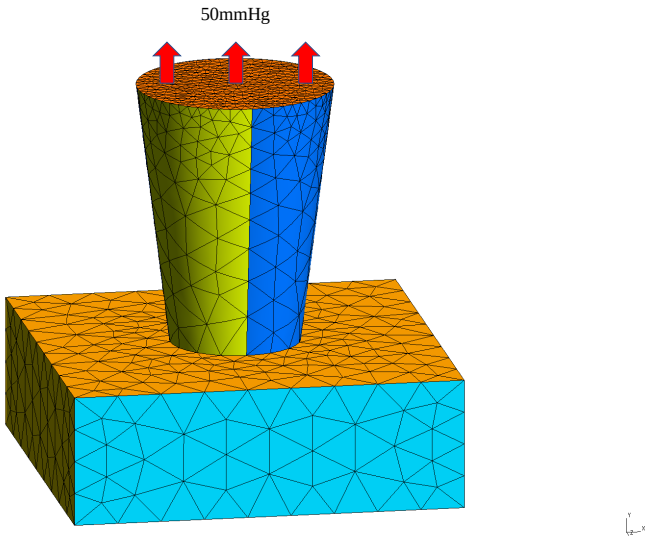

Figure 4.4: Boundary conditions of cell under patch clamp.

With a potential stimulus of δV added to the extracellular environment in the pipette, the HH equation on the clamped membrane then becomes:

$$i_n = c_m \frac{\partial V}{\partial t} + g_{Na}(V - E_{Na} + \delta V) + g_K(V - E_K + \delta V) + g_L(V - E_L + \delta V) \tag{4.1}$$

Note that the initial value of V is that of V_{rest}, which is -65 mV.

Different configuration were applied to the top and the bottom membranes to mimic the effect of electrical stimulation delivered to the top membrane by the pipette. The above modified HH equation was applied to the clamped membrane

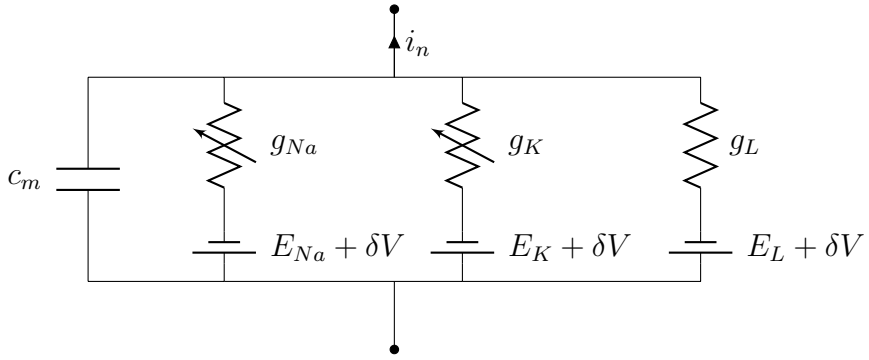

Figure 4.5: Equivalent circuit for voltage clamp stimulation.

in the original configuration (see Chapter 3 Section 3.3 ((3.32)), while the original HH boundary condition was applied to membrane outside the patch clamp (i.e., top of the cube). The domain representing the membrane in contact with the pipette was set to have no electrical flux flowing across it, while the cytoplasm boundaries were set to be free.

4.3 Results

The following figure shows the membrane under a suction equivalent to 50 mmHg. The domain height is approximately 0.3 µm, see Figure 4.6.

To compare the simulation against the current measurements by the electrode within the pipette, the total current flowing in the outward normal direction to the membrane bleb geometry is estimated. This is done by summing the normal currents (i_n) from each element within the clamped membrane region:

$$i_{clamp} = \sum_{n=1}^{N} i_n \tag{4.2}$$

where N is the number of elements within the clamped membrane. The current flow across a patch of membrane without suction (dome height of zero) and a patch of membrane with a suction of 50 mmHg are compared in Figure 4.7. The simulated current flow across patches of membrane experiencing different levels of negative pressure (-40 mmHg, -50 mmHg and -60 mmHg) is presented in Figure 4.8. From both figures, faster channel dynamics, i.e., faster rise time in the current profile similar to the aforementioned "left-shift" dynamics, is observed as negative pressure

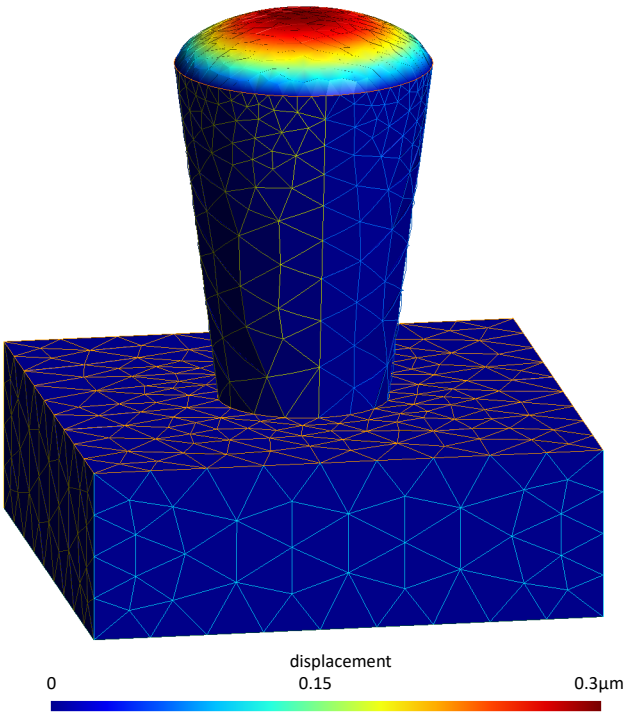

Figure 4.6: Displacement of bleb at maximal suction of 50 mmHg. The displacement shown is at 1:1 scale.

on the patched membrane increases. The magnitude of the normal current also increases with negative pressure applied on the patched membrane.

Figures 4.9a and 4.9b show the intracellular voltage gradient in the original configuration pre and post suction at t=2.14 ms. It can be observed that the voltage gradient at the base of the micropipette pre suction (Figure 4.9a) is greater than post suction (Figure 4.9b). Prior to suction, current is more likely to flow out of the pipette, meaning that less current will be flowing through the top of the membrane and hence will be more likely to lead to a slower dynamics compared to post suction.

4.4 Discussion

In the above simulations, it was assumed that the radius of the cell in which the pipette aspirated from was much larger than the radius of the pipette. Where a typical diameter of a HEK cell is 75 µm [135], and the pipette radius was 0.75 µm. According to the Law of Laplace, the micropipette aspiration can be analysed

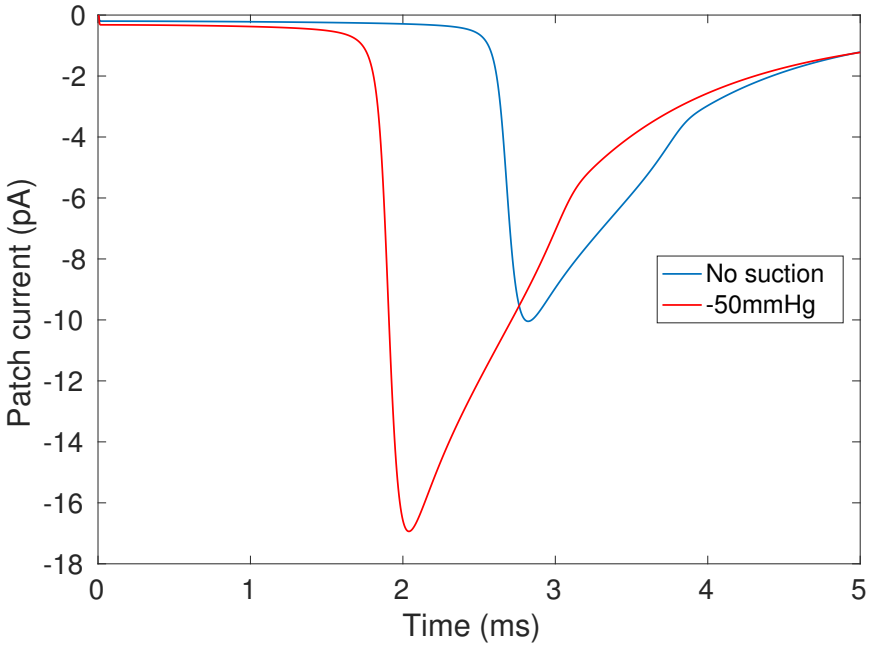

Figure 4.7: Comparison of current flowing normal to membrane with and without suction.

as follows: [136],

$$P_c = \frac{2T_c}{R_c} \tag{4.3}$$

and

$$P_p = 2T_c \left(\frac{1}{R_p} - \frac{1}{R_c} \right) \tag{4.4}$$

where T_c is the membrane surface tension, R_c and R_p are the radii of the cell and pipette respectively, and P_c and P_p are the internal pressure of the cell and pipette respectively. Since R_c is 100 times larger than R_p, assuming a constant membrane tension, P_p will be significantly larger (99 times) than P_c, irrespective of P_c.

Assuming that the aspirated cell region is a hemisphere, $R_c = 75\,\mu\text{m}$ and $R_p = 0.75\,\mu\text{m}$, using 50 mmHg (6666 Pa) pipette aspiration the membrane tension is:

$$T_c = \frac{P_p}{2\left(\frac{1}{R_p} - \frac{1}{R_c}\right)} \tag{4.5}$$

The membrane tension is estimated to be $2.5\,\text{mN}\,\text{m}^{-1}$, which is within the range of membrane tension for mechano-activation of channels ($1\,\text{mN}\,\text{m}^{-1}$) and membrane lytic tension of 5-8 $\text{mN}\,\text{m}^{-1}$.

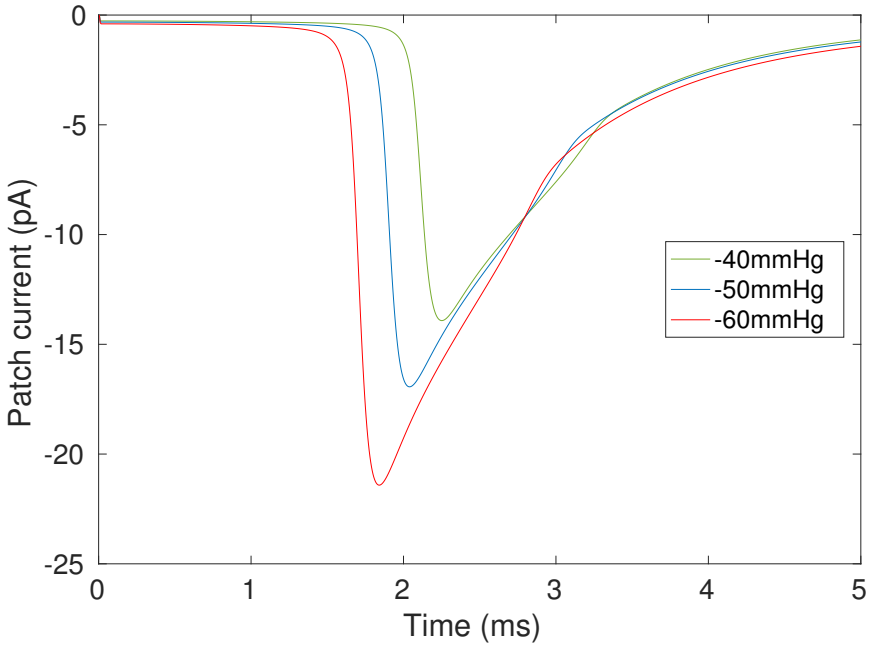

Figure 4.8: Profile of current flowing normal to membrane.

As seen in Figures 4.7 and 4.8, the rise velocity and magnitude of the current flow across the membrane increase as the negative pressure on the patched membrane increases. In the above simulations the membrane geometry during AP propagation was assumed to be fixed. Membrane creep during patch clamp experiments has been previously observed [134], however the time scale of the creep was more than an order of magnitude larger than the time scale of an AP. Furthermore, this study focusses on the electrophysiology propagation on different static geometry as a result of different negative pressure, therefore a fixed geometry was adequate as a first approximation.

In the above simulations the modified HH model with a stimulus of ∂V was applied on the original configuration, where the Na_V and K_V channel conductances were calculated with respect to the original configuration. The leak and membrane capacitance were calculated with respect to the deformed reference frame. The areal strain as a result of different aspirations can be determined by calculating the area of the spherical cap, based on the height of the bleb:

$$A = \pi(a^2 + h^2) \tag{4.6}$$

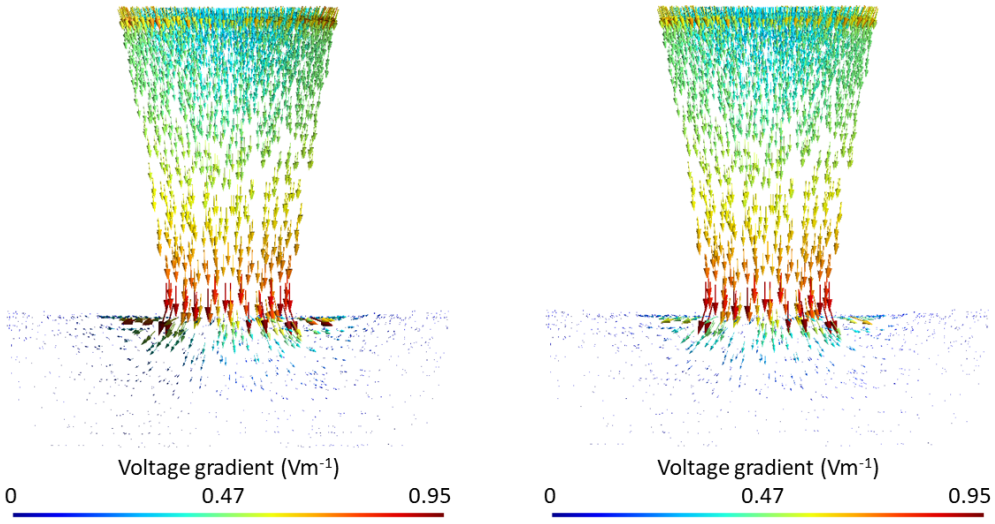

(a) Pre suction **(b)** Post suction

Figure 4.9: Comparison of voltage gradient pre and post suction (50 mmHg) in the original configuration at t=2.14 ms. The difference is most visible in the region at the base of the pipette, slightly higher voltage gradient can be observed in this region pre suction.

where A is the curved surface area of the spherical cap, h is the height of the cap and a ($a = R_p$) is the radius of the base of the cap:

$$A_0 = \pi R_p^2 \tag{4.7}$$

$$A = \pi(R_p^2 + h^2) \tag{4.8}$$

$$\varepsilon_A = \frac{A - A_0}{A_0} \tag{4.9}$$

The height of the bleb, $h = 0.3\,\mu m$. The surface area strain, ε_A is therefore 0.16. As the area of the membrane increased under negative pressure, a higher overall conductance across the membrane, and a faster rise time for channel activation are expected. Furthermore, the overall conductance of the cytoplasm increased as the overall volume increased, this meant that available current from out of the pipette could flow into the clamped region more readily.

It was noted that the magnitude of current from the above simulations was of an order of magnitude smaller than the ones reported in the experiments. A

possible reason may be the number of ion channels that were available in the experimental membrane patches. Since the ion channels were artificially transfected in the experiments, it was possible that there were an abnormally high number of ion channels available to pass ions through the membrane, leading to a higher current. In the above simulations a reference channel concentration from squid axon [33] was selected, if however the ion channel density in the transfected HEK cells was reported, this model can be straightforwardly calibrated to improve the accuracy of the simulation.

It is worth mentioning that in the study of Wang et al. [24], experiments were conducted on cells with $Na_V1.6$ channels with and without beta subunits (a mechanosensitive subunit of the $Na_V1.6$ channel), however no marked difference was reported between the two. The above simulations have demonstrated that geometrical alterations can alter the electrophysiological conduction in terms of an increased rise time of channel activation, without explicitly altering the channel gating dynamics. This is in contradiction with Wang et al.'s conclusion, suggesting that the "left-shift" dynamics cannot be justified by an increase in channel openning probability or area, as this would solely result in an increase in current amplitude [24]. Wang et al. therefore suggested that the data points to trauma-induced $Na_V1.6$ channel dynamics changes. We demonstrated here that this is not necessarily true and that the "left-shift" can be observed without inducing ion channel damage.

Expression levels of Na_V channels in transfected HEK cells are difficult to control. Current densities of transfected HEK cells have been observed to be up to tenfold greater than endogenous current densitiesRe M.T. comment on HEK cells transfection [137]. Expression levels are highly variable and are often too high [138]. Trapani et al. have devised an inducible expression system to control the current density of the transfected cells [138], through such a system, it is then possible to calibrate the channel density to produce a comparable current in future simulations.

5
Axon to nerve scaling

Contents

5.1 Experimental study 64
5.2 Axonal bundle model 65
5.3 Calibration of axonal fibre model 71
5.4 Calibration of representative axon model 74
5.5 Discussion 76

In normal AP propagation, the dynamics of ions flowing in and out of the membrane is governed by the gating variables, modelled by the variables m, n and h in the HH model. The altered axonal electrophysiology caused by mechanical stretch has previously been modelled by Jerusalem et al. [1]. In their study, the axonal model was compared to experimental data measured from guinea pig spinal cord white matter segments. It is however unclear whether the overall CAP of a segment of spinal cord tissue post-stretch (as measured experimentally by Shi et al. [52]) can be modelled by the AP of one unique axon (such as the model by Jerusalem et al. [1]). Additionally, it is also unclear whether an imbalance observed at the axonal levelcan be upscaled to the tissue level. This chapter therefore sets out to explore the modelling of altered macroscopic electrophysiology of a bundle of axons.

The experimental data of this chapter is based on the macroscopic electrophysiological measurement of stretched guinea pig spinal cord white matter for different

strains and strain rates [52], see Section 5.1. Section 5.2 proposes an extension framework for extrapolating axon bundle electrophysiology from individual axon electrophysiology, based on the mechanical-electrophysiological single axon model, *Neurite*, published by Jerusalem et al. [1] (see Chapter 2 Section 2.4 for details). The extended framework is then linked with an optimisation framework to perform systematic parameter search to obtain the best calibration against the experimental reference, see Section 5.3. Two models were optimised through this framework: (i) an axonal fibre bundle, see Section 5.3 (ii) a representative single axon model with the diameter as an extra parameter, see Section 5.4. These two models were then compared to investigate whether an axon bundle model (considering a range of conduction properties) is needed, or could be replaced by a representative single axon model, to capture rate dependent stretch induced electrophysiological deficits.

5.1 Experimental study

The experimental studies by Shi et al. [52] set out to measure the changes in CAP amplitude before and after different degrees of traumatising stretch. The pre-stretch CAP was measured in a double sucrose gap, an experimental rig with three chambers. The ends of the spinal cord segment were in the two end-chambers, submerged in intracellular ionic solution, while the rest of the spinal cord segment was in the middle chamber submerged in extracellular solution. The chambers were separated by concentrated sucrose, acting as a high impedance partition. One of the end chambers had a stimulating electrode to induce AP in the spinal cord segment. The resulting signal can then be measured as a potential difference between the middle and the other end chamber with electrodes, see Figure 5.1. In addition to this set up, an impacting rod was used in the middle chamber to impose different degrees of traumatising stretches, while the CAP was then measured again after stretch.

The post-stretch CAP as a percentage of the pre-stretch CAP was used as an evaluator of the change in CAP after the mechanical stretch. During the experiment, subsequent CAP measurements were also done after the initial injury to observe a recovery of CAP amplitude accompanying a 30 min stress free relaxation of the spinal

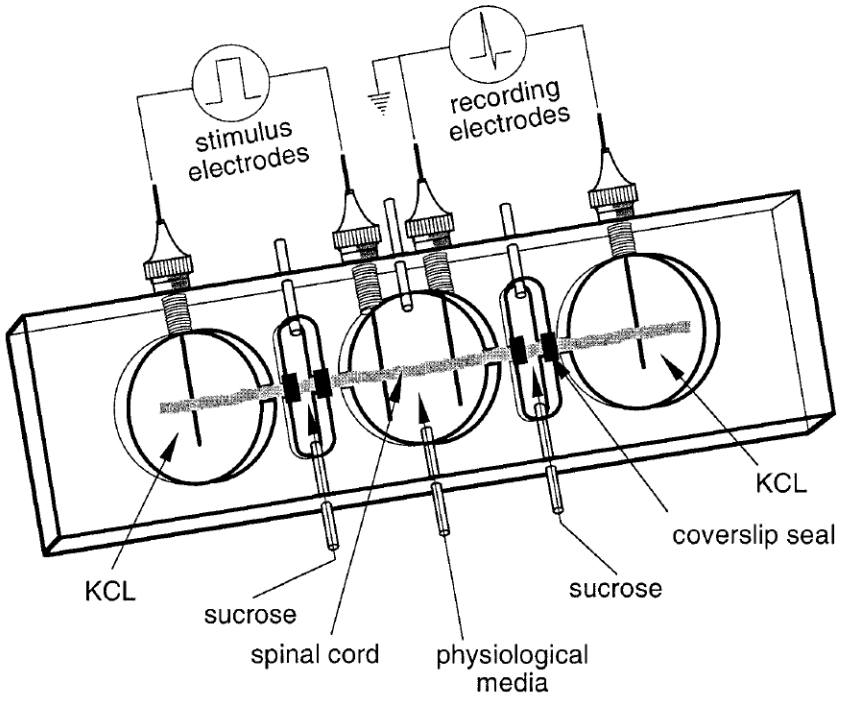

Figure 5.1: Double sucrose gap set up [52]. Permission to reproduce this image has been granted by Prof. R. Shi.

cord segment. CAP measurements were measured at 5 min intervals. In Figure 5.2, the percentage of CAP post-stretch compared to pre-stretch vs. relaxation time is presented. The findings show that a higher strain, and a higher strain rate in general, causes a larger CAP reduction, which are recoverable to varying degrees over 30 min.

5.2 Axonal bundle model

The model using *Neurite* published by Jerusalem et al. [1] uses a reference axon diameter of 3 µm to capture tissue level electrophysiology. However wide ranging geometrical variations are observed within the axon population of a fibre [139–145]. The characteristics of one AP are reflective of the conduction properties of the axon of interest, in turn dependent on its geometrical features [146], such as diameter, nodes of Ranvier sizes or internodal lengths. Previous morphometric studies of axons observed variances in all the aforementioned geometrical parameters [140–145]. Furthermore, a normal distribution was observed in axon calibres for

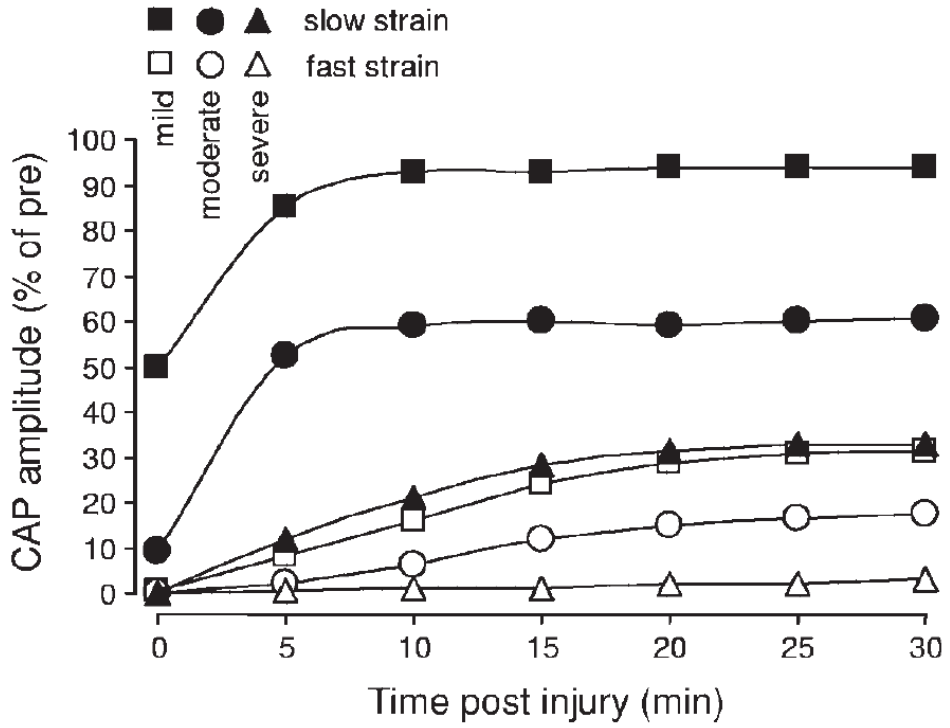

Figure 5.2: CAP amplitudes of six loading cases (presented as a percentage of the pre-strain signal) during the 30 min mechanical stress free relaxation [52]. Permission to reproduce this image has been granted by Prof. R. Shi.

different species, such as rats and guinea pigs [51, 139]. The g-ratio (the ratio of inner axonal diameter to the total outer diameter [125, 146]) is a good indicator of axonal myelination and when assuming a constant inner axonal diameter and myelin layer thickness, the number of myelin layers can be deduced. This ratio can vary slightly from species to species, and also from healthy to injured axons [5, 57, 125]. In terms of mechanically induced electrophysiology deficits it is desirable to study the relationship between a population's geometrical characteristics and one hypothetical representative characteristic. The need for a collective behaviour within an axonal bundle may hypothetically be rationalised through the need for signal redundancy. From a computational perspective, it is more desirable and practical to consider one unique representative axon. The rest of this section therefore details a framework for extending *Neurite* up to an axonal fibre model, by taking into account realistic geometrical characteristics, in order to compare it to a single axon in terms of modelling mechanically induced electrophysiology deficits.

In order to create the fibre model, morphometric relationships for guinea pig axonal calibre, internodal length and number of myelin layers were obtained from Hilderbrand et al.[127].

Linear fits were used to approximate the relationship between internodal lengths and the number of myelin layers, and between internodal lengths and axon diameter, see Figure 5.3a and 5.4.

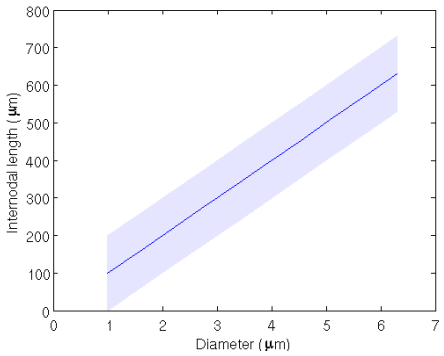

(a) Internodal length vs. diameter relationship

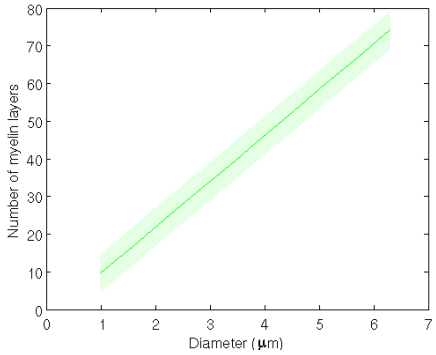

(b) Number of myelin layers vs. diameter relationship

Figure 5.3: Geometrical relationships extracted from morphmetric studies of guinea pig axons [127].

The internodal length was estimated to be 100 times the axon calibre [127]. The smallest diameter in the fibre model was estimated to be 0.7 µm [139], and therefore the smallest internodal length was determined to be 70 µm. The number of myelin layers were estimated to be 12 times the diameter value of the axon calibre in micrometres (the slope in Figure 5.4)[127]. In the experiments conducted in a double sucrose gap [52], the spinal cord segment were over-stimulated with a large voltage, therefore one assumption was that the axons recruited in the CAP reflects the axon population within the cord segment. There are numerous axons within the experimental sample, and it would be impractical and computationally expensive to simulate all of them. Figure 5.4 presents the reported diameter distribution for the guinea pig spinal cord [52].

In order to simplify the model to a representative population, the data from Figure 5.4 were taken to extract the relative ratios of the different diameter bins

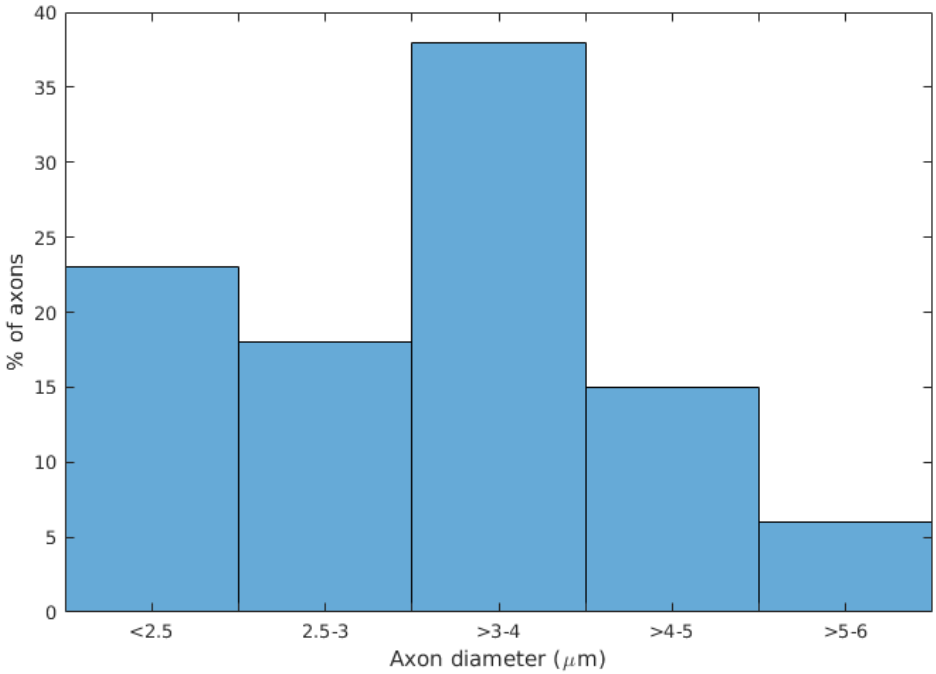

Figure 5.4: Distribution of diameters in the nerve fibre obtained from guinea pig spinal cord axons [52].

in the histogram. One set of diameters was used and a random diameter within each bin was chosen by a random number generator. Each internode was assigned a length and a number of myelin layers within the range corresponding to its diameter generated by a random number generator. Two axons were used to approximate the smallest histogram bin (axon diameter of 5-6 µm), and the number of axons per bin for the other bins was chosen proportionally. The minimum number of axons to approximate this population was hence determined to be 27, composing of six axons under 2.5 µm, five between 2.5-3 µm, ten between 3-4 µm, four between 4-5 µm and two between 5-6 µm. Random diameters within each bin were generated to form the bundle, each with 200 nodes and internodes following the geometrical relationship mentioned above.

Scaling rule for CAP The AP of each axon is obtained at the same point, at 10 mm from the start of the axon. The resultant APs are then averaged using the following scheme to interpolate to an overall signal of a fibre. The contribution

of a single axon towards an overall CAP was assumed to be proportional to its circumferential area. This assumption was based on the fact that the ion channels reside on the membrane. If the density of ion channels per unit membrane area is constant, larger axons will produce a larger current, hence resulting in a larger contribution to the overall CAP [147]. This simple scaling rule was adopted for this study and the axon's AP was assumed to be proportional to its diameter, see Figure 5.5.

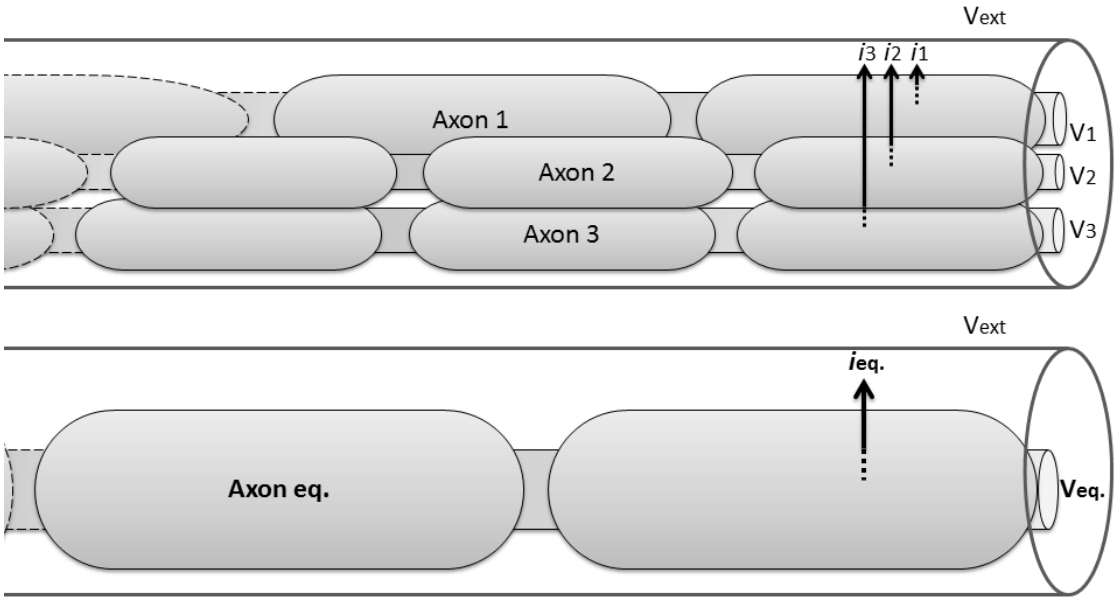

Figure 5.5: Nerve and representative axon.

In a single axon (e.g., axon 1 of Figure 5.5) that is stimulated by an input voltage, the resultant potential measured locally is V_1 is such that

$$V_{ext} - V_1 = i_1 R_1 \tag{5.1}$$

and for the n^{th} axon,

$$V_{ext} - V_n = i_n R_n \tag{5.2}$$

where V_{ext}, i_n and R_n are, respectively, the extracellular potential, the current leaving axon n and its instantaneous resistance in the vicinity of the measurement point.

In a double sucrose gap, and applying the analogy of parallel resistors, the following can be obtained:

$$V_{ext} - V_{CAP} = i_{Total} R_{Total} \tag{5.3}$$

where

$$R_{Total} = \frac{1}{\frac{1}{R_1} + \frac{1}{R_2} + \frac{1}{R_3} + ... + \frac{1}{R_n}} \tag{5.4}$$

$$i_{Total} = i_1 + i_2 + i_3 + ... + i_n \tag{5.5}$$

By using Equation (5.2), Equation (5.3) becomes:

$$V_{ext} - V_{CAP} = V_{ext} - \left(\frac{1}{\sum_j^n \frac{1}{R_j}} \sum_i^n \frac{V_i}{R_i} \right) \tag{5.6}$$

As the resistances R_i are related to the patches of membrane in the vicinity of the measurement point, and therefore by definition inversely proportional to the axon diameters d_i, this leads to:

$$V_{CAP} = \frac{1}{\sum_j^n d_j} \sum_i^n V_i d_i \tag{5.7}$$

Accordingly, the larger the axon, the higher its contribution towards V_{CAP}. For example, an ideal case of three identical axons all with the same geometry (see Figure 5.6) will therefore have the same resistance, and

$$V_{CAP} = \frac{1}{3}(V_1 + V_2 + V_3) \tag{5.8}$$

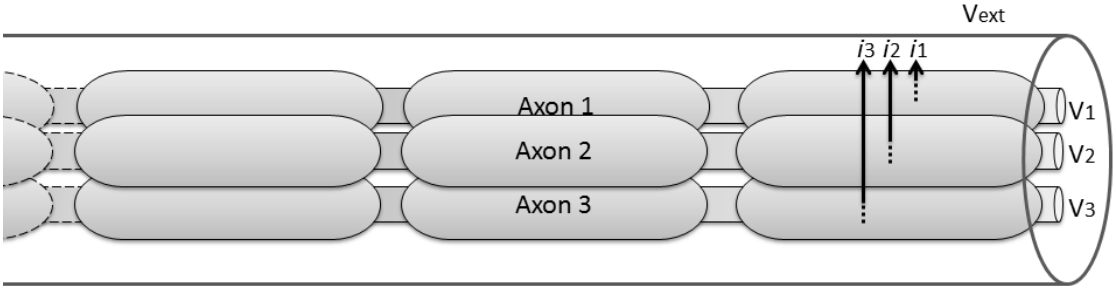

Figure 5.6: A case with three identical axons.

This method of scaling may seem straightforward for axons with the same morphology (identical APs), however the assumption of identical morphology is far from reality in biological nerves. APs will differ between axons of different morphologies; furthermore, the same level of strain will affect axons of different calibre differently. The following sections will explore the modelling of electrophysiological alteration at various levels of strain and strain rate based on the above scaling rule.

5.3 Calibration of axonal fibre model

Neurite was incorporated into a multithread framework to handle the simultaneous computation of the 27 axons of the aforementioned scaling framework to produce a CAP. In order to compare the effectiveness of a single representative axon and of the 27-axon bundle. The simulated fibre had a length of 10 mm, the same as for the simulations presented by Jerusalem et al. [1]. The electrophysiological parameters of each axon was assumed to be the same and the parameters reported in Jerusalem et al. [1] were used in this study (also listed in Table 3.2).

To trigger the APs, three voltage stimuli of duration 3 ms were used in this study (as opposed to a single stimulus as used by Jerusalem et al. [1]). First, the fibre was triggered twice in quick succession one after the other (at time t=20 ms and t=33 ms), then at t=150 ms the fibre was triggered again. The reason to adopt this pattern was that it was often observed that a new resting potential can be established for some of the loading cases (especially Cases 3 and 4, see Table 5.2). Therefore the first two triggers were used to establish a new stable resting potential before an AP was recorded. Without this triggering system, post stretch CAP for Cases 3 and 4 can have an abnormally large amplitudes, since it is possible for the damaged nerve to establish a new resting potential. From a model point of view, allowing the HH model to first establish a new resting potential by triggering it, then triggering it again for an AP is closer to what is measured experimentally. The total simulation time was 300 ms, this was chosen to be long enough to observe all APs initiated by the three triggers. Note that $V_{rest} = -65$ mV in all simulations in this study.

In terms of optimisation methodology, an evolutionary technique – differential evolution – was used to search for the free parameters value. Differential evolution is an iterative optimisation method based on a fitness function [148]. Differential evolution creates new candidate solutions and combines the existing candidates with the best fitnesses. This method was chosen for this application due to its ability to search large spaces and robustness to noise [148]. The evolutionary optimisation framework was developed by Dr. Antonio Latorre, and the calibrations presented here were done in collaboration.

Parameter	Definition
E	Young's modulus
k	Damage evolution
η_{eq}	Equivalent η
$\tilde{\varepsilon}$	Microscopic strain threshold
κ	Sensitivity parameter for microscopic relaxation
γ	Coupling sensitivity exponent

Table 5.1: Calibrated model parameters [1].

The 27-axon model was coupled with the optimisation algorithm, which was used to calibrate seven parameters, listed in Table 5.1. The model fit was evaluated by its ability to match the experimental electrophysiological deficits – the percentage of CAP reduction due to a loading case (six loading cases in total, see Chapter 2, Section 2.4) relative to a signal of a non-loaded bundle. The fitness function, F, is defined as the accumulative score for each time point compared to the experimental reference (see Figure 2.2):

$$F = \sum_{i,j} \left| CAP^{s}_{ij} - CAP^{e}_{ij} \right| \tag{5.9}$$

where i represents the different loading cases (listed in Table 5.2), j represents 5 min time interval up to 30 min, and where CAP^{e}_{ij} correspond to the CAP of loaded Case i at time j relative to the non-loaded case for the simulation/experiment, see Table 5.2.

Case	Description	$\dot{\varepsilon}$ (s^{-1})	ε_{max} (%)
1	Slow-mild	0.006-0.008	25
2	Slow-moderate	0.006-0.008	50
3	Slow-severe	0.006-0.008	100
4	Fast-mild	355-519	25
5	Fast-moderate	355-519	50
6	Fast-severe	355-519	100

Table 5.2: Tensile tests loading conditions [1].

In order to speed up the optimisation, the number of parameters optimised were reduced using the relationships listed below,

$$\eta_{eq} = (\eta_1^- + 1/\eta_2^-)^{-1} \tag{5.10}$$

$$\kappa = \frac{\eta_1^-}{\eta_1^- + \eta_2^-} \tag{5.11}$$

where η_1^- and η_2^- are the tissue active molecular reorganisation viscosity and the viscous molecular cross-linking between the axon and its surrounding structures as during stress free relaxation, as reported by Jerusalem et al. [1].

Calibration results Figure 5.7 presents results of the 27-axon the model calibrated by the optimisation algorithm plotting (CAP reduction vs. time). The calibrated parameter values are provided in Table 5.3. At t=0 min, the bundle model experiences a total conduction block except for the mildest strain at the slowest strain rate (Case 1). The CAP for Case 1 at t=0 min was predicted to be just over 90% of the pre-stretched CAP. While this data point is quite similar to the experimental value presented in Figure 5.2, the CAP at the subsequent relaxation time is higher, which is contrary to the experimental trend. The reason is that the strain was at its highest at t=0 min before the relaxation has begun. The axons with diameters between 2.1 µm and 5.8 µm (22 out of the 27 axons) used to build the axon bundle signal become ectopic due to the alteration in the reversal potentials under mild strain and slow strain rates. The ectopic conduction produced in this model was a result of the altered Na_V and K_V reversal potential based on membrane strain (see Equation (2.8)). If the new reversal potentials cannot establish a resting

potential, then the conduction will evolve to be ectopic. This effect is then alleviated as the axon enters relaxation, and therefore the CAP for Case 1 from t=5 min onwards becomes slightly lower. For the other loading cases however, the maximum loading at t=0 min is far too severe, therefore resulting in total conduction block instead of ectopic conduction. As the fibre bundle relaxes, at t=5 min onwards, the fibre regains some of its conduction ability for Cases 2, 3 and 4.

The axon bundle model predicts total conduction block for moderate and severe strain at fast strain rate (Cases 5 and 6, respectively), where axons can not recover conduction even after 30 min of stress free relaxation. This is different to the experimental data where the tissue was still able to recover $\approx$ 20% of CAP for Case 5 and $\approx$ 5% for Case 6.

Parameter	Value
E	491 337
k	968 781
η_{eq}	5.55529e+06
$\tilde{\varepsilon}$	0.058985
κ	0.015625
γ	2.16269

Table 5.3: Calibrated model parameters values for axon bundle model.

5.4 Calibration of representative axon model

It is commonly observed that conduction magnitude increases with axon calibre, and that thinner axons produce a smaller AP output [149]. Axons of different diameters not only have different conduction properties, but also mechanical properties: smaller axons are more likely to be susceptible to damage, resulting in a higher number of bleb occurrences and higher permeability to non-native particles after stretch [51, 150].

Since the axons with a smaller diameter are more likely to be damaged, and as they output a smaller amplitude of AP, one of the questions that arise is whether the conduction from the smaller axons can be lost and thus whether the resulting

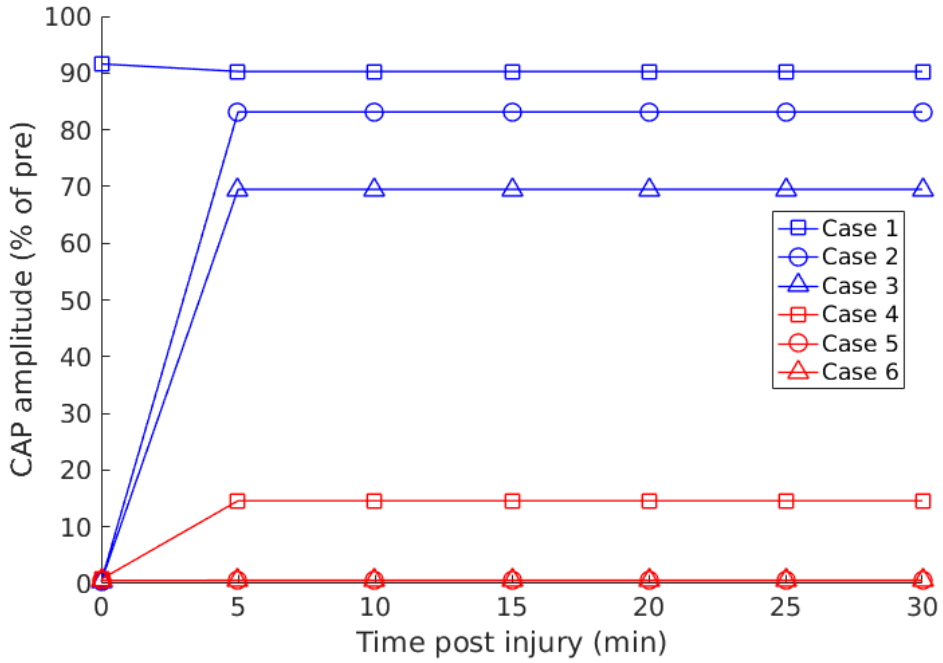

Figure 5.7: CAP recovery simulations using 27-axon fibre model.

signal on a larger scale could be reduced to be represented by the signal of a prominent axon of a higher calibre. This study involves a systematic search using the aforementioned optimisation method to search for an axon with a diameter that gives the most representative altered electrophysiological signal. The search was done on a range of observed diameter sizes. The optimisation algorithm was modified to include diameter as an extra parameter to conduct the systematic search. The optimisation found that an axon with a diameter of 6.52 µm gives the best fit to the experimental reference.

Calibration results Figure 5.8 presents the results of the representative axon model calibrated by the optimisation algorithm (CAP reduction vs. time). The calibrated parameter values are given in Table 6.3. At t=0 min, the axon model experiences a total conduction block except for Case 1. Here, the CAP for Case 1 at t=0 min has significantly reduced but not to the level of total conduction block. As the axon bundle relaxes, at t=5 min and onwards, only Cases 1 and 2 demonstrated recovery, with Case 1 regaining conduction completely and Case

2 close to total recovery.

Parameter	Value
E	606 605
k	5 390 980
η_{eq}	3.6914e+07
$\tilde{\varepsilon}$	0.0194079
κ	0.4
γ	3.43963
diameter	6.325 85 µm

Table 5.4: Calibrated model parameters values for single axon model.

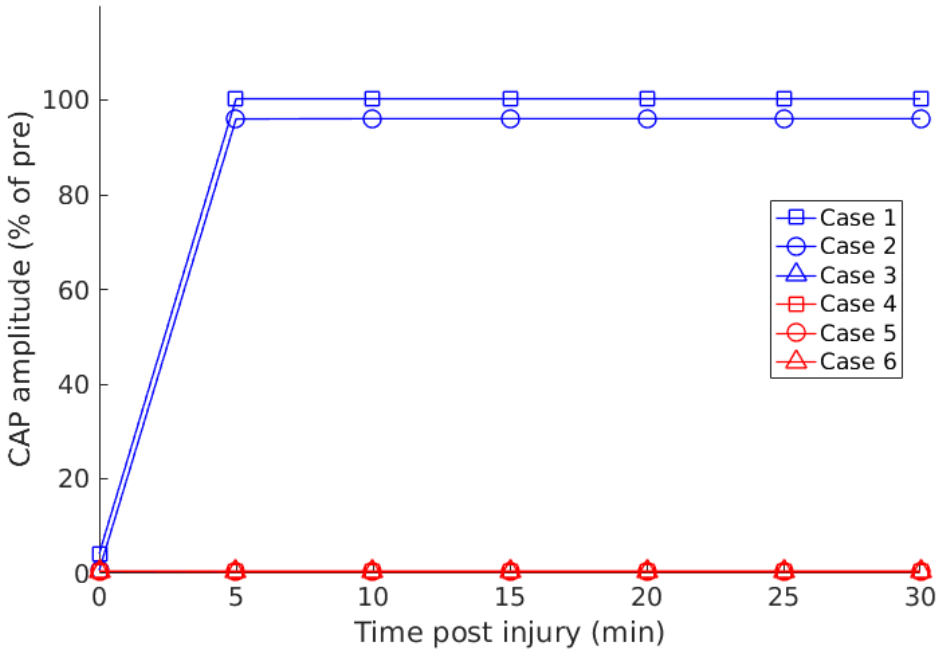

Figure 5.8: CAP recovery simulations using single axon model.

5.5 Discussion

The main aim of this study is to test whether the inclusion of microstructure heterogeneity details such as axon diameter, internodal lengths and number of myelin layers to build a fibre model can enrich the mechanical electrophysiological coupling compared to a single axon model.

In terms of capturing the magnitude of the recovered conduction loss at t=30 min, the fibre model was able to better capture the tendencies of Cases 1, 2, 3 and 4 compared to the single axon model. The average signal from a group of axons with representative microstructural geometries has shown to have more resilience in terms of its electrophysiological CAP propagation compared to a single axon for the same damage law.

Compare to the original experimental data (Figures 5.7 and 5.8), it can be seen that the behaviour of the single axon model and the 27-axon fibre model is less gradual compared to the experimental data and the calibration by Jerusalem et al. [1]. Both the fibre and the single axon models presented more conduction blocks during the relaxation time, and both failed to capture the transient phase (t=5 - 10 min) in the recovery that is present in the experimental data and by Jerusalem et al. [1].

In healthy nerve tissues, axons of different calibres exist to conduct electrophysiological signals. Larger and smaller axons have different conduction speeds and this allows information to be encoded temporally in the signals [139]. This study has theoretically demonstrated that this heterogeneity may not only serve a purpose in healthy nerves, but also in terms of protective mechanisms of nerves when subjected to mechanical damage. The redundancies and heterogeneity included in the fibre model provided more resilience to the CAP conduction compared to that of a single axon.

It is important to comment that both models appear to perform quite poorly relative to the calibration performed by Jerusalem et al. [1]. This is due to the fact that the three stimuli were used to trigger an AP instead of only one stimulus that was used by Jerusalem et al. The three-trigger approach ensured that the axon was at a new settled resting potential before measuring the CAP loss, while the original model took an unstable resting potential as a reference, leading to biased results. This new resting potential is the result of the altered reversal potentials of the Na_V and K_V channels of the HH model. This effect can be observed here in both the representative axon and the fibre model. Through the dependence of

reversal potential on the membrane strain (similarly observed by Boucher et al. [2]), it was chosen here to exclude the effect of the new resting potential by using three triggers. Since only relative CAP loss values were reported, it was assumed that new resting potentials could often be established experimentally.

The single axon and fibre model studies have shown that it is complicated to represent altered electrophysiology on a higher length scale in terms of linear combination of altered axonal electrophysiology. One possible explanation is that the overall altered CAP is not a linear combination of the altered axonal AP. For example, demyelination is commonly observed as a secondary injury hallmark, and it has sometimes been observed as early as 30 min [5], potentially introducing complex signal attenuation and time delays in propagation within a nerve bundle. Another damage mechanism that could occur within the 30 min recovery window could be the influx of Ca^{2+}, which alters the functioning of the Na^{+}/Ca^{2+} exchanger [49], therefore increasing the complexity of the ion imbalance of Na^{+} and K^{+}, contributing to reasons why the altered electrophysiology for one axon, as well as a bundle of axons, may not be straightforwardly modelled by the damage model used in *Neurite*. Despite the shortfall of the above models in terms of secondary ion dynamics, it is important to acknowledge that the consideration of the axon population redundancies has a beneficial effect on capturing the electrophysiological coupling. The fibre model would have the capability to model a more graded response as some of the smaller axons become more damaged electrophysiology under a certain strain and strain rate, while the response of a single axon model is more binary in comparison. Therefore it maybe advisable to consider a fibre model when studying and modelling axonal tracts.

Other than a potentially indescriptive electrophysiological model, it is also possible that the micromechanics model proposed by *Neurite* may not be capturing the mechanical damage and recovery that is present in an axon within a tissue segment. The mechanical model in *Neurite* was formulated with the infinitesimal strain theory, while the macroscopic and microscopic levels were linked with a viscous dashpot. It is not straightforward that this is the mechanical relationship

between the two length scales, furthermore, it is not yet feasible to validate this kind of multiscale model in biological tissues. It is possible that the reason the altered CAP can not be modelled by a linear combination of altered AP is a combination of the reasons mentioned above. In order to further investigate this issue, the next chapter will present the mechanical-electrophysiological coupling formulated in a finite deformation framework directly at the tissue level to eliminate the complexity of a micromechanics model.

6

Modelling tissue scale mechanically induced electrophysiological alteration

Contents

6.1 Constitutive model framework 82
6.1.1 Mechanics 82
6.1.2 Electrophysiology 86
6.1.3 Coupling of mechanics and electrophysiology 87
6.2 Calibration 87
6.2.1 Mechanical model calibration 87
6.2.2 Energies evaluation 89
6.3 Results 90
6.4 Discussion 93

The model development and calibration presented in this chapter were done in collaboration with Dr. Daniel Garcia Gonzalez. Dr Garcia Gonzalez derived the hyperelastic constitutive model, implemented the Aliev-Panvilov model and derived the energy equivalences between mechanics and electrophysiology.

In the previous chapter, the single axon and nerve fibre studies have highlighted the difficulties arising from the consideration of multiple individual axons for the modelling of a fibre. In particular, such an approach could not fully capture the conduction loss under different loading cases, possibly due to the limitations of, i) the phenomenological electrophysiological model, ii) the mechanical model

which may not be adequate when modelling the micromechanics of axons within nerves, or iii) a combination of both.

Experimentally, it is feasible to obtain the mechanical behaviour of a tissue sample, and it is possible to get a reasonable calibration on the mechanical response. This chapter therefore begins by first focussing on the modelling of the macroscopic material behaviour of the tissue, see Section 6.1.1. In this chapter, the electrophysiology was not scaled from axonal electrophysiology and a tissue level electrophysiology model was adopted by directly relating the electrophysiology alteration to the mechanical free energy. The calibrated model (Section 6.1.2) was used to predict the tissue deformation in energetic terms during tensile loading and stress free relaxation (as in the experiments published by Shi et al. [52]). The overall results and a comparison with the axon and nerve fibre models (a linear combination of multiple single axon, described in Section 5.2) is presented in Sections 6.3 and 6.4.

6.1 Constitutive model framework

6.1.1 Mechanics

It is important to note that, in the experiments by Shi et al. [52], the strains that the spinal cord were subjected to were extremely large (up to 100%). Therefore, the established viscous characteristics that is common to biological tissue, requires the consideration of a finite deformation framework.

The Helmholtz free energy, Ψ used to deform a viscous material is partly stored in the material as elastic (recoverable) energy, Ψ^e, while the rest of the energy is dissipated by the viscous component (unrecoverable), Ψ^ν:

$$\Psi = \Psi^e + \Psi^\nu \tag{6.1}$$

Hyperelastic energy Hyperelastic constitutive models are commonly used for modelling the mechanical behaviour of soft tissues. The Ogden model is one of the most commonly used hyperelastic models for soft tissues [95, 110, 151, 152], and the

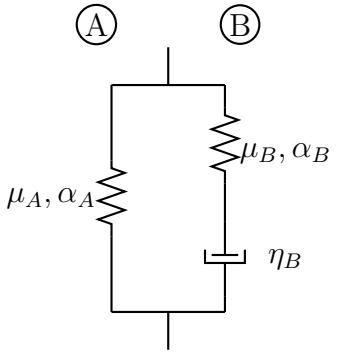

Figure 6.1: Schematic of the constitutive hyperviscoelasticity model

first order Ogden model has previously been calibrated for peripheral nerves [152]:

$$\Psi^e = \frac{\mu_p}{\alpha_p}(\lambda_1^{\alpha_p} + \lambda_2^{\alpha_p} + \lambda_3^{\alpha_p} - 3) \tag{6.2}$$

where μ_p and α_p are material parameters, such that $\mu_p \cdot \frac{\alpha_p}{2}$ is the equivalent shear modulus [95, 151], λ_1, λ_2 and λ_3 denotes the stretches in the principal directions.

Viscous energy The viscous energy arises from inelastic dissipation of the viscous components within the material. The dissipated energy at time t is calculated as follows:

$$\Psi^\nu = \int_0^t \boldsymbol{\sigma}^\nu \cdot \dot{\boldsymbol{\varepsilon}}^\nu dt \tag{6.3}$$

where $\boldsymbol{\sigma}^\nu$ and $\dot{\boldsymbol{\varepsilon}}^\nu$ are the stress and strain tensors in the viscous component.

Uniaxial loading The hyperviscoelastic constitutive model used in this chapter is composed of two branches: a pure elastic branch analogous to a hyperelastic spring and a viscoelastic branch analogous to a hyperelastic spring and a viscous dashpot in series, see Figure 6.1. For uniaxial stretch with the assumption of incompressibility (the Jacobian, $J = \lambda_1\lambda_2\lambda_3 = 1$, and $N = 1$), one can substitute $\lambda_2 = \lambda_3 = \lambda_1^{-\frac{1}{2}}$ to Equation (6.2), the hyperelastic spring in branch (A) is defined as the following:

$$\Psi_A^e = \frac{\mu_A}{\alpha_A}(\lambda_A^{\alpha_A} + 2\lambda_A^{-\frac{\alpha_A}{2}} - 3) \tag{6.4}$$

where μ_A and α_A are material parameters and $\lambda_A = \lambda_1$ for branch (A). The stress contribution of branch (A) can be derived from the energy as:

$$\sigma_A = \lambda_A \cdot \frac{\partial \widetilde{\Psi}_A^e}{\partial \lambda_A} = \mu_A(\lambda_A^{\alpha_A} - \lambda_A^{-\frac{\alpha_A}{2}}) \tag{6.5}$$

The strain in branch (B), ε_B is the sum of the strain from the hyperelastic and the viscous components:

$$\varepsilon_B = \varepsilon_B^e + \varepsilon_B^\nu \tag{6.6}$$

In large deformation, the stretch λ is used instead such that stretch and strain ε are related through the relation $\varepsilon = \ln \lambda$. By analogy in large deformation, Equation (6.6) is then expressed as:

$$\lambda_B = \lambda_B^e \lambda_B^\nu \tag{6.7}$$

According to the rheological model (Figure 6.1), the elastic component and the viscous component in branch (B) experience the same stress, i.e.,:

$$\sigma_B^e = \sigma_B^\nu \tag{6.8}$$

where the stress contribution from the hyperelastic component in branch (B) can be derived the same way as the stress contribution from branch (A):

$$\sigma_B^e = \mu_B \left(\lambda_B^{e(\alpha_B)} - \lambda_B^{e(\frac{\alpha_B}{2})} \right) \tag{6.9}$$

where μ_B and α_B are material parameters, and λ_B^e is the elastic stretch in branch (B). Here, a linear dashpot is assumed and

$$\sigma_B^\nu = \eta_B \cdot \dot{\varepsilon}_B^\nu \tag{6.10}$$

where $\varepsilon_B^\nu = \ln \lambda_B^\nu$, and λ_B^ν is the viscous stretch in branch (B) and η_B is the viscosity. By using Equations (6.8), (6.9) and (6.10), one obtains:

$$\eta_B \cdot \frac{\dot{\lambda}_B^\nu}{\lambda_B^\nu} = \mu \left(\lambda_B^{e(\alpha_B)} - \lambda_B^{e(\frac{\alpha_B}{2})} \right) \tag{6.11}$$

and

$$\dot{\lambda}_B^{\nu} = \frac{\mu_B}{\eta_B}\left(\lambda^{(\alpha_B)}\lambda_B^{\nu(1-\alpha_B)} - \lambda^{(-\frac{\alpha_B}{2})}\lambda_B^{\nu(1+\frac{\alpha_B}{2})}\right) \tag{6.12}$$

Experimental work on porcine spinal cord tissue has shown the tissue yields at high level of strain ($\sim 70\%$) [153]. In order to capture such yielding, a damage criterion was included in the formulation, whereby if the system exceeds a critical energy threshold, mechanical damage will occur. The corresponding mechanical damage evolution is governed by:

$$\dot{D}_{mech} = \begin{cases} \frac{\dot{\Psi}}{\Psi_f - \Psi_{crit}} & \text{if } \Psi > \hat{\Psi}_{crit} \quad \hat{\Psi}_{crit}(s) = \max\left\{\max_{s\in[\infty,t]}(\Psi(s)), \Psi_{crit}\right\} \\ 0 & \text{otherwise} \end{cases} \tag{6.13}$$

where D_{mech} is the mechanical damage parameter, Ψ_{crit} is the critical energy threshold where the material starts to fail and Ψ_f is the energy at which point the material has no load bearing strength remaining. Mechanical damage only occurs when the free energy of the system exceeds the critical energy. The current free energy threshold ($\hat{\Psi}_{crit}$) is taken to be the maximum between Ψ_{crit} or the maximum energy reached. The initial D_{mech} is taken to be zero. The final system of equations governing the three component mechanical model is therefore:

$$\begin{cases} \Psi_A &= \frac{\mu_A}{\alpha_A}(\lambda_A^{\alpha_A} + 2\lambda_A^{-\frac{\alpha_A}{2}} - 3) \\ \Psi_B &= \Psi_B^e + \Psi_B^{\nu} \\ \Psi_B^e &= \frac{\mu_B}{\alpha_B}(\lambda_B^{\alpha_B} + 2\lambda_B^{-\frac{\alpha_B}{2}} - 3) \\ \Psi_B^{\nu} &= \int_0^t \sigma_B^{\nu}\frac{\dot{\lambda}_B^{\nu}}{\lambda_B^{\nu}}dt \\ \Psi &= \widetilde{\Psi}_A + \widetilde{\Psi}_B \\ \widetilde{\Psi} &= (1 - D_{mech})\Psi \\ \dot{D}_{mech} &= \begin{cases} \frac{\dot{\Psi}}{\Psi_f - \Psi_{crit}} & \text{if } \Psi > \hat{\Psi}_{crit} \\ 0 & \text{otherwise} \end{cases} \end{cases} \tag{6.14}$$

This system of equations was solved by the forward difference method and implemented in Matlab. Note that in reality, the viscosity of the material would change as damage occurs. Here we capture the overall change in energy that damage incurs, rather than the change in material properties. This phenomenological approach was chosen as a proof of concept, but in the future it will be possible to use more sophisticated mechanical models when considering the mechanical-electrophysiological coupling at this length scale.

Uniaxial stress free relaxation During stress free relaxation, $\sigma = \sigma_A + \sigma_B = 0$ the flow rule is as follows:

$$\frac{\dot{\lambda}}{\lambda} = (\frac{\partial \sigma_A}{\partial \varepsilon} + \frac{\partial \sigma_B}{\partial \varepsilon^e})^{-1} \cdot \left(-\frac{\frac{\partial \sigma_A}{\partial \varepsilon} \cdot \frac{\partial \sigma_B}{\partial \varepsilon^e}}{\eta} \ln \lambda \right) \tag{6.15}$$

where $\lambda = \lambda_A$ ($\varepsilon = \varepsilon_A$), and $\frac{\partial \sigma_A}{\partial \varepsilon}$ and $\frac{\partial \sigma_B}{\partial \varepsilon^e}$ are the tangent moduli of the hyperelastic springs of branches (A) and (B), respectively. Note that the formulation presented above is only valid where no damage occurs. When damage occurs, the tangent moduli are modified to reflect the continual degradation of the material stiffness due to damage:

$$\begin{cases} \frac{\partial \sigma_A}{\partial \varepsilon} \Big|_{damage} = (1 - D_{mech}) \cdot \frac{\partial \sigma_A}{\partial \varepsilon} \\ \\ \frac{\partial \sigma_B}{\partial \varepsilon} \Big|_{damage} = (1 - D_{mech}) \cdot \frac{\partial \sigma_B}{\partial \varepsilon} \end{cases}$$

This set of equations allows for the determination of the stretch evolution with time during the unloading process. Finally, using the chain rule:

$$\begin{cases} \frac{\partial \sigma_A}{\partial \varepsilon} = \frac{\partial \sigma_A}{\partial \lambda} \frac{\partial \lambda}{\partial \varepsilon} = \frac{\alpha_A \eta_A}{2} \left(2\lambda^{\alpha_A - 1} + \lambda^{\frac{-\alpha_A - 1}{2}} \right) \lambda \\ \\ \frac{\partial \sigma_B}{\partial \varepsilon_B^e} = \frac{\partial \sigma_B}{\partial \lambda^e} \frac{\partial \lambda^e}{\partial \varepsilon_B^e} = \frac{\alpha_B \eta_B}{2} \left(2\lambda^{\alpha_B - 1} + \lambda^{\frac{-\alpha_B - 1}{2}} \right) \lambda^e \end{cases} \tag{6.17}$$

6.1.2 Electrophysiology

The FitzHugh-Nagumo (FHN) model simplifies the HH model to one phenomenological variable, leveraging on the fact that the gating variables n and h have a relatively slow kinetics to compare to m. FHN consists of the following system of equations [154].

$$\begin{array}{rcl} \frac{\partial v}{\partial t} & = & v(v-a)(1-v) - w + I \\ \frac{\partial w}{\partial t} & = & \tau(v - bw) \end{array} \tag{6.18}$$

where v denotes the dimensionless voltage of the fast variable, w denotes the recovery current, I denotes a current stimulus, τ controls the temporal scaling of the AP and a and b are the activation parameters. Both the activation parameters were tested, and both have a similar effect in terms of the AP amplitude as an output. The parameter b had a slightly larger input range and was therefore chosen for calibrating the electrophysiological change with the free energies of the mechanical system, detailed in Section 6.1.3.

6.1.3 Coupling of mechanics and electrophysiology

The mechanical component of the model is linked to the electrophysiological component by directly relating the free energy of the system to the electrophysiological damage parameter D_{elec} as:

$$\begin{array}{lcl} \frac{\partial v}{\partial t} & = & v(v-a)(1-v)-w+I \\ \frac{\partial w}{\partial t} & = & \tau(v-\frac{b}{1-D_{elec}}w) \\ D_{elec}(t) & = & \min\{\phi\Psi(t)^{\beta},1\} \end{array} \tag{6.19}$$

where Ψ is the free energy calculated by Equation 6.14, ϕ and β are parameters controlling sensitivity of the electrophysiological damage in the power law. Note that D_{elec} ranges from zero to one, where zero represents no damage, and one represents total conduction block.

6.2 Calibration

Since no information was reported regarding the geometry of the segment from Shi et al.'s experiments, a material point model was considered and calibrated for both the hyperviscoelastic model and the FHN model. The following aims to demonstrate that the free energy of the material has the potential to be a good parameter when considering coupling between mechanics and electrophysiology at tissue scale.

Firstly, the mechanical model is calibrated against experimental data in Section 6.2.1. Secondly, the energies of the system were predicted after the loading stage and at 5 min intervals of the relaxation stage (as reported in Shi et al. [52]) in Section 6.2.2. Finally, the energies were related to the FHN model through the coupling Equation (6.19).

6.2.1 Mechanical model calibration

The mechanical model is calibrated against a set of porcine spinal cord compression data published by Fradet et al. [153]. This data set was chosen because the range of strains and strain rates were the most similar to those in Shi et al. [52], and no experimental mechanical measurements of guinea pig spinal cord were

published. Although the material properties of porcine spinal cord may differ from that of guinea pig spinal cord, the stress-strain curve of the porcine spinal cord data exhibits a typical hyperelastic characteristics for soft tissues. Furthermore, it also exhibits typical strain and strain rate dependencies for soft tissues, therefore demonstrating it to be a good data set for obtaining the qualitative tendencies for spinal cord stress-strain dependencies.

During the parameter calibration of the mechanical model, it was important to respect several physical rules in order to assume that the mechanical model is meaningful. Firstly, for the Ogden model, the equivalent shear modulus is obtained from $\mu_i\alpha_i/2$, and the conditions $\mu_A\alpha_A \leq 0$ and $\mu_B\alpha_B \leq 0$ must hold [151]. Secondly, based on many experimental studies on mechanical tests of soft nervous tissues [6, 155, 156], the stress at a given strain has commonly observed to be lower in compression than in tension. Finally, the viscous component (η_B) was carefully chosen such that it still displays viscous behaviour even at the highest strain rate in the experiments ($\dot{\varepsilon}_{max} = 519s^{-1}$).

The mechanical parameters μ_A, α_A, μ_B, α_B and η_B were calibrated through optimisation using the Nelder-Mead simplex algorithm implemented as the *fminsearch* function in Matlab. Figure 6.2 shows the experimental spinal cord compression stress strain curve along with the calibrated model predicting stress under three different strain rates: $50\,\mathrm{s}^{-1}$, $5\,\mathrm{s}^{-1}$ and $0.5\,\mathrm{s}^{-1}$.

Parameter	Value
μ_A	-2.1943×10^4
α_A	-4.6811
η_A	8.8631×10^3
μ_B	-1.3286×10^4
α_B	-3.9456
Ψ_{crit}	7.4856×10^4
Ψ_f	4.8472×10^5

Table 6.1: Calibrated parameters of the hyperviscoelastic mechanical model (to the nearest 5 significant figures).

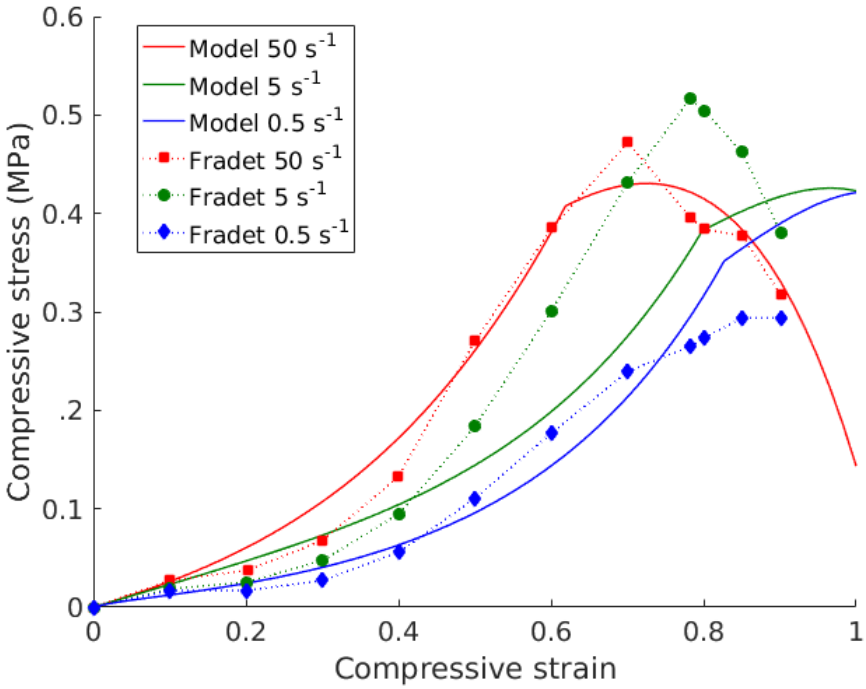

Figure 6.2: Model calibration with compression data by Fradet et al. [153].

6.2.2 Energies evaluation

The model was loaded following the loading in Shi et al. [52]. For each loading case (see Section 5.2), the free energy during relaxation (post loading) was generated at 5 min intervals for the evaluation of the mechanical damage in the rheological system, see Table 6.2. Note that energies from 10 to 30 min are not presented as they did not change. The following values were used for the calibration of the electrophysiology conduction loss.

	Free energies (Joules)		
Case	t=0 min	t=5 min	t=30 min
1	2189	1146	1146
2	8442	4708	4708
3	38419	24333	24333
4	6381	3267	3267
5	24881	12265	12265
6	92241	39634	39634

Table 6.2: Energy values during relaxation. The energies between 5 and 30 min are not presented as they did not change.

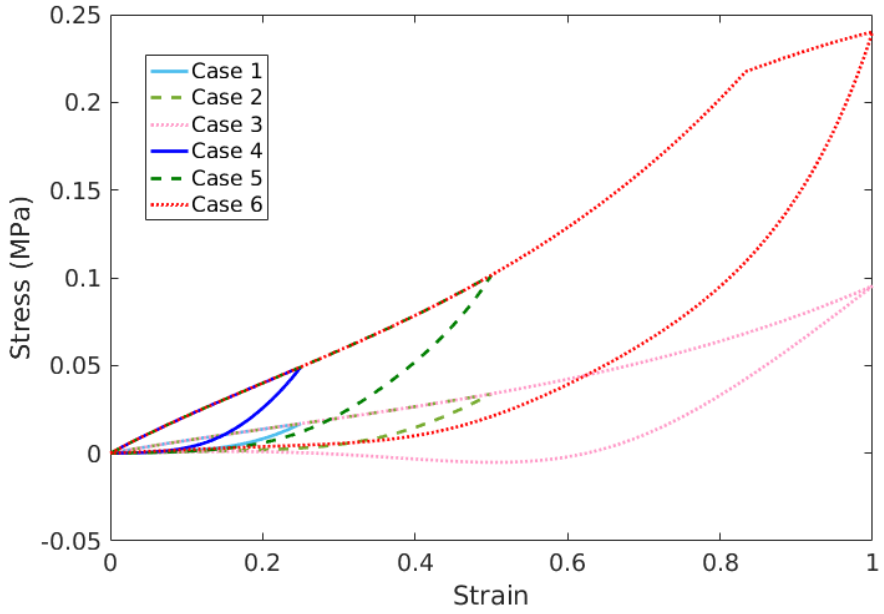

Figure 6.3: Loading according to the experimental strains and strain rates in Shi et al. [52]. Unloading/ relaxation generated from the hyperviscoelastic model.

Figure 6.3 shows the stress-strain curves of the tensile loading followed by unloading/ relaxation as generated by the model in each case. The value for D_{elec} were then calculated using Equation (6.19) while the damage sensitivity parameters ϕ and β were calibrated so that the resulting electrophysiological evolutions best fit their experimental counterparts using standard linear regression.

Parameter	Value
ϕ	0.13393
β	0.18954
a	0.4
b	$\frac{a}{(1-D_{elec}(t))}$

Table 6.3: Calibrated parameters of the FHN electrophysiology model (to the nearest 5 significant figures).

6.3 Results

Figures 6.4a and 6.4b shows the final calibrated results in terms of electrophysiological conduction deficit (see also Chapter 5, Section 5.3). In the experimental data

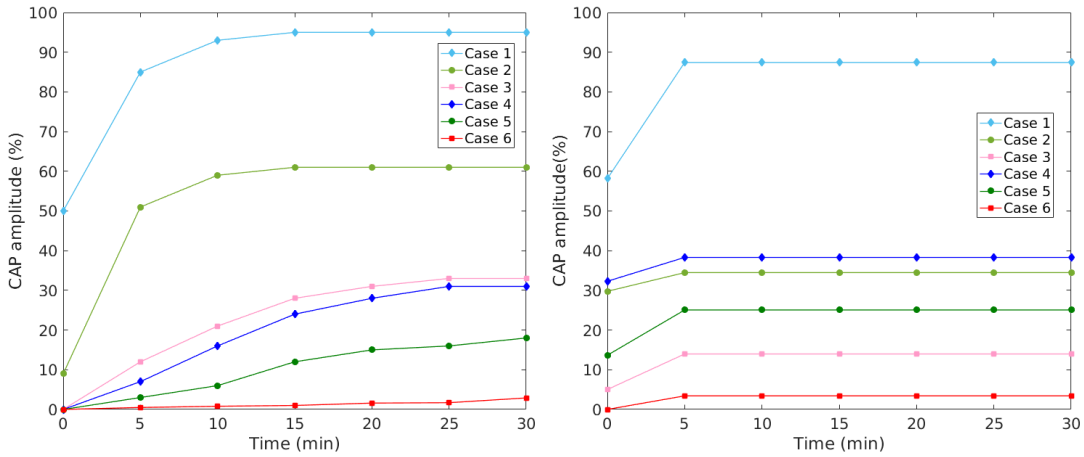

(a) Experiment **(b)** Model

Figure 6.4: Experimental conduction deficit (a) and calibrated conduction deficit (b).

(Figure 6.4a), a lower strain generally means a lower loss of conduction (i.e., a higher CAP %). The model has captured this mechanical-electrophysiology tendency well, where the CAP losses were predicted to increase with strains. As seen in Figure 6.4b, the model predicted Case 1 (mild strain) to have the smallest CAP loss ($\approx 90\%$), followed by Case 2 (moderate strain) to have $\approx 35\%$ CAP and followed by Case 3 (severe strain) with $\approx 15\%$ CAP. A similar trend can be observed for predictions at high strain rates in Cases 4, 5 and 6.

In the experimental data, see Figure 6.4a, the conduction losses at slow strain rates were less than the conduction losses at fast strain rates, i.e., Cases 1, 2 and 3 all have less conduction loss compared to Cases 4, 5 and 6. The model here was able to capture the most extreme cases, i.e., Case 1 (mild strain at slow strain rate) and Case 6 (severe strain at high strain rate). The model presented some discrepancies in terms of the CAP % of Cases 2 and 3 (moderate and severe strain at slow strain rates) compared to Cases 4 and 5 (mild and moderate strain at high strain rates). Experimentally, Cases 2 and 3 experienced a smaller loss in CAP, while the model predicted the contrary.

In general the predicted conduction recoveries show faster rise times than the experimental results. The rise times of the model were all shorter than 5 min, while the experimental data show rise times of 15 min. Currently in the model, the recovery

of the CAP has a similar rise time as the mechanical recovery. However, it is clear from the model that the stress free relaxation is faster than the electrophysiological recovery observed experimentally, suggesting that there is slower dynamics involved in the electrophysiological recovery. Although this model may not be suitable for modelling the transitional phase of the recovery of CAP, the predictions of initial CAP loss and the steady state CAP loss at 30 min are still valid.

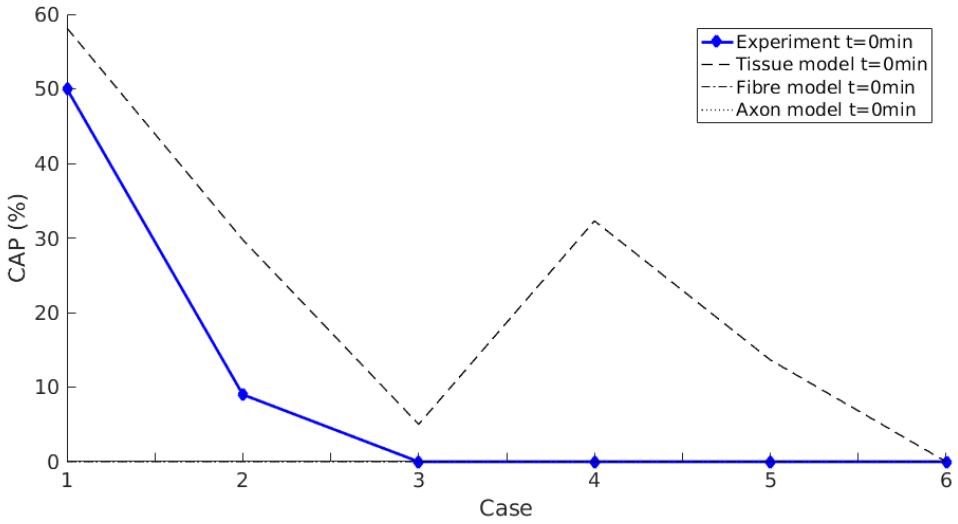

Figure 6.5: Comparison between experimental, tissue, fibre and axon model at t=0 min post loading.

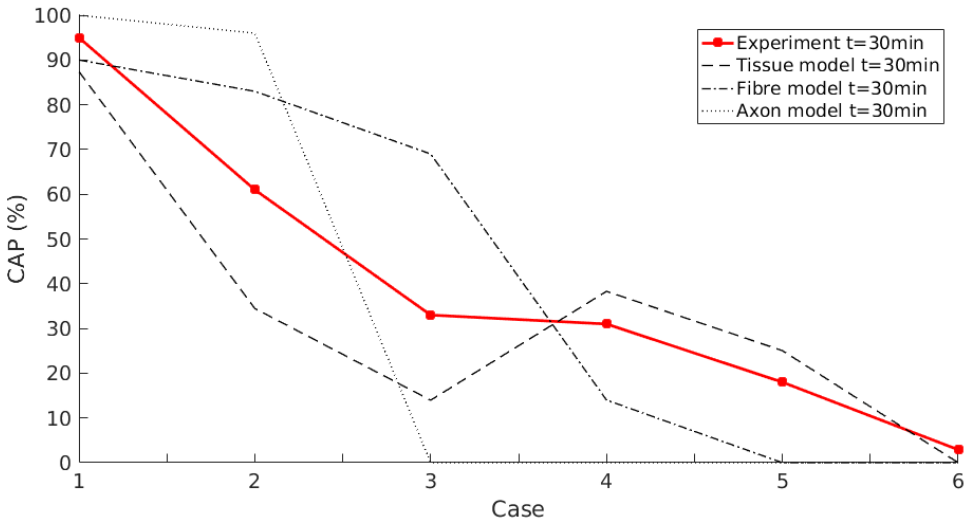

Figure 6.6: Comparison between experimental, tissue, fibre and axon model at t=30 min post loading.

In Figures 6.6 and 6.5, the CAP amplitude percentage at t=0 min and t=30 min are plotted against their corresponding cases for comparison between the three different models reported in this chapter and the previous chapter: tissue, fibre and axon model.

At t=0 min (Figure 6.5), only the tissue model was able to capture experimental tendencies at lower strain rates. Other than the discrepancies for Cases 3 and 4, the tissue model performed the best at capturing the inital CAP % tendencies, while the fibre and tissue models predicted total conduction loss for all cases. At t=30 min, presented in Figure 6.6, both the tissue (dashed line) and the fibre models (dash-dotted line) captured the general trend of steady-state conduction loss, while the axon model predicted the conduction loss poorly for Cases 1 and 2, and predicted total conduction for the other cases.

6.4 Discussion

The tissue level model presented in this chapter used a novel approach of free energy evaluation for characterising the amount of electrophysiological properties alteration in the system. The advantage of this model is that the mechanical model can be straightforwardly calibrated with available mechanical experimental data, as presented in Section 6.2.1. With the free energy approach, this model is able to capture the experimental tendencies for conduction loss at t=30 min for mild, moderate and severe strains.

As previously discussed, the tissue level model was able to capture the general tendencies of CAP conduction loss as strain increases. In terms of predicting the strain rate dependencies of the CAP loss, the prediction for Cases 2 and 3 (moderate and severe strain at low strain rates) were higher compared to Cases 4 and 5 (mild and moderate strain at high strain rates), contrary to experimental findings. This discrepancy is related to the energies predicted by the mechanical model, as seen in Figure 6.3 and Table 6.2. In particular, for Cases 3 and 4, the free energy predicted by the mechanical model in the system is much greater at a higher strain even at a lower strain rate (Case 3) than at a lower strain at a high strain rate (Case

4). It is important to note that this does not mean that the mechanical model does not provide a good prediction of the mechanical response. The fact that all three models presented in Figure 6.6 did not capture the transitional phase of the conduction recovery from 5-15 min, may actually indicate the fact that the mechanical recovery can not be straightforwardly linked with electrophysiological conduction recovery. Even though resealing of membrane has been experimentally observed to have a similar rise time as the recovery of electrophysiology in axons [51, 52], it is possible that across 30 min within a tissue sample, there are more complex secondary mechanisms that are likely to occur and contribute to the overall change of the CAP during the 30 min of relaxation or even during slow rate loading. For example, ion channels with slower dynamics such as Ca^{2+} channels were not considered in any of the electrophysiological models above and could have a large contribution to the CAP dynamics [4, 157].

Furthermore, the advantage of the tissue level model over the fibre model is the reduced number of parameters. The fibre model presented in Chapter 5 is a linear combination of multiple single axon models. Although it has the ability to capture the effect of microstructures on the mechanical electrophysiological coupling, the shortfall of that model is that it will require parameters governing the morphometric distribution of the number of myelin layers, internode length and axon diameter. The fibre model needs six parameters for the calibration model in addition to three morphometric relationships: internodal length vs. axon diameter, number of myelin layers vs. axon diameter and axon diameter distribution within the population. This could be impractical if the fibre model was to used to scale up to a much larger length scale across a large population of axons, or if the morphometric information for that axon population is not readily available. The fibre model is more suitable for studying a small population of axons for tissue of the scale of an axonal tract. The tissue model needs ten parameters in total to calibrate the model, although there are more parameters to calibrate, it is better suited for modelling the phenomenological coupling of mechanics and electrophysiology within nerve

tissue of larger scale or even at the head level because there is no need to obtain any microstructural information at the lower scale.

This model has the potential to become a flexible framework for modelling mechanical-electrophysiological coupling in nerve tissue. To fully understand the tissue level mechanical-electrophysiological coupling, further work is required to investigate the mechanisms in electrophysiological recovery and their relationships with the free energy in the mechanical system.

7 Conclusion

Contents

7.1 Summary 97
7.2 Conclusion 99
7.3 Future work 100

7.1 Summary

Chapter 1 highlighted the socioeconomic burden and the associated challenges posed by TBI and SCI. The specific primary mechanisms of axonopathy reviewed in Chapter 2 concluded that these injuries involve coupled mechanical-electrophysiological phenomena at multiple length scales, difficult to study with experimental means alone. It is therefore highly desirable to complement experimental studies with computational work to further the understanding of the coupled problem at different length scales.

In Chapter 3, a mechanical-electrophysiological coupled 3D FE framework for modelling axons was proposed. In this model, the electrophysiological HH and CT models, for the nodes of Ranvier and internodes, respectively, were introduced as surface boundary conditions directly in the weak form. The application of the model in an idealised case of axonal dislocation shows that, for a mild indentation, the

sole consideration of induced longitudinal stretch following transverse loading of a node of Ranvier is not enough to capture the severity of axonal electrophysiological deficit. This application demonstrated the potential usage of the 3D framework in modelling axonal electrophysiology alteration post mechanical loads.

Chapter 4 utilised the framework proposed in the previous chapter to study the mechanical-electrophysiological coupling in patch clamping. By considering the 3D flow of electrophysiology of a piece of membrane under suction, an alternative geometry based explanation to the "left-shifted" dynamics in electrophysiology observed by Wang et al. [24] was proposed.

Chapters 5 and 6 were dedicated to comparing axonal, fibre and tissue level models and their abilities to capture macroscale electrophysiology under various strains and strain rates. Chapter 5 extended an existing axonal model, *Neurite*, to a fibre model by considering a representative distribution of geometrical diameters, nodal and internodal lengths. The chapter also aimed at identifying the most "representative" axon calibre from a range of physical diameters in a single axon model. Both models were calibrated with a robust optimisation method to search for parameters with the best fit with the experimental data from Shi et al. [52]. The fibre model was shown to perform better than the single axon model for capturing macroscale electrophysiology, however both of these approaches were shown to fall short of capturing the strain rates dependencies and the recovery in CAP. The bottom-up approach for capturing macroscopic electrophysiological changes did not seem to be effective as the altered macroscale electrophysiology is not necessarily a linear combination of the axonal electrophysiology.

Chapter 6 presented a more generic approach to the modelling of mechanical-electrophysiological coupling by considering the energetic terms of a tissue level mechanical model. This model proposed that the damage is related to the free energy of the mechanical system during uniaxial loading and stress free relaxation. This model captured well the stress-strain tendencies during mechanical loading and relaxation. The tissue level model was generally more effective at capturing the CAP

tendencies compared to the fibre and axonal models, however it also fell short of capturing completely the relaxation of CAP (similar to the fibre and axonal models).

7.2 Conclusion

This thesis presented models that are appropriate for studying mechanical- electrophysiological coupling at different length scales. At the axon level, a 3D model was presented and a main conclusion from this model was that when studying mechanical-electrophysiological damage mechanisms, considering only the mechanical deformation in 1D is insufficient for modelling the resultant conduction deficits. Advanced experimental techniques such as digital image correlation have been applied to 3D neuronal cultures, where deformation fields were characterised [111], or the study of functional connectivity of neurons within a 3D sample with microelectrode arrays are experimentally feasible [59]. Based aforementioned finding, future experimental and computational studies should consider and characterise comprehensively the mechanical boundary conditions that are applied to the axonal sample. Furthermore, it is experimentally difficult to only apply pure loading modes, therefore as well as adopting advanced experimental techniques, future research should take advantage of computational techniques to explore different damage mechanisms.

At the subcellular level, this thesis presented a model that can study the mechanical-electrophysiological coupling of membranes within a pipette. It was demonstrated that the membrane geometry alone can give rise to an alteration of electrophysiology. If the current density is calibrated with HEK cell's ion channels expression levels, using the system presented by Trapani et al. [138] this model has the potential to link varying degree of pressure and membrane tension to the amount of mechano-sensitivity experienced by voltage gated ion channels.

Beyond cellular and subcellular scales, this thesis explored the modelling of a population of axons. It demonstrated that by introducing a redundancy of axons of different calibre (and hence difference susceptibility to mechanical-electrophysiological damage), the redundancy and variation in population acts

as natural protection to the electrophysiological signals. This is opposed to a single theoretical axon which would suffer a much more severe conduction block than the axonal bundle.

In order to scale the mechanical-electrophysiological modelling to a higher organ level, such as a whole head, it would not be practical to obtain microstructure information for the entire head. Instead, a phenomenological model with fewer parameters has been shown in this thesis to be effective for modelling a spinal cord segment.

From the fibre and phenomenological models, another conclusion that can be drawn is that it is important to consider other slower mechanical-electrophysiological mechanisms when studying tissue scale electrophysiological recovery. Furthermore, it is important to use a model that is relevant to the length scale of interest, since the electrophysiological recovery cannot be straightforwardly linked by only considering the dysfunction of Na_V and K_V and the mechanical recovery of the tissue. These are both important findings for guiding future modelling efforts aiming to quantify the level of electrophysiological dysfunction for a time frame that is relevant for medical intervention. The electrophysiological recovery is not only dependent on the mechanical recovery of axonal structures (such as membrane and ion channels), but also dependent on other mechanisms that are yet to be established (such as mechanically induced Ca^{2+} dynamics alterations).

7.3 Future work

Each of the models presented in this thesis has the potential to be a useful research tool. At the subcellular level, the membrane pipette model has the potential to link varying degrees of pressure and membrane tension to the amount of mechanosensitivity experienced by voltage gated ion channels by calibrating it with the current density measured. This could be a powerful tool for testing different mechanisms for mechanosensitive electrophysiological alterations. For the study of a population of axons, the axonal fibre model can be calibrated with morphometric studies of local axon population and can be used for modelling conduction blockages in upper extremity nerve damage or the conduction recovery of carpel tunnel

syndrome post pressure relief treatment. Finally, the phenomenological model has the potential to be scaled to a larger length scale which could be clinically relevant for determining regions that might experience electrophysiological change post traumatic head injury.

In order to build a more practical picture that is relevant for medical intervention for injury scenarios, such as in sports, it is important to investigate how mechanical impacts alter the dynamics of Ca^{2+} as well as Na^{+} and K^{+}. The 3D FE framework developed in this thesis can be adapted to study mechanical- electrophysiological coupling by observing the Ca^{2+} dynamics with fluorescence imaging, combined with the observation of cell deformation with high speed cameras. This framework has the potential to investigate and identify electrophysiological changes triggered by complex loading such as shear stress.

The evaluation of electrophysiological conduction in this thesis has been based on the reduction in CAP/AP amplitude, since this acts as a good primary indicator as to whether or not the axons are functional. It is important to note that even though the CAP/AP amplitude may present itself to be an obvious candidate for evaluating electrophysiological deficits, there are also many other aspects of neuronal signalling that are equally, if not more important, to investigate, such as latency of conduction and conduction velocity. The rate of information transfer within axons has been observed to encode complex information [139]. Furthermore, axons in the periphery of damage have been observed to alter their excitability [58]. These are important observations that are relevant to the understanding of mechanically altered electrophysiology on a larger scale.

Experimentally, strains of spinal cord can be measured through digital image correlation [147], while the altered electrophysiology can be characterised by quantifying the rate and latency of AP. These experimental efforts can be complemented with computational simulations using the axon, fibre and tissue models presented in this thesis. The above will allow for the investigation of the best computational representation of mechanically altered conduction rate, which would

be invaluable for building noninvasive methods for evaluating electrophysiological deficits post mechanical injury.

Both furthering the understanding of Ca^{2+} dynamics and conduction speed post-mechanical injury with the aid of computational tools can help design treatment protocols. If carefully calibrated and validated, the above set of simulation tools, in combination with a head level model, have the potential to evaluate and inform the levels of damage *in situ* (through evaluating the excitability, propagation latency and signal amplitude) after a mechanical injury. By allowing clinicians to evaluate the injury and prescribe treatment effectively without the need for invasive investigation, these tools have the potential to transform the treatment paradigm for TBIs and SCIs.

Appendices

A
Appendix

Contents

A.1 $\frac{\partial f_{CT}}{\partial V}$ **106**
A.2 $\frac{\partial f_{HH}}{\partial V}$ **106**
A.3 $\frac{\partial f_{CT}}{\partial u_{kb}}$ **108**
A.4 $\frac{\partial f_{HH}}{\partial u_{kb}}$ **108**
A.5 $\frac{\partial n_i}{\partial u_{kb}}$ **109**
A.6 ε_s **110**
A.7 1D FE script **111**

The following are terms derrived for the mechanical-electrophysiological coupling FE framework presented in Chapter 3.

A.1 $\frac{\partial f_{CT}}{\partial V}$

Recalling Equations (3.15) and (3.16):

$$f_{CT}(V, \frac{\partial V}{\partial t}, \varepsilon_s) = -\rho_c \left(\frac{C_m C_{my}}{h_m C_{my} + n_{my} h_{my} C_m} \frac{\partial V}{\partial t} + \frac{1}{h_m \rho_m + n_{my} h_{my} \rho_{my}} (V - V_{rest}) \right) \tag{A.1}$$

In incremental form with respect to V at time t^{i+1}, this equation reads:

$$f_{CT}(V^\alpha, \frac{V^{i+1} - V^i}{\Delta t}, \varepsilon_s) = -\rho_c \left(\frac{C_m C_{my}}{h_m C_{my} + n_{my} h_{my} C_m} \frac{V^{i+1} - V^i}{\Delta t} + \frac{1}{h_m \rho_m + n_{my} h_{my} \rho_{my}} (V^\alpha - V_{rest}) \right) \tag{A.2}$$

where V^{i+1}, V^i are, respectively, the values of V at t^{i+1} and t^i, where $\Delta t = t^{i+1} - t^i$ is the time step, α is a parameter specifying the intermediary time between t^{i+1} and t^i, and where:

$$V^\alpha = (1 - \alpha) V^i + \alpha V^{i+1} \tag{A.3}$$

Ultimately, the derivation of Equation (A.2) with respect to V^{i+1} yields:

$$\left. \frac{\partial f_{CT}}{\partial V} \right|_{V = V^{i+1}} = -\frac{\rho_c}{\Delta t} \left(\frac{C_m C_{my}}{h_m C_{my} + n_{my} h_{my} C_m} + \frac{\alpha \Delta t}{h_m \rho_m + n_{my} h_{my} \rho_{my}} \right) \tag{A.4}$$

A.2 $\frac{\partial f_{HH}}{\partial V}$

Recalling Equations (3.15) and (3.16):

$$f_{HH}(V, \frac{\partial V}{\partial t}, \varepsilon_s) = \frac{-\rho_c}{h_m} \left(C_m \frac{\partial V}{\partial t} + G_{Na}(V - E_{Na}(\varepsilon_s)) + G_K(V - E_K(\varepsilon_s)) + G_L(V - E_L) \right) \tag{A.5}$$

In incremental form with respect to V at time step t^{i+1}, this equation reads:

$$f_{HH}(V^\alpha, \frac{V^{i+1}-V^i}{\Delta t}, \varepsilon_s) = \frac{-\rho_c}{h_m}\left(C_m\frac{V^{i+1}-V^i}{\Delta t} + G_{Na}(V^\alpha,\varepsilon_s)(V^\alpha - E_{Na}(\varepsilon_s)) + G_K(V^\alpha,\varepsilon_s)(V^\alpha - E_K(\varepsilon_s)) + G_L(V^\alpha,\varepsilon_s)(V^\alpha - E_L(V^\alpha,\varepsilon_s))\right) \tag{A.6}$$

Ultimately, one has

$$\begin{aligned}\left.\frac{\partial f_{HH}}{\partial V}\right|_{V=V^{i+1}} = \frac{-\rho_c}{h_m}\Bigg(&\frac{C_m}{\Delta t} + \alpha(G_{Na}(V^\alpha,\varepsilon_s) + G_K(V^\alpha,\varepsilon_s) + G_L) \\ &+ \left.\frac{\partial G_{Na}(V^\alpha,\varepsilon_s)}{\partial V}\right|_{V=V^{i+1}}(V^\alpha - E_{Na}(\varepsilon_s)) \\ &+ \left.\frac{\partial G_K(V^\alpha,\varepsilon_s)}{\partial V}\right|_{V=V^{i+1}}(V^\alpha - E_K(\varepsilon_s)) \\ &- G_L\left.\frac{\partial E_L(V^\alpha,\varepsilon_s)}{\partial V}\right|_{V=V^{i+1}}\Bigg)\end{aligned} \tag{A.7}$$

where, using Table 3.1,

$$\begin{cases}\left.\frac{\partial G_{Na}(V^\alpha,\varepsilon_s)}{\partial V}\right|_{V=V^{i+1}} = \alpha\bar{G}_{Na}\left(3m_\alpha^2 h_\alpha \left.\frac{\partial m}{\partial V}\right|_{V=V^\alpha} + m_\alpha^3 \left.\frac{\partial h}{\partial V}\right|_{V=V^\alpha}\right) \\ \left.\frac{\partial G_K(V^\alpha,\varepsilon_s)}{\partial V}\right|_{V=V^{i+1}} = 4\alpha n_\alpha^3\bar{G}_K \left.\frac{\partial n}{\partial V}\right|_{V=V^\alpha}\end{cases} \tag{A.8}$$

where forward Euler approximation is used as follows:

$$\begin{cases} m_\alpha \approx m_i + \alpha\Delta t \left.\frac{dm}{dt}\right|_{V=V^i} \\ h_\alpha \approx h_i + \alpha\Delta t \left.\frac{dh}{dt}\right|_{V=V^i} \\ n_\alpha \approx n_i + \alpha\Delta t \left.\frac{dn}{dt}\right|_{V=V^i}\end{cases} \tag{A.9}$$

where the temporal derivatives of m, h and n at time step t_i are directly obtained from Table 3.1. The remaining terms of Equation (A.8), i.e., $\left.\frac{\partial m}{\partial V}\right|_{V=V^\alpha}$, $\left.\frac{\partial h}{\partial V}\right|_{V=V^\alpha}$ and $\left.\frac{\partial n}{\partial V}\right|_{V=V^\alpha}$, can be evaluated numerically. Alternatively, under loading slow enough so that the variation of m, n and h are mainly driven by variation in V and not in ε_s, the following approximation can be made:

$$\begin{cases}\left.\frac{\partial m}{\partial V}\right|_{V=V^\alpha} \approx \frac{\Delta t}{V^{i+1}-V^i}\left.\frac{dm}{dt}\right|_{V=V^i} \\ \left.\frac{\partial h}{\partial V}\right|_{V=V^\alpha} \approx \frac{\Delta t}{V^{i+1}-V^i}\left.\frac{dh}{dt}\right|_{V=V^i} \\ \left.\frac{\partial n}{\partial V}\right|_{V=V^\alpha} \approx \frac{\Delta t}{V^{i+1}-V^i}\left.\frac{dn}{dt}\right|_{V=V^i}\end{cases} \tag{A.10}$$

This last assumption is naturally *a priori* violated under very high strain rate loading cases such as blast loadings.

A.3 $\frac{\partial f_{CT}}{\partial u_{kb}}$

Under the assumption that the CT permittivity, resistivities and membrane/myelin layer thicknesses are independent of the deformation because of the geometrical dependency, the derivation of Equation (A.1) yields:

$$\frac{\partial f_{CT}}{\partial u_{kb}} = 0 \tag{A.11}$$

Note that this would not be the case if involving damage-driven capacity and/or resistivity alteration.

A.4 $\frac{\partial f_{HH}}{\partial u_{kb}}$

While HH membrane and leak permittivity, resistivities and conductivities are independent of the deformation, the ion channels conductivities and potentials are deformation dependent. The derivation of f_{HH} with respect to u_{kb} thus yields:

$$\begin{aligned}\frac{\partial f_{HH}}{\partial u_{kb}} = \frac{-\rho_c}{h_m}\frac{\partial \varepsilon_s}{\partial u_{kb}}\Bigg(&\frac{\partial G_{Na}(V,\varepsilon_s)}{\partial \varepsilon_s}(V - E_{Na}(\varepsilon_s)) \\ &+ \frac{\partial G_K(V,\varepsilon_s)}{\partial \varepsilon_s}(V - E_K(\varepsilon_s)) \\ &- G_{Na}(V,\varepsilon_s)\frac{\partial E_{Na}(\varepsilon_s)}{\partial \varepsilon_s} \\ &- G_K(V,\varepsilon_s)\frac{\partial E_K(\varepsilon_s)}{\partial \varepsilon_s}\Bigg)\end{aligned} \tag{A.12}$$

where, using Table 3.1,[1]

$$\begin{cases} \frac{\partial G_{Na}(V,\varepsilon_s)}{\partial \varepsilon_s} = \bar{G}_{Na}\left(3m^2 h\frac{\partial m}{\partial \varepsilon_s} + m^3\frac{\partial h}{\partial \varepsilon_s}\right) \\ \frac{\partial G_K(V,\varepsilon_s)}{\partial \varepsilon_s} = 4n^3\bar{G}_K\frac{\partial n}{\partial \varepsilon_s} \end{cases} \tag{A.13}$$

and

$$\begin{cases} \frac{\partial E_{Na}(\varepsilon_s)}{\partial \varepsilon_s} = \begin{cases} -\frac{\gamma}{\tilde{\varepsilon}}\left(\frac{\varepsilon_s}{\tilde{\varepsilon}}\right)^{\gamma-1} E^0_{Na}, & \text{if } \varepsilon_s < \tilde{\varepsilon} \\ 0, & \text{else.} \end{cases} \\ \frac{\partial E_K(\varepsilon_s)}{\partial \varepsilon_s} = \begin{cases} -\frac{\gamma}{\tilde{\varepsilon}}\left(\frac{\varepsilon_s}{\tilde{\varepsilon}}\right)^{\gamma-1} E^0_{K}, & \text{if } \varepsilon_s < \tilde{\varepsilon} \\ 0, & \text{else.} \end{cases} \end{cases} \tag{A.14}$$

In Equation (A.13), $\frac{\partial m}{\partial \varepsilon_s}$, $\frac{\partial h}{\partial \varepsilon_s}$ and $\frac{\partial n}{\partial \varepsilon_s}$ can be evaluated numerically. ε_s is defined in Appendix A.6

[1] Note that under the same assumption as in Equation (A.10), both following terms can be considered equal to 0.

A.5 $\frac{\partial n_i}{\partial u_{kb}}$

For any element face belonging to the domain boundary $\partial\Omega_0$, such as the grey area in Figure A.1, the tangent basis vectors $\mathbf{a_1}$ and $\mathbf{a_2}$ are defined by:

$$\mathbf{a}_\alpha(\boldsymbol{\xi}) = \sum_{a=1}^{n_s} \mathbf{x}_a^s N_{a,\alpha}^s(\boldsymbol{\xi}), \forall \alpha \in \{1,2\} \tag{A.15}$$

where $N_{a,\alpha}^s(\boldsymbol{\xi})$ are the corresponding shape functions derivatives with respect to the natural direction α, $\boldsymbol{\xi}$ being the coordinate vector in the surface element isoparametric reference frame. The normalised normal vector is then given by:

$$\mathbf{n} = \frac{\mathbf{a}_1 \times \mathbf{a}_2}{||\mathbf{a}_1 \times \mathbf{a}_2||} \tag{A.16}$$

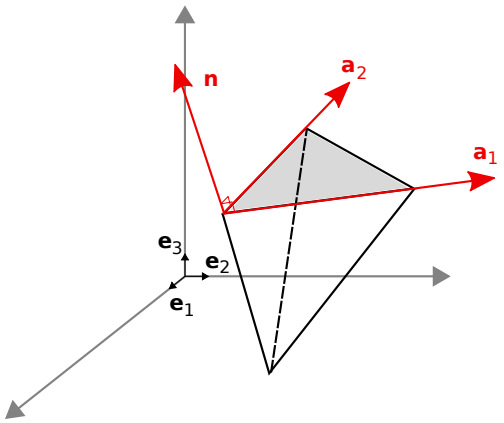

Figure A.1: Surface element: tangent basis vector $\mathbf{a}_1$ and $\mathbf{a}_2$, and normal vector $\mathbf{n}$ in the global reference frame defined by the basis vectors $(\mathbf{e}_1, \mathbf{e}_2, \mathbf{e}_3)$.

As a consequence, one has:

$$\frac{\partial n_i}{\partial u_{kb}} = \frac{\partial n_i}{\partial x_{kb}} = \underbrace{\frac{1}{||\mathbf{a}_1 \times \mathbf{a}_2||} \frac{\partial \left[(\mathbf{a}_1 \times \mathbf{a}_2) \cdot \mathbf{e}_i\right]}{\partial x_{kb}}}_{A} + \underbrace{\left[(\mathbf{a}_1 \times \mathbf{a}_2) \cdot \mathbf{e}_i\right] \frac{\partial}{\partial x_{kb}} \left(\frac{1}{||\mathbf{a}_1 \times \mathbf{a}_2||}\right)}_{B} \tag{A.17}$$

- Using the Levi-Vicita—or permutation—symbol, ϵ_{ijk}, one obtains:

$$A = \frac{1}{||\mathbf{a}_1 \times \mathbf{a}_2||} \frac{\partial(\epsilon_{ijl} a_{1j} a_{2l})}{\partial x_{kb}} = \frac{\epsilon_{ijl}}{||\mathbf{a}_1 \times \mathbf{a}_2||} \left(a_{1j} \frac{\partial a_{2l}}{\partial x_{kb}} + a_{2l} \frac{\partial a_{1j}}{\partial x_{kb}}\right) \tag{A.18}$$

Based on Equation (A.15),

$$\begin{cases} \frac{\partial a_{1j}}{\partial x_{kb}} = \delta_{jk} N_{b,1}^s \\ \frac{\partial a_{2l}}{\partial x_{kb}} = \delta_{lk} N_{b,2}^s \end{cases} \tag{A.19}$$

Noting that $\epsilon_{ijl} = -\epsilon_{jil}$, Equation (A.18) can thus be rewritten as:

$$A = \frac{\epsilon_{ikl}}{||\mathbf{a}_1 \times \mathbf{a}_2||} \left(a_{2l} N^s_{b,1} - a_{1l} N^s_{b,2} \right) \tag{A.20}$$

which can also be rewritten as

$$A = \frac{\epsilon_{klq}}{||\mathbf{a}_1 \times \mathbf{a}_2||} \left(a_{2l} N^s_{b,1} - a_{1l} N^s_{b,2} \right) \delta_{iq} \tag{A.21}$$

- One has:

$$B = -\left[(\mathbf{a}_1 \times \mathbf{a}_2) \cdot \mathbf{e}_i \right] \frac{\partial ||\mathbf{a}_1 \times \mathbf{a}_2||}{\partial x_{kb}} \frac{1}{||\mathbf{a}_1 \times \mathbf{a}_2||^2} \tag{A.22}$$

and by noting that the derivative of a vector norm can be written as $||\mathbf{u}||' = \frac{\mathbf{u} \cdot \mathbf{u}'}{||\mathbf{u}||}$, B can be rewritten as

$$B = -\frac{n_i}{||\mathbf{a}_1 \times \mathbf{a}_2||} \mathbf{n} \cdot \frac{\partial \left(\mathbf{a_1} \times \mathbf{a_2} \right)}{\partial x_{kb}} = -\frac{n_i \epsilon_{klq}}{||\mathbf{a}_1 \times \mathbf{a}_2||} \left(a_{2l} N^s_{b,1} - a_{1l} N^s_{b,2} \right) n_q \tag{A.23}$$

making use of the derivation of A.

Finally, gathering Equations (A.21) and (A.23):

$$\frac{\partial n_i}{\partial u_{kb}} = \frac{\epsilon_{klq}}{||\mathbf{a}_1 \times \mathbf{a}_2||} \left(a_{2l} N^s_{b,1} - a_{1l} N^s_{b,2} \right) (\delta_{iq} - n_i n_q) \tag{A.24}$$

A.6 ε_s

The surface strain ε_s can be defined as:

$$\varepsilon_s = \frac{\mathbf{a}_1 \times \mathbf{a}_2}{||\mathbf{A}_1 \times \mathbf{A}_2||} - 1 \tag{A.25}$$

where $\mathbf{A}_1$ and $\mathbf{A}_2$ are the counterparts of $\mathbf{a}_1$ and $\mathbf{a}_2$, respectively, in the reference configuration.

A.7 1D FE script

The following is the Matlab script for 1D HH and CT finite element electrophysiololgy, which was used for verifying the Gmsh implementation as presented in Chapter 3.

```
close all;
clear all;

nb_output = 100; % number of outputs
reltol    = 1e-6; % relative tolerance for NR

%%%%%%%%%%%%%%%%%%%%
% Axon parameters %
%%%%%%%%%%%%%%%%%%%%
L = 5e-3;  % length of axon
dia = 3e-6; % axon diameter

%%%%%%%%%%%%%%%%%%%%%%%%%%
% Spatial discretisation %
%%%%%%%%%%%%%%%%%%%%%%%%%%
ne = 100; % number of elements
h  = L/ne;  % element size
nn = ne+1; % number of nodes
coordinates  = 0:h:L;
connectivity = [(1:nn-1)',(2:nn)'];

% 1D linear element
xi_q      = 1/2;
Na_q      = [1-xi_q,xi_q];
dNadxi_q = [-1,1];

w_q       = ones(ne,1);
J_q       = zeros(ne,1);
dNadX_q   = zeros(ne,2);
for i=1:ne
J_q(i)        = dNadxi_q*coordinates(connectivity(i,:))';
dNadX_q(i,:) = dNadxi_q/J_q(i);
end

%%%%%%%%%%%%%%%%%%%%%%%%%%%%%%%%%%%
% Electrophysiological parameters %
%%%%%%%%%%%%%%%%%%%%%%%%%%%%%%%%%%%
rhoc     = 1.89; % (Ohm m) axial cytoplasm resisitivity
C        = 1/rhoc;
hm       = 4e-9; % (nm) membrane thickness
hmy      = 18e-9;% (nm) mylin layer thickness
nmy      = 0;    % number of myelin layers
Cm       = 4e-11;% (F/m)membrane electric constant
Cmy      = 1.08e-10;% (F/m)myelin layer electric constant
rhom     = 2.5e9; % membrane resistivity
rhomy    = 4.44e6; % myelin layer resistivity
Vrest    = -65e-3; % resting potential

%%%%%%%%%%%%%%%%%%%%%%%%
% Time discretisation %
%%%%%%%%%%%%%%%%%%%%%%%%
time         = 0; % initialise time
total_time   = 0.01; % total time of simulation
dt           = 4e-4; % time step size
nt           = ceil(total_time/dt); % number of time step
ite_max      = 100; % max number of iteration for NR

%%%%%%%%%%%%%%%%%%%%%%%%
% Boundary conditions %
%%%%%%%%%%%%%%%%%%%%%%%%
% trigger = [time Direclet/Neumann Value]
trigger = [[0 1 0.5e-9];[total_time 1 0]];

%%%%%%%%%%
% Solver %
%%%%%%%%%%
V          = Vrest*ones(nn,1);
Ve0        = Vrest*ones(ne,1);
Ve1        = Vrest*ones(ne,1);
GradVe     = zeros(ne,1);
fCT        = zeros(ne,1);
dfCTdV     = zeros(ne,1);

if trigger(1,2) == 1    % if trigger is a voltage trigger
V(1,1) = trigger(1,3);
end

for i=2:nt % loop for time step

time   = time + dt;
```

```
disp(['time = ', num2str(time), ' s']);
tol    = reltol * (h/dt)^(1/ne);
for j=1:ne
Ve0(j) = Na_q*V(connectivity(j,:),i-1);
end
V(:,i) = V(:,i-1);

ite = 1;
while ite < ite_max

disp([' iteration ', num2str(ite)]);
stiffness = zeros(nn,nn);
residual  = zeros(nn,1);
for j=1:ne

Ve1(j)    = Na_q*V(connectivity(j,:),i);
GradVe(j) = dNadX_q(j,:)*V(connectivity(j,:),i);
fCT(j)    = -rhoc*((Cm*Cmy/(hm*Cmy+nmy*hmy*Cm))*(Ve1(j)-Ve0(j))/dt...
+ (1/(hm*rhom+nmy*hmy*rhomy))*(Ve1(j)-Vrest));
dfCTdV(j) = -(rhoc/dt)*(Cm*Cmy/(hm*Cmy+nmy*hmy*Cm));

%%%%%%%%%%%%%%%%%%%
% Residual vector %
%%%%%%%%%%%%%%%%%%%
residual(connectivity(j,:)) = residual(connectivity(j,:))...
+ w_q(j)*J_q(j)* (dNadX_q(j,:)'*GradVe(j)* (dia^2))...
- (w_q(j)*J_q(j)* Na_q *fCT(j)*(4*dia))' ;

%%%%%%%%%%%%%%%%%%%
% Stiffness matrix %
%%%%%%%%%%%%%%%%%%%
stiffness(connectivity(j,:),connectivity(j,:)) = ...
stiffness(connectivity(j,:),connectivity(j,:))...
+ w_q(j)*J_q(j)*( 1*dNadX_q(j,:)'*dNadX_q(j,:) * dia^2)...
- (w_q(j)*J_q(j)* Na_q'*dfCTdV(j)*Na_q *(4*dia) );
end

%%%%%%%%%%%%%%%%%%%%%%
% Boundary conditions %
%%%%%%%%%%%%%%%%%%%%%%
bcFactor = max(stiffness(:));
% fixing voltage at -65mV at x=L, while applying a voltage or current at x=0
stiffness(end, end-1:end) = [-bcFactor bcFactor]; % dVdx = 0 in stiffness matrix
residual(end) = 0;

for k=1:(size(trigger,1)-1)
if (time > trigger(k,1) && time < trigger(k+1,1))
if trigger(k,2) == 1 % a voltage trigger
stiffness_eff = stiffness(2:(nn-1),2:(nn-1));
residual_eff  = residual(2:(nn-1),1);
residual_eff(:) = residual_eff(:) ...
- stiffness(2:(nn-1),1) * (trigger(k,3)-V(1,i-1));
V(1,i) = trigger(k,3);
V(2:nn-1,i) = V(2:nn-1,i) - stiffness_eff\residual_eff;
break;
elseif trigger(k,2) == 2 % a current trigger
stiffness_eff = stiffness(1:(nn-1),1:(nn-1));
residual_eff  = residual(1:(nn-1),1);
residual_eff(1) = residual_eff(1) - trigger(k,3);
V(1:nn-1,i) = V(1:nn-1,i) - stiffness_eff\residual_eff;
break;
end
end
end

error_res = norm(residual_eff);
disp(['  error = ', num2str(error_res)]);
if error_res < tol
break
end
ite = ite +1;
end
if ite == ite_max
error('iterations reached maximum');
end

end

figure
hold on
plot(V(:,1:ceil(nt/nb_output):nt))
hold off
```

```
% This code is used to study HH electrophysiology with 1D FEM
close all;
clear all;

nb_output = 100;
reltol    = 1e-6;

%%%%%%%%%%%%%%%%%%%
% Axon  parameters %
%%%%%%%%%%%%%%%%%%%
```

```
L = 5e-3;  % length of axon
dia = 3e-6; % axon diameter

%%%%%%%%%%%%%%%%%%%%%%%%%%%
% Spatial discretisation %
%%%%%%%%%%%%%%%%%%%%%%%%%%%
ne = 100;  % number of elements
he  = L/ne;  % element size
nn = ne+1; % number of nodes
coordinates  = 0:he:L;
connectivity = [(1:nn-1)',(2:nn)'];

% 1D linear element
xi_q      = 1/2;
Na_q      = [1-xi_q,xi_q];
dNadxi_q = [-1,1];

w_q       = ones(ne,1);
J_q       = zeros(ne,1);
dNadX_q  = zeros(ne,2);
for i=1:ne
J_q(i)        = dNadxi_q*coordinates(connectivity(i,:))';
dNadX_q(i,:) = dNadxi_q/J_q(i);
end

%%%%%%%%%%%%%%%%%%%
```

```
104   for i=2:nt % loop for time step
105
106   time   = time + dt;
107   disp(['time = ', num2str(time), ' s']);
108   tol    = reltol * (he/dt)^(1/ne);
109   for j=1:ne
110   Ve0(j) = Na_q*V(connectivity(j,:),i-1);
111   end
112   V(:,i) = V(:,i-1);
113
114   ite = 1;
115
116   while ite < ite_max
117
118   disp([' iteration ', num2str(ite)]);
119   stiffness = zeros(nn,nn);
120   residual  = zeros(nn,1);
121   for j=1:ne
122
123   Ve1(j)       = Na_q*V(connectivity(j,:),i);
124   GradVe(j)    = dNadX_q(j,:)*V(connectivity(j,:),i);
125
126   %dt and V in msec and mV for hh rate constants calculation
127   mV = 1e3; msec = 1e3;
128   Vprev = Ve0(j);
129   Vcurr = Ve1(j);
130   alpha_m = (2.5-0.1*( (Vcurr-Vrest)*mV )) / (exp(2.5 - 0.1*( (Vcurr-Vrest)*mV ))-1);
131   beta_m = 4*exp(-( (Vcurr-Vrest)*mV )/18);
132   alpha_h = 0.07*exp(-( (Vcurr-Vrest)*mV )/20);
133   beta_h = 1/( exp( 3 - 0.1*( (Vcurr-Vrest)*mV ) ) + 1 );
134   alpha_n = (0.1 - 0.01*( (Vcurr-Vrest)*mV ))/(exp(1 - 0.1*( (Vcurr-Vrest)*mV ))-1);
135   beta_n = 0.125*exp(-( (Vcurr-Vrest)*mV )/80);
136
137   m(j) = m_prev(j) + dt*msec*(alpha_m*(1 - m_prev(j)) - beta_m*m_prev(j));
138   h(j) = h_prev(j) + dt*msec*(alpha_h*(1 - h_prev(j)) - beta_h*h_prev(j));
139   n(j) = n_prev(j) + dt*msec*(alpha_n*(1 - n_prev(j)) - beta_n*n_prev(j));
140
141   GNa = G_Na*m(j)^3*h(j);
142   GK  = G_K*n(j)^4;
143   GL = G_L;
144
145   fHH(j) = -(rhoc/(hm))*((Cm*(Vcurr-Vprev)/dt) + GNa*(Vcurr - ENa)...
146   + GK*(Vcurr - EK)...
147   + GL*(Vcurr - EL));
148   dfHHdV(j) = -(rhoc/hm)*(Cm/dt);
149
150   %%%%%%%%%%%%%%%%%%%
151   % Residual vector %
152   %%%%%%%%%%%%%%%%%%%
153   residual(connectivity(j,:)) = residual(connectivity(j,:))...
154   + w_q(j)*J_q(j)* (dNadX_q(j,:)'* GradVe(j)* (0.25*pi*dia^2))...
155   - (w_q(j)*J_q(j)* Na_q *fHH(j)*(pi*dia))' ;
156
157   %%%%%%%%%%%%%%%%%%%
158   % Stiffness matrix %
159   %%%%%%%%%%%%%%%%%%%
160   stiffness(connectivity(j,:),connectivity(j,:)) = ...
161   stiffness(connectivity(j,:),connectivity(j,:))...
162   + w_q(j)*J_q(j)*( dNadX_q(j,:)'*dNadX_q(j,:) * (0.25*pi*dia^2) )...
163   - (w_q(j)*J_q(j)* Na_q'*dfHHdV(j)*Na_q *(pi*dia) );
164
165   end
166
167   %%%%%%%%%%%%%%%%%%%%%%
168   % Boundary conditions %
169   %%%%%%%%%%%%%%%%%%%%%%
170   bcFactor = max(stiffness(:));
171   % fixing voltage at -65mV at x=L, while applying a voltage or current at x=0
172   stiffness(end, end-1:end) = [-bcFactor bcFactor]; % dVdx = 0 in stiffness matrix
173   residual(end) = 0;
174
175   for k=1:(size(trigger,1)-1)
176   if (time > trigger(k,1) && time < trigger(k+1,1))
177   if trigger(k,2) == 1 % a voltage trigger
178   stiffness_eff = stiffness(2:(nn),2:(nn));
179   residual_eff  = residual(2:nn,1);
180   residual_eff(:) = residual_eff(:) ...
181   - stiffness(2:nn,1) * (trigger(k,3)-V(1,i-1));
182   V(1,i) = trigger(k,3);
183   V(2:nn,i) = V(2:nn,i) - stiffness_eff\residual_eff;
184   break;
185   elseif trigger(k,2) == 2 % a current trigger
186   stiffness_eff = stiffness(1:(nn-1),1:(nn-1));
187   residual_eff  = residual(1:(nn-1),1);
188   residual_eff(1) = residual_eff(1) - trigger(k,3);
189   V(1:nn-1,i) = V(1:nn-1,i) - stiffness_eff\residual_eff;
190   break;
191   end
192   end
193   end
194
195   error_res = norm(residual_eff);
196   disp(['  error = ', num2str(error_res)]);
```

```
197     if error_res < tol
198     break
199     end
200     ite = ite +1;
201     end
202
203     m_prev = m;
204     h_prev = h;
205     n_prev = n;
206
207     if ite == ite_max
208     error('iterations reached maximum');
209     end
210
211     end
212
213     figure
214     hold on
215     plot(coordinates(:),V(:,1:ceil(nt/nb_output):nt))
216     hold off
```

References

[1] A Jerusalem et al. “A computational model coupling mechanics and electrophysiology in spinal cord injury”. In: *Biomech Model Mechanobiol* 13 (2013), pp. 883–896.

[2] P A Boucher, B Joós, and C E Morris. “Coupled left-shift of Nav channels: Modeling the Na+-loading and dysfunctional excitability of damaged axons”. In: *J Comput Neurosci* 33.2 (2012), pp. 301–319.

[3] V Volman and L J Ng. “Primary paranode demyelination modulates slowly developing axonal depolarization in a model of axonal injury”. In: *J Comput Neurosci* 37.3 (2014), pp. 439–457.

[4] V E Johnson, W Stewart, and H S Douglas. “Axonal pathology in traumatic brain injury”. In: *Exp Neurol* 246 (2013), pp. 35–43.

[5] H Ouyang et al. “Compression induces acute demyelination and potassium channel exposure in spinal cord”. In: *J Neurotrauma* 27.6 (2010), pp. 1109–1120.

[6] C J Sparrey and T M Keaveny. “Compression behavior of porcine spinal cord white matter”. In: *J Biomech* 44.6 (2011), pp. 1078–1082.

[7] N A Shaw. “The neurophysiology of concussion”. In: *Prog Neurobiol* 67.4 (2002), pp. 281–344.

[8] A J Fournier et al. “Changes in neurofilament and microtubule distribution following focal axon compression”. In: *PLOS ONE* 10.6 (2015), e0131617.

[9] D J Sharp, G Scott, and R Leech. “Network dysfunction after traumatic brain injury”. In: *Nat Rev Neurol* 10.3 (2014), pp. 156–166.

[10] J Mez et al. “Clinicopathological evaluation of chronic traumatic encephalopathy in players of american football”. In: *JAMA* 318.4 (2017), pp. 360–370.

[11] F M Maynard Jr et al. “International standards for neurological and functional classification of spinal cord injury”. In: *Spinal Cord* 35 (1997), pp. 266–274.

[12] M Faul et al. “Traumatic brain injury in the United States: national estimates of prevalence and incidence, 2002–2006”. In: *Injury Prevention* 16 (2010), A268–A268.

[13] V G Coronado et al. “The CDC traumatic brain injury surveillance system: characteristics of persons aged 65 years and older hospitalized with a TBI”. In: *J Head Trauma Rehabil* 20.3 (2005), pp. 215–228.

[14] E Zaloshnja et al. “Prevalence of Long-Term Disability From Traumatic Brain Injury in the Civilian Population of the United States, 2005”. In: *J Head Trauma Rehabil* 23.6 (2008), pp. 394–400.

[15] P Corso et al. “Incidence and lifetime costs of injuries in the United States”. In: *Injury Prevention* 12.4 (2006), pp. 212–218.

[16] T Lawrence et al. “Traumatic brain injury in England and Wales: prospective audit of epidemiology, complications and standardised mortality”. In: *BMJ Open* 6.11 (2016), e012197.

[17] S Connell et al. “Novel model to investigate blast injury in the central nervous system”. In: *J Neurotrauma* 28.7 (2011), pp. 1229–36.

[18] Y C Chen, D H Smith, and D F Meaney. “In-vitro approaches for studying blast-induced traumatic brain injury”. In: *J Neurotrauma* 26.6 (2009), pp. 861–876.

[19] R A Stern et al. “Clinical presentation of chronic traumatic encephalopathy”. In: *Neurology* 81.13 (2013), pp. 1122–1129.

[20] L E Goldstein et al. “Chronic traumatic encephalopathy in blast-exposed military veterans and a blast neurotrauma mouse model”. In: *Sci Transl Med* 4.134 (2012), 134ra60.

[21] P P Tsitsopoulos and N Marklund. “Amyloid-beta peptides and tau protein as biomarkers in cerebrospinal and interstitial fluid following traumatic brain injury: A review of experimental and clinical studies”. In: *Front Neurol* 4 (2013), pp. 1–17.

[22] L J Ng et al. “A mechanistic end-to-end concussion model that translates head kinematics to neurologic injury”. In: *Front Neurol* 8 (2017), p. 629.

[23] D Sahoo, C Deck, and R Willinger. “Brain injury tolerance limit based on computation of axonal strain”. In: *Accid Anal Prev* 92 (2016), pp. 53–70.

[24] J A Wang et al. “Membrane trauma and Na^+ leak from Nav1.6 channels.” In: *Am J Physiol Cell Physiol* 297.4 (2009), pp. C823–C834.

[25] C H Berthold and M Rydmark. “Morphology of normal peripheral axons”. In: *The axon: structure, function and pathophysiology*. Ed. by S G Waxman, J D Kocsis, and Stys P.K. New York: Oxford University Press, 1995.

[26] A Hirano and J F Llena. “Morphology of central nervous system axons”. In: *The axon: structure, function and pathophysiology*. Ed. by S G Waxman, J D Kocsis, and Stys P.K. New York: Oxford University Press, 1995.

[27] N A Silva et al. “From basics to clinical: A comprehensive review on spinal cord injury”. In: *Prog Neurobiol* 114 (2014), pp. 25–57.

[28] J A Kiernan and N Rajakumar. *Barr’s The human nervous system*. Canada: Lippincott Williams & Wilkins, 2014.

[29] H Lodish, A Berk, and Zipursky S.L. “Overview of Neuron Structure and Function”. In: *Molecular Cell Biology*. Ed. by H Lodish, A Berk, and Zipursky S.L. New York: W.H. Freeman, 2000.

[30] M Sato et al. “Rheological properties of living cytoplasm: A preliminary investigation of squid axoplasm (Loligo pealei)”. In: *Cell Motil* 4.1 (1984), pp. 7–23.

[31] J M Ritchie. “Physiology of axons”. In: *The axon: structure, function and pathophysiology*. Ed. by S G Waxman, J D Kocsis, and Stys P.K. New York: Oxford University Press, 1995.

[32] A Hess and J Z Young. “The nodes of Ranvier”. In: *Proc. R. Soc. Lond. B* 140 (1952), pp. 301–320.

[33] C Koch. *Biophysics of computation. Information processing in single neurons.* New York: Oxford University Press, 1999.

[34] S G Waxman. "Voltage-gated ion channels in axons: Localisation, function and development". In: *The axon: structure, function and pathophysiology.* Ed. by S G Waxman, J D Kocsis, and Stys P.K. New York: Oxford University Press, 1995.

[35] R Luján. "Organisation of potassium channels on the neuronal surface". In: *J Chem Neuroanat* 40.1 (2010), pp. 1–20.

[36] R Nashmi and M G Fehlings. "Changes in axonal physiology and morphology after chronic compressive injury of the rat thoracic spinal cord". In: *Neuroscience* 104 (2001), pp. 235–251.

[37] A Krishnan et al. "Axonal ion channels from bench to bedside: A translational neuroscience perspective". In: *Prog Neurobiol* 89 (2009), pp. 288–313.

[38] P K Stys, S G Waxman, and B R Ransom. "Ion pumps and exchangers". In: *The axon: structure, function and pathophysiology.* Ed. by S G Waxman, J D Kocsis, and Stys P.K. New York: Oxford University Press, 1995.

[39] P Stys and J D Kocsis. "Electrophysiological approaches to the study of axons". In: *The axon: structure, function and pathophysiology.* Ed. by S G Waxman, J D Kocsis, and Stys P.K. New York: Oxford University Press, 1995.

[40] L Zhang, K H Yang, and A I King. "Comparison of brain responses between frontal and lateral impacts by finite element modeling". In: *J Neurotrauma* 18.1 (2001), pp. 21–30.

[41] M A Hemphill et al. "Traumatic brain injury and the neuronal microenvironment: A potential role for neuropathological mechanotransduction". In: *Neuron* 85.6 (2015), pp. 1177–1192.

[42] D F Meaney and D H Smith. "Biomechanics of concussion". In: *Clin Sports Med* 30.1 (2011), pp. 19–vii.

[43] S A Kruse et al. "Magnetic resonance elastography of the brain". In: *Neuroimage* 39.1 (2008), pp. 231–237.

[44] S Budday et al. "Mechanical properties of gray and white matter brain tissue by indentation". In: *J Mech Behav Biomed Mater* 46 (2015), pp. 318–330.

[45] K L Monson et al. "Axial mechanical properties of fresh human cerebral blood vessels". In: *J Biomech Eng* 125.2 (2003), pp. 288–294.

[46] T M Reeves et al. "Proteolysis of submembrane cytoskeletal proteins ankyrin-G and alpha-II-spectrin following diffuse brain injury: A role in white matter vulnerability at Nodes of Ranvier". In: *Brain Pathol* 20.6 (2010), pp. 1055–1068.

[47] T M Reeves, L L Phillips, and J T Povlishock. "Myelinated and unmyelinated axons of the corpus callosum differ in vulnerability and functional recovery following traumatic brain injury". In: *Exp Neurol* 196.1 (2005), pp. 126–137.

[48] D G Siedler et al. "Diffuse axonal injury in brain trauma: insights from alterations in neurofilaments". In: *Front Cell Neurosci* 8 (2014), p. 429.

[49] J T Wang, Z A Medress, and B A Barres. "Axon degeneration: Molecular mechanisms of a self-destruction pathway". In: *J Cell Biol* 196.1 (2012), pp. 7–18.

[50] J E Greer et al. “Mild traumatic brain injury in the mouse induces axotomy primarily within the axon initial segment”. In: *Acta Neuropathol* 126.1 (2013), pp. 804–828.

[51] R Shi and J D Pryor. “Temperature dependence of membrane sealing following transection in mammalian spinal cord axons”. In: *Neuroscience* 98.1 (2000), pp. 157–166.

[52] R Shi and J Whitebone. “Conduction deficits and membrane disruption of spinal cord axons as a function of magnitude and rate of strain”. In: *J Neurophysiol* 95.March 2006 (2006), pp. 3384–3390.

[53] J A Wolf et al. “Traumatic axonal injury induces calcium influx modulated by tetrodotoxin-sensitive sodium channels”. In: *J Neurosci* 21.6 (2001), pp. 1923–1930.

[54] M N Rasband and P Shrager. “Ion channel sequestration in central nervous system axons”. In: *J Physiol* 525 (2000), pp. 63–73.

[55] Y Eshed-Eisenbach and E Peles. “Axonal spectrins: All-purpose fences”. In: *J Cell Biol* 203 (2013), pp. 381–383.

[56] D R Coleman and Filbin M T. “Cell adhesion molecules in myelination”. In: *Basic Neurochemistry: Molecular, Cellular and Medical Aspects*. Ed. by Siegel G J, Agranoff B W, and Albers R W. Philadelphia: Lippincott-Raven, 1999.

[57] W Sun et al. “Paranodal myelin damage after acute stretch in guinea pig spinal cord”. In: *J Neurotrauma* 10 (2012), pp. 611–619.

[58] J E Greer, J T Povlishock, and K M Jacobs. “Electrophysiological Abnormalities in Both Axotomized and Nonaxotomized Pyramidal Neurons following Mild Traumatic Brain Injury”. In: *J Neurosci* 32.19 (2012), pp. 6682–6687.

[59] W H Kang et al. “Alterations in hippocampal network activity after in vitro traumatic brain injury”. In: *J Neurotrauma* 32.13 (2015), pp. 1011–1019.

[60] S K Agrawal and M G Fehlings. “Mechanisms of secondary injury to spinal cord axons in vitro: role of $Na^+, Na^+ - K^+ - ATPase, the Na^+ - H^+ exchanger, and the Na^+ - Ca^{2+} exchanger$”. In: *J Neurosci* 16.2 (1996), pp. 545–552.

[61] A Hånell, J Greer, and K Jacobs. “Increased network excitability due to altered synaptic inputs to neocortical layer V intact and axotomized pyramidal neurons after mild traumatic brain injury”. In: *J Neurotrauma* 1598 (2015), pp. 804–828.

[62] A S Hunanyan et al. “Alterations of action potentials and the localization of Nav1.6 sodium channels in spared axons after hemisection injury of the spinal cord in adult rats”. In: *J Neurophysiol* 105 (2011), pp. 1033–1044.

[63] W H Kang and B III Morrison. “Predicting changes in cortical electrophysiological function after in vitro traumatic brain injury”. In: *Biomech Model Mechanobiol* 14.5 (2015), pp. 1033–1044.

[64] T P Patel et al. “Single-neuron NMDA receptor phenotype influences neuronal rewiring and reintegration following traumatic injury”. In: *J Neurosci* 34.12 (2014), pp. 4200–4213.

[65] T P Patel et al. “Automated quantification of neuronal networks and single-cell calcium dynamics using calcium imaging”. In: *J Neurosci Methods* 243.Supplement C (2015), pp. 26–38.

[66] K D Browne et al. “Mild traumatic brain injury and diffuse axonal injury in Swine”. In: *J Neurotrauma* 28.9 (2011), pp. 1747–1755.

[67] Q Luo et al. “Complexity analysis of resting state magnetoencephalography activity in traumatic brain injury patients”. In: *J Neurotrauma* 30.20 (2013), pp. 1702–1709.

[68] A Singh et al. “Structural and functional changes in nerve roots due to tension at various strains and strain rates: An in-vivo study”. In: *J Neurotrauma* 26 (2009), pp. 627–640.

[69] H Ouyang et al. “Biomechanics of spinal cord injury: a multimodal investigation using ex vivo guinea pig spinal cord white matter.” In: *J Neurotrauma* 25.1 (2008), pp. 19–29.

[70] G C Magou, B J Pfister, and J R Berlin. “Effect of acute stretch injury on action potential and network activity of rat neocortical neurons in culture”. In: *Brain Research* 1624 (2015), pp. 525–535.

[71] D H Smith et al. “High tolerance and delayed elastic response of cultured axons to dynamic stretch injury”. In: *J Neurosci* 19.11 (1999), pp. 4263–4269.

[72] M D Tang-Schomer et al. “Mechanical breaking of microtubules in axons during dynamic stretch injury underlies delayed elasticity, microtubule disassembly, and axon degeneration”. In: *FASEB J* 24.5 (2010), pp. 1401–1410.

[73] O Farkas, J Lifshitz, and J T Povlishock. “Mechanoporation induced by diffuse traumatic brain injury: An irreversible or reversible response to injury?” In: *J Neurosci* 26.12 (2006), pp. 3130–3140.

[74] C R Von Reyn et al. “Mechanisms of calpain mediated proteolysis of voltage gated sodium channel alpha-subunits following in vitro dynamic stretch injury”. In: *J Neurochem* 121 (2012), pp. 793–805.

[75] M J McGinn et al. “Biochemical, structural, and biomarker evidence for calpain-mediated cytoskeletal change after diffuse brain injury uncomplicated by contusion”. In: *J Neuropathol Exp Neurol* 68.3 (2009), pp. 241–249.

[76] D M Geddes, R S Cargill II, and M C LaPlaca. “Mechanical stretch to neurons results in a strain rate and magnitude-dependent increase in plasma membrane permeability”. In: *J Neurotrauma* 20.10 (2004), pp. 1039–1049.

[77] A Iwata et al. “Traumatic axonal injury induces proteolytic cleavage of the voltage-gated sodium channels modulated by tetrodotoxin and protease inhibitors”. In: *J Neurosci* 24 (), pp. 4605–4613.

[78] N E Ziv and Spira M E. “Spatiotemporal distribution of Ca^{2+} following axotomy and throughout the recovery process of cultured aplysia neurons”. In: *Eur J Neurosci* 5.6 (1993), pp. 657–668.

[79] F Perocchi et al. “MICU1 encodes a mitochondrial EF hand protein required for Ca2+ uptake”. In: *Nature* 467 (2010), pp. 3525–3531.

[80] M A Hemphill et al. “A possible role for integrin signaling in diffuse axonal injury”. In: *PLOS ONE* 6.7 (2011).

[81] M Hines and N Carnevale. “The NEURON simulation environment”. In: *Neural Comput* 9 (1997), pp. 1179–1209.

[82] J Bower and D Beeman. In: *The book of GENESIS: exploring realistic neural models with the GEneral NEural SImulation System*. New York: Springer, 1998.

[83] B A Teplitzky et al. “Computational modeling of an endovascular approach to deep brain stimulation”. In: *J Neural Eng* 11.2 (), p. 026011.

[84] E M Moraud et al. “Mechanisms underlying the neurmoulation of spinal circuits for correcting gait and balance deficits after SCI”. In: *Neuron* 89.4 (2016), pp. 814–828.

[85] S Elia, P Lamberti, and V Tucci. “A finite element model for the axon of nervous cells”. In: *COMSOL Eur Conf* (2009), pp. 1–7.

[86] P Bauer et al. “Finite element analysis of neuronal electric fields: the effect of heterogeneous resistivity”. In: *arXiv* (2012), p. 7. eprint: `1211.0249`.

[87] H Meffin et al. “Modeling extracellular electrical stimulation: I. Derivation and interpretation of neurite equations.” In: *J Neural Eng* 9.6 (2012), p. 065005.

[88] B Tahayori et al. “Modeling extracellular electrical stimulation: II. Computational validation and numerical results”. In: *J Neural Eng* 9.6 (2012), p. 065006.

[89] H Meffin et al. “Modelling extracellular electrical stimulation: III. Derivation and interpretation of neural tissue equations.” In: *J Neural Eng* 11.6 (2014), p. 065004.

[90] B Tahayori et al. “Modelling extracellular electrical stimulation: IV. Effect of the cellular composition of neural tissue on its spatio-temporal filtering properties.” In: *J Neural Eng* 11.6 (2014), p. 065005.

[91] C F Babbs and R Shi. “Subtle paranodal injury slows impulse conduction in mathematical model of myelinated axons”. In: *PLOS ONE* 8 (2013), e67767.

[92] M Lachance et al. “Stimulation-induced ectopicity and propagation windows in model damaged axons”. In: *J Comput Neurosci* 37.3 (2014), pp. 523–531.

[93] N Yu et al. “Spontaneous excitation patterns computed for axons with injury-like impairments of sodium channels and Na/K pumps”. In: *PLOS Comput Biol* 8.9 (2012), pp. 1–20.

[94] C E Morris, P F Juranka, and B Joós. “Perturbed voltage-gated channel activity in perturbed bilayers: Implications for ectopic arrhythmias arising from damaged membrane”. In: *Prog Biophys Mol Biol* 110.2 (2012), pp. 245–256.

[95] D Garcia-Gonzalez et al. “A continuum mechanics constitutive framework for transverse isotropic soft tissues”. In: *J Mech Phys Solids* 112 (2018), pp. 209–224.

[96] T El Sayed et al. “Biomechanics of traumatic brain injury”. In: *Comput Methods Appl Mech Eng* 197 (2008), pp. 4692–4701.

[97] R J H Cloots et al. “Multi-scale mechanics of traumatic brain injury: predicting axonal strains from head loads”. In: *Biomech Model Mechanobiol* 12 (2013), pp. 137–150.

[98] C Giordano and S Kleiven. “Connecting fractional anisotropy from medical images with mechanical anisotropy of a hyperviscoelastic fibre-reinforced constitutive model for brain tissue”. In: *J Royal Soc Interface* 11.91 (2014).

[99] R M Wright et al. “A Multiscale Computational Approach to Estimating Axonal Damage under Inertial Loading of the Head.” In: *J Neurotrauma* 30.2 (2013), pp. 102–118.

[100] R de Rooij and E Kuhl. “Constitutive modeling of brain tissue: Current perspectives”. In: *ASME Appl Mech Rev* 68.1 (2016), pp. 010801–16.

[101] B Khuyagbaatar, K Kim, and H K Yoon. “Effect of bone fragment impact velocity on biomechanical parameters related to spinal cord injury: A finite element study”. In: *J Biomech* 47.11 (2014), pp. 2820–2825.

[102] B Galle et al. “Correlations between tissue-level stresses and strains and cellular damage within the guinea pig spinal cord white matter”. In: *J Biomech* 40.13 (2007), pp. 3029–3033.

[103] C S Drapaca. “An electromechanical model of neuronal dynamics using Hamilton’s principle”. In: *Front Cell Neurosci* 9 (2015), p. 271.

[104] T Tekieh et al. “Are deformed neurons electrophysiologically altered? A simulation study”. In: *Curr Appl Phys* 16.10 (2016), pp. 1413–1417.

[105] I Cinelli, M Duffy, and McHughP. “Thermo-electrical equivalents for simulating the electro-mechanical behavior of biological tissue”. In: *Conf Proc IEEE Eng Med Biol Soc* (2015), pp. 3969–3972.

[106] I Cinelli et al. “Neurotrauma evaluation in a 3D electro-mechanical model of a nerve bundle”. In: *NER’17* (2017), pp. 513–516.

[107] I Cinelli et al. “Effects of nerve bundle geometry on neurotrauma evaluation”. In: *NER’17* (2017), pp. 517–520.

[108] I Cinelli et al. “Electro-thermal equivalent 3D finite element model of a single neuron”. In: *IEEE Trans Biomed Eng* PP.99 (2017), pp. 1–1.

[109] M T Kwong et al. “3D finite element formulation for mechanical-electrophysiological coupling in axonopathy”. In: *Comput Methods Appl Mech Eng (under review)* (2018).

[110] A Goriely et al. “Mechanics of the brain: perspectives, challenges, and opportunities”. In: *Biomech Model Mechanobiol* 14.5 (2015), pp. 931–965.

[111] E Bar-Kochba et al. “Strain and rate-dependent neuronal injury in a 3D in vitro compression model of traumatic brain injury”. In: *Sci Rep* 6 (2016), p. 30550.

[112] G C Magou et al. “Engineering a High Throughput Axon Injury System”. In: *J Neurotrauma* 28 (2011), pp. 2203–2218.

[113] B J Pfister et al. “Stretch-grown axons retain the ability to transmit active electrical signals”. In: *FEBS Letters* 580 (2006), pp. 3525–3531.

[114] R Lorente De No. “The electrical excitability of the motoneurones”. In: *J Cell Compar Physiol* 7 (1935), pp. 47–71.

[115] A L Hodgkin and W A H Rushton. “The electrical constants of a crustacean nerve fibre”. In: *Proc R Soc Lond B Biol Sci* 133 (1946), pp. 444–479.

[116] C Geuzaine and J F Remacle. “Gmsh: A 3D finite element mesh generator with built-in pre- and post-processing facilities”. In: *Int J Numer Meth Eng* 79.11 (2009), pp. 1309–1331.

[117] L Wu et al. “A micro-meso-model of intra-laminar fracture in fiber-reinforced composites based on a discontinuous Galerkin/cohesive zone method”. In: *Eng Fract Mech* 104 (2013), pp. 162–183.

[118] G Cheng et al. “Mitochondria in traumatic brain injury and mitochondrial-targeted multipotential therapeutic strategies”. In: *Br J Pharmacol* 167 (2012), pp. 699–719.

[119] M A Avery et al. “Wld^S prevents axon degeneration through increased mitochondrial flux and enhanced mitochondrial Ca^{2+} buffering”. In: *Curr Biol* 22 (2012), pp. 596–600.

[120] A L Hodgkin and A F Huxley. “A quantitative description of membrane current and its application to conduction and excitation in nerve”. In: *J Physiol* 117 (1952), pp. 500–544.

[121] J A García-Grajales et al. “Neurite, a finite difference large scale parallel program for the simulation of electrical signal propagation in neurites under mechanical loading”. In: *PLoS One* 10.2 (Feb. 2015), pp. 1–22.

[122] A El Hardy and B B Machta. “Mechanical surface waves accompany action potential propagation”. In: *Nat Commun* 6.6697 (2015).

[123] A Gonzale-Perez et al. “Solitary electromechanical pulses in lobster neurons”. In: *Biophys Chem* 216 (2016), pp. 51–59.

[124] M Plaksin et al. “Thermal transients excite neurons through universal intramembrane mechanoelectrical effects”. In: *Phys Rev X* 8.011043 (2018).

[125] T Chomiak and B Hu. “What is the optimal value of the g-ratio for myelinated fibers in the rat CNS? A theoretical approach”. In: *PLOS ONE* 4 (2009), p. 37754.

[126] T Jensen et al. “Molecular X-ray computed tomography of myelin in a rat brain”. In: *NeuroImage* 57 (2011), pp. 124–129.

[127] C Hilderbrand and R Hahn. “Relation between myelin sheath thickness and axon size in spinal cord white matter of some bertebra species”. In: *J Neuro Sci* 38 (1985), pp. 421–434.

[128] J Loverde and B Pfister. “Developmental axon stretch stimulates neuron growth while maintaining normal electrical activity, intracellular calcium flux, and somatic morphology”. In: *Front Cell Neurosci* 9 (2015), p. 308.

[129] B S Colley et al. “Neurotrophin B receptor kinase increases Kv subfamily member 1.3 (Kv1.3) ion channel half-life and surface expression”. In: *Neurosci* 144.2 (2007), pp. 531–546.

[130] N Bavi et al. “Biophysical implications of lipid bilayer rheometry for mechanosensitive channels”. In: *Proc Natl Acad Sci U S A* 111.38 (2014), pp. 13864–9.

[131] O Bavi et al. “Influence of global and local membrane curvature on mechanosensitive ion channels: A finite element approach”. In: *Membranes* 6.1 (2016), E14.

[132] R S Gold. “The axon guide for electrophysiology biophysics laboratory techniques”. In: 2007.

[133] Y Zhang and O P Hamill. “On the discrepancy between whole-cell and membrane patch mechanosensitivity in Xenopus oocytes”. In: *J Physiol* 523.1 (2000), pp. 101–115.

[134] T M Suchyna, V S Markin, and F Sachs. “Biophysics and structure of the patch and the gigaseal”. In: *Biophys J* 97.3 (2009), pp. 738–747.

[135] H M Raghu, S Nandi, and S M Reddy. “Follicle size and oocyte diameter in relation to developmental competence of buffalo oocytes in vitro”. In: *Reprod Fertil Dev* 14 (2002), pp. 55–61.

[136] E Evans and A Yeung. “Apparent viscosity and cortical tension of blood granulocytes determined by micropipet aspiration”. In: *Biophys J* 56 (1989), pp. 151–160.

[137] B He and D M Soderlund. “Functional expression of rat Nav1.6 voltage-gated sodium channels in HEK293 cells: Modulation by the auxillary beta1 subunit”. In: *PLoS One* 9.1 (2014), e85188.

[138] J G Trapani and Stephen J K. “Control of ion channel expression for patch clamp recordings using an inducible expression system in mammalian cell lines”. In: *BMC Neurosci* 15.4 (2003).

[139] J A Perge et al. “Why do axons differ in caliber?” In: *J Neurosci* 32 (2012), pp. 626–638.

[140] R G Lascelles and P K Thomas. “Changes due to age in internodal length in the sural nerve in man”. In: *J Neurol Neurosurg Psychiat* 29 (1966), pp. 40–44.

[141] A D Vizoso. “The relationship between internodal length and growth in human nerves”. In: *J Anat* 84 (1950), pp. 342–352.

[142] R L Fride and R Bischhausen. “The precise geometry of large internodes”. In: *J Neurol Sci* 48 (1980), pp. 367–381.

[143] R L Fride and W Beuche. “Combined scatter diagrams of sheath thickness and fibre calibre in human sural nerves: changes with age and neuropathy”. In: *J Neurol Neurosurg Psychiatry* 48 (1985), pp. 749–756.

[144] R L Fride, B Johanna, and U Hartmann. “Changes in myelin sheath thickness and internode geometry in the rabbit phrenic nerve during growth”. In: *J Anat* 143 (1985), pp. 103–113.

[145] R L Fride. “Relation between myelin sheath thickness, internode geometry, and sheath resistance”. In: *Exp Neurol* 92 (1986), pp. 234–247.

[146] W A H Rushton. “A theory of the effects of fibre size in medullated nerve”. In: *J Physiol* 115 (1951), pp. 101–122.

[147] J Li and R Shi. “Stretch-induced nerve conduction deficits in guinea pig ex vivo nerve”. In: *J Biomech* 40.3 (2007), pp. 569–578.

[148] R Storn and K Price. “Differential evolution – A simple and efficient heuristic for global optimization over continuous spaces”. In: *J Global Optim* 11.4 (1997), pp. 341–359.

[149] C H Hakansson. “Conduction velocity and amplitude of the action potential as related to circumference in the isolated fibre of frog muscle”. In: *Acta Physiologica* 37 (1956), pp. 14–34.

[150] J P Dollé et al. “Brain-on-a-chip microsystem for investigating traumatic brain injury: Axon diameter and mitochondrial membrane changes play a significant role in axonal response to strain injuries”. In: *Technology* 2 (2014), p. 106.

[151] R W Ogden, G Saccomandi, and I Sgura. “Fitting hyperelastic models to experimental data”. In: *Comput Mech* 34.6 (2004), pp. 484–502.

[152] C T Chang et al. “Finite element modeling of hyper-viscoelasticity of peripheral nerve ultrastructures”. In: *J Biomech* 48 (2015), pp. 1982–1987.

[153] L Fradet et al. “Strain rate dependent behavior of the porcine spinal cord under transverse dynamic compression”. In: *Proc Inst Mech Eng H* 230.9 (2016), pp. 858–866.

[154] J Engelbrecht et al. “On the complexity of signal propagation in nerve fibres”. In: *Proc Est Acad Sci Eng* 67.1 (2018), pp. 28–38.

[155] S Budday et al. “Mechanical characterization of human brain tissue”. In: *Acta Biomater* 48 (2017), pp. 319–340.

[156] R J Fiford and L E Bilston. “The mechanical properties of rat spinal cord in vitro”. In: *J Biomechanics* 28 (2005), pp. 1509–1515.

[157] D H Smith and D F Meaney. “Axonal damage in traumatic brain injury”. In: *Porg Clin Neurosci* 6 (2000), pp. 483–492.